Master's thesis

NTNU
Norwegian University of Science and Technology
Faculty of Engineering
Department of Marine Technology

Vilde Eirin Eidsæther Bruun

Ship collision analysis of monopile offshore wind turbines

Analyse av skipsstøt for offshore vindturbiner understøttet av monopæl

Master's thesis in Marine Technology
Supervisor: Prof. Jørgen Amdahl
Co-supervisor: Postdoc Zhaolong Yu and PhD-candidate Stian H. Sørum
June 2021

NTNU
Norwegian University of
Science and Technology

Vilde Eirin Eidsæther Bruun

Ship collision analysis of monopile offshore wind turbines

Analyse av skipsstøt for offshore vindturbiner understøttet av monopæl

Master's thesis in Marine Technology
Supervisor: Prof. Jørgen Amdahl
Co-supervisor: Postdoc Zhaolong Yu and PhD-candidate Stian H. Sørum
June 2021

Norwegian University of Science and Technology
Faculty of Engineering
Department of Marine Technology

NTNU
Kunnskap for en bedre verden

NTNU
Norges teknisk-naturvitenskapelige universitet
Institutt for marin teknikk

MASTER THESIS 2021

For

Stud. **Vilde Eirin Eidsæther Bruun**

Ship collision analysis of monopile offshore wind turbines

Analyse av skipsstøt for offshore vindturbiner understøttet av monopæl

Background:
Wind power is considered to be “green” energy and a large number of wind turbines have been erected on land. However, the wind energy potential is considerably larger in open seas, the environmental impact is smaller, and consequently it is expected that an increasing part of the new wind farms will be installed offshore. Shallow water areas - up to approximately 50 - 70m water depth - will be utilized first as this will allow for bottom supported installations. Development is notably taking place in Sheringham Shoals and Dogger Bank in UK and in the Germany waters of the North Sea and the Baltic Sea.

Wind farms will be serviced by vessels and thus the risk of impacts exists. In addition, many offshore wind farms will be located close to ship traffic lanes and thus the risk of collision with merchant vessel or even large tankers become of concern. For wind turbines supported by monopiles, tripods or jackets several failure modes are possible:
- The support structure may be pushed over such that the turbine drops into the sea away from the vessel.
- The support structure may collapse at the impact point, so the tower collapse towards the vessel.
- The support structure may survive the impact, but local buckling of the tower may take place in the tower, such that it collapses towards or away from the vessel.

Ship collision analysis have been carried out to a large extent assuming central impacts, where the ship has to come to almost complete stop. Furthermore, the hydrodynamic forces during collision have been on simplified analysis. The objective of this investigation is to examine in detail the response of different bottom supported offshore wind turbines to ship impacts taking interaction between the hit structure and the ship into account by means of a local shell model in the contact area. Further, the hydrodynamic forces will be taken more accurately into account using a module based on linear potential theory into account and glancing bow/side impacts with large vessels will also be considered.

Scope of work

The following topics should be addressed:

1. Brief description of bottom supported wind turbine installations, Emphasis should be placed on the structural dimensions of the tower, monopiles and jackets for wind

turbines up to 15- 20 MW. Describe relevant collision scenarios (wrt. to ship size, contact locations, speed, impact angle, central and non-central (glancing) impacts etc.) and potential consequences /failure modes for the installations. Relevant codes requirements for ship collision design shall be reviewed.

2. Describe design philosophies that will be applicable for the collision scenarios. Discuss the concepts external and internal mechanics and strength, ductile and shared-energy design. Review analytical methods for simplified analysis of local energy dissipation in during collision. Discuss how interaction may influence the energy distribution. Describe how the hydrodynamic forces may be taken into account. Reference is made to paper by Yu et. al: *Implementation of linear potential-flow theory in the 6DOF coupled simulation of ship collision and grounding accidents, J. Ship Research*, June 2016.

3. Revisit of calculations with the simplified model of a monopile wind turbine support structure (tower, transition piece and pile, but not rotor blades) developed for LS-DYNA analysis of a central ship impact. To the extent needed the model may be updated to better reflect real geometries and modelling of soil boundary conditions. Redo analysis of broad side impact both with realistic simulation of the retardation process. Determine the force-local indentation relationship at the impact point, and, if possible, the contact force distribution (intensity). Compare results from LS-DYNA analysis with the simplified indentation models used in USFOS. Discuss how the dynamic response of the tower influences the resistance to local indentation.

4. Perform a parametric of the impact situation in pt.3. The impact velocity and the thickness of the monopile may be varied.

5. Conduct analysis of impact with larger vessels and larger impact energies. Possible candidates are a Ro-Ro vessel and a tanker where existing bow or side models in LS-DYNA will be made available. Sliding impact may also be carried out using the coupled simulation tool developed by Zhaolong Yu, refer *Implementation of linear potential-flow theory in the 6DOF coupled simulation of ship collision and grounding accidents, J. Ship Research*, June 2016.

6. Establish a finite element model of the wind turbine in USFOS. A finite element model of a 10 MW wind turbine (rotor and nacelle) and a turbine control algorithm will be made available, but the tower and soil must be modelled. Model also contact with ship by means of nonlinear springs that represent the resistance to local indentation and elastic unloading when the local indentation decreases. Perform analysis of the collision event for a turbine in parked and in operating condition. Compare key response parameters e.g., acceleration of nacelle, bending moment and local indentation. In operating conditions, the risk of rotor blades hitting the tower wall shall be monitored.

7. Evaluate whether the tower moment caused by ship collision may lead to local buckling and if so, model the tower structure with shell elements in the contact area. Imperfections may need to be introduced.

8. Develop a simplified analytic model for ship collision. It is envisaged that this model may be described by a linear spring representing the soil, a cantilever representation of the tower and a bending deformation of the tower supported at the nacelle. Alternatively,

by two vibration eigenmodes of the tower. The force deformation curve of the ship may be represented by a spring which is connected to the tower and a nodal mass representing the ship.

9. Conclusions and recommendations for further work.

Literature studies of specific topics relevant to the thesis work may be included.

The work scope may prove to be larger than initially anticipated. Subject to approval from the supervisor, topics may be deleted from the list above or reduced in extent.

In the thesis the candidate shall present his personal contribution to the resolution of problems within the scope of the thesis work.

Theories and conclusions should be based on mathematical derivations and/or logic reasoning identifying the various steps in the deduction.

The candidate should utilize the existing possibilities for obtaining relevant literature.

The thesis should be organized in a rational manner to give a clear exposition of results, assessments, and conclusions. The text should be brief and to the point, with a clear language. Telegraphic language should be avoided.

The thesis shall contain the following elements: A text defining the scope, preface, list of contents, summary, main body of thesis, conclusions with recommendations for further work, list of symbols and acronyms, references and (optional) appendices. All figures, tables and equations shall be numerated.

The supervisor may require that the candidate, in an early stage of the work, presents a written plan for the completion of the work. The plan should include a budget for the use of computer and laboratory resources which will be charged to the department. Overruns shall be reported to the supervisor.

The original contribution of the candidate and material taken from other sources shall be clearly defined. Work from other sources shall be properly referenced using an acknowledged referencing system.

The report shall be submitted in two copies:

- Signed by the candidate.
- The text defining the scope included.
- In bound volume(s).
- Drawings and/or computer prints which cannot be bound should be organised in a separate folder.

Supervisor:
Prof. Jørgen Amdahl
Postdoc Zhaolong Yu
PhD-candidate Stian H. Sørum

Deadline: June 10th, 2021

Trondheim, January 15, 2021

Jørgen Amdahl

Jørgen Amdahl

Abstract

With the increasing energy demand, offshore wind turbines (OWTs) are an excellent option to capture the full potential of wind energy to supplement the demand. However, with the increasing size of the wind farms and the OWTs, they are more exposed to ship collisions. Therefore, it is of interest to investigate a ship impact with an OWT.

The main goal of this thesis was to examine in detail the response of monopile supported OWT subjected to a ship impact. A 10MW OWT with monopile foundation located at a water depth of 30m was exposed to a drifting broadside impact from a 7,500 tons displacement supply vessel. The vessel collides with the monopile foundation of the OWT, which has a diameter of 9m and a wall thickness of 80mm. The impact velocities are 2m/s and 3/ms, resulting in impact energies of 21MJ and 47MJ, respectively. A finite element model has been created to represent the OWT. Local analysis was conducted in the software program LS-DYNA, while the global response of the OWT in both parked and operating condition was investigated in the software program USFOS. Additionally, USFOS has investigated local effects of concern, which is the effect of buckling.

The results of the analysis showed high resistance against global collapse for the studied cases. The most critical responses were found in the midsection of the tower and the acceleration of the nacelle. The most significant bending stresses for the midsection was found to be 285MPa for the operating condition when subjected to the largest impact velocity. The most significant acceleration of the nacelle was found to be for the parked condition with the largest impact velocity. In contrast, the most significant moment force was found for the operating condition for the largest impact velocity. No local buckling was observed in the midsection. The controller algorithm provided beneficial effects in operating condition by reducing the responses of the OWT. All scenarios were desirable as the OWT would withstand the impact from the broadside ship impact.

Sammendrag

Med økene etterspørsel for energi og nye bærekraftsmål er offshore vindturbiner en gyllen mulighet til å utnytte det fulle potensialet til vindenergi, og å redusere etterspørselen på en bærekraftig måte. Derimot utgjør den økende størrelsen på både offshore vindparker og offshore vindturbin at de blir mer utsatt for skipskollisjoner. Det er derfor av interesse å undersøke effekten av skipsstøt mot offshore vindturbin.

Hovedmålet med oppgaven var å undersøke i detalj responsen til en offshore vindturbin når den er utsatt for en skipskollisjon. En 10MW vindturbin med monopæl som base, står på en vanndybde på 30m når den blir truffet sidelengs av et drivende 7500 tonns deplasement forsyningsskip. Skipet kolliderer med monopælen som har en diameter på 9m og veggtykkelse 80mm. Skipsstøtet har hastigheter på 2m/s og 3m/s som tilsvarer initiale kinetiske energier på henholdsvis 21MJ og 47MJ. Lokal analyse av vindturbinen har blitt utført i programvaren LS-DYNA, mens globale analyser har blitt utført i programvaren USFOS for både parkert og operasjonell tilstand. I tillegg har lokale effekter som knekking blitt undersøkt i USFOS.

Resultatene fra analysene viser at vindturbinen har høy motstandsdyktighet mot skipsstøt. De mest kritiske resultatene var spenningene som oppsto i midtre del av tårnet, samt akselerasjonen av nacellen på toppen av tårnet. Den største bøyespenningen var 285MPa i operasjonell tilstand for den høyeste kollisjonshastigheten. Den største akselerasjonen ble funnet for parkert tilstand, mens den største momentkraften ble funnet i operasjonell tilstand. Begge for den største kollisjonshastigheten. Ingen lokal knekking ble observert i midtre del av tårnet. Kontrollalgoritmen ga gunstige effekter i operasjonell tilstand da den reduserte responsen av vindturbinen. Alle kollapsmekanismene som oppsto var ønskelige da vindturbinen viste høy motstandsdyktighet mot det drivende skipssøtet.

Preface

This master's thesis marks the end of the Master of Science degree in Marine Technology at the Norwegian University of Science and Technology (NTNU). The thesis objectives have been formulated by the main supervisor, Jørgen Amdahl, and assigned by the Department of Marine Technology. Further, it is inspired by the ongoing development of offshore wind energy and the author's interest in sustainable energy. The master's thesis is written as part of the specialisation Marine Structures.

The main aim of this thesis was to model complete models of the OWT in both LS-DYNA and USFOS and investigate the global response as an effect of local indentation caused by drifting broadside ship impact.

The thesis has provided an understanding of the theory and modelling behind OWTs subjected to ship impact. By weekly meetings through the semester, guidance has been provided. Due to the current SARS-CoV-2 pandemic, the majority of the meetings were held online and limited communications with the supervisors through digital platforms. This has been challenging when issues have arisen, and one was unable to visit supervisors in their offices directly and at once. Notably, the modelling stage has been challenging and been highly time-consuming. Issues with the location of output files regarding shell generation caused headaches but were eventually solved using a remote desktop.

Trondheim, 10th of June, 2021

Vilde E. Bruun

Vilde Eirin Eidsæther Bruun

Acknowledgement

I would first and foremost like to thank my supervisor Professor Jørgen Amdahl for the valuable information, guidance, and expertise throughout the semester. Next, I would like to thank Doctoral Research Fellow Stian Høegh Sørum for helping me with the theory on offshore wind turbines. He always answered my questions quickly and clearly. Further, I would like to thank Postdoctoral Fellow Zhaolong Yu for helping me in the modelling process in LS-DYNA. Lastly, I would like to direct a big thank you to my friends and family for getting me through these five demanding years.

Contents

List of Figures

List of Tables

Nomenclature

Abbreviations

ALS	Accidental limit states
BC	Boundary condition
BEM	Blade Element Momentum
CFD	Computational Fluid Dynamics
CWIF	Caithness Windfarm Information Forum
DNV GL	Det Norske Veritas Germanischer Lloyd
DOF	Degrees of freedom
FEM	Finite element method
FLS	Ultimate limit states
LRFD	Load and resistance factor design format
MSL	Mean sea level
NORSOK	The Norwegian shelf's competitive position
OWT	Offshore wind turbine
RNA	Rotor-nacelle-assembly
RP	Recommended practice

RWT	Reference wind turbine
SLS	Serviceability limit states
ULS	Ultimate limit states

Greek symbols

$\bar{\lambda}$	Reduced slenderness factor
β	Deformation of the installation
δ_0 & δ	Initial imperfection and maximum imperfection, respectively
ϕ	Plasticity reduction factor
ρ	Density
ρ_{kd}	Knock-down factor
σ_E	Elastic buckling resistance accounting for shape imperfections
σ_Y	Yield stress
σ_{cl}	Elastic buckling resistance
σ_{cr}	Elastic critical buckling stress
θ	Angle

Latin symbols

$\dot{u}_c$	Velocity at collision point
$\dot{u}_s$	Velocity of topside
a_s	Ship added mass

B	Bifurcation point or width of contact area
c_t	Linear damping term
$D, D_z \ \& \ D_s$	Diameter of tubular member, diameter of tower base and diameter of tower top, respectfully
dw_i	Deformation of the installation
dw_s	Deformation of the ship
E	Young's modulus
E_s	Total strain energy dissipation
$E_{s,i}$	Dissipated strain energy from installation
$E_{s,s}$	Dissipated strain energy from ship
E_{ship}	Deformation energy
F_c	Internal collision force
F_c'	Collision force
F_t	Internal transmitted force
F_t'	Generalised force
F_w	Wind load
g	Gravitational acceleration, $9.81m/s^2$, or rod length
I	Moment of inertia
$I_c \ \& \ I_t$	Impulse
K	Strength coefficient

k, c_1 & c_2	Factors used for calculation of resistance to indentation
k_c	Stiffness seen from ship fro zero deflection of OWT mass
k_p	Generalised stiffness
k_s	Stiffness coefficient
k_{ij}	Generalised stiffness coefficient
L	Limit point or length of spring
L_1	Total height of monopile
L_2	Total height of tower
L_s	Remaining length of cone which is not part of the OWT
L_z	Total length of cone
M	Bending moment
m_a	Mass of ship including added mass
M_p	Full plastic bending moment
m_s	Ship mass
m_t	Generalised topside mass
M_{red}	Reduced plastic bending moment
N	Buckling load
n	Hardening exponent, integration points
N_{Rd}	Design axial compressive force

N_{Sd}	Design axial compressive resistance
r	Radius
R_d	Design resistance
R_i	Resistance of installation
R_s	Resistance of ship
S_d	Design load effect
t	Wall thickness
t_1	Duration of first collision phase
t_2	Duration of second collision phase
u_A	Displacement of topside from wind load
u_c	Displacement at collision point
u'_c	Adjusted displacement at collision point
u_s	Displacement at collision point of the ship
u_t	Displacement of topside
u'_t	Adjusted displacement of topside
V_0	Impact velocity
v_s	Impact velocity
w	Coefficient of inertia moment
w_d	Dent depth

This page is intentionally left blank.

Chapter 1

Introduction

With the ever-increasing demand for energy to satisfy the growing population of the world, more renewable solutions are needed to reduce the impact on the environment. One of the widely used solutions is wind energy due to its high technological maturity and high wind resource availability (Esteban et al., 2010).

Onshore wind turbines represent the majority of the wind energy today as offshore wind turbines (OWT) are more complex in design, construction, and operations due to the ocean environment. However, one can see an increase in the development of offshore wind turbines as there are multiple advantages with moving wind turbines offshore, whereas better wind quality and more accessible areas being the main ones (Dai et al., 2013). Since 2009 the offshore wind energy in Europe has increased by over 733% in cumulative installed capacity (GW), demonstrating the rapid escalation of the offshore wind industry.

With increasing numbers of OWTs, higher risks of collisions follow. Additionally, OWTs are moving further away from shore and possibly into harsher environments, meaning commercial ship traffic and service vessels may increase in size. Therefore, it is of interest to investigate the impact between these vessels and OWTs. With increasing water depth, there is a change in the foundations of the OWTs. Typically shallow water depths, up to approximately 50 - 70m, utilise bottom supported foundations while floating foundations commonly dominate deeper water depths. This is because bottom-fixed OWTs are not economically profitable at deeper depths. For water depths of around 30m, monopiles have been the domineering foundation.

However, XL and XXL monopiles are challenging their fellow bottom-fixed foundations in deeper water depths by having diameters up to 10m and being used at depths in more than 40m (WindPower International, 2013). An example of these XL monopiles, located at a water depth of 37m, is the Gemini wind farm located off the coast of the Netherlands (Ramboll, 2016). Still, projects in even deeper waters and larger structures are ongoing.

1.1 Master's thesis objectives

This master's thesis objectives have been proposed by the main supervisor, Professor Jørgen Amdahl, at the start of the spring semester of 2021. The objectives can be seen at the beginning of this document. Briefly described: this master's thesis aims to research the global response of a monopile OWT based on local indentation resulting from ship collision. Throughout the work period, the scope of work has been discussed along the way. Due to time constraints and by approval of the supervisor, sliding impact with implementation of hydrodynamic forces using a coupled method was not carried out. The modifications of the master's thesis scope are as follows:

1. The literature study is focused on the monopile foundation rather than the jacket due to time limitations.
2. Modelling of the transition piece was not done as the focus was the effect of ship collision on the monopile. Hence, the impact is located at the monopile.
3. The seabed was modelled using a rotational spring rather than implementing soil characteristics.
4. A simple analytical model was presented but not verified due to time constraints.
5. Sliding impact using coupled simulation tool for ship collision was not conducted due to time constraints.

1.2 Approach to solving the thesis objectives

To achieve the stated thesis objectives, the following approach is used:

1. An extensive literature study to obtain knowledge on previous ship impacts with OWTs with monopile foundation. This by investigation of risks and consequences, design philosophies, and previous findings related to this topic.

2. A local analysis in the software program LS-DYNA and global analysis in the software program USFOS was conducted by modelling the OWT to obtain the results presented in this thesis. The model is made from scratch, except for the rotor-nacelle-assembly (RNA), hub, and blades in USFOS, which was given. Learning two new software programs and creating a realistic model has been very time-consuming but important to obtain accurate results. Thus, the majority of the time has been dedicated to modelling.

1.3 Limitations of the thesis

To perform the finite element analysis, a high demand for computational and storage capacity has had limitations on this thesis as a personal computer is used. Therefore, it has been necessary to implement trade-offs to reduce the computational time, but without affecting the results. These trade-offs are mainly the finite element mesh size and the time steps used for the most extensive analysis, which are the ones with shell elements. Further, the current SARS-CoV-2 pandemic has, to some extent, contributed to limited resources which generally would be available.

1.4 Main contributions from the thesis

The main contributions to this master's thesis are:

- Finite element model of a 10MW offshore wind turbine with a monopile foundation in the software programs LS-DYNA and USFOS. The finite element model includes the tower and monopile, while models for the RNA, hub, and blades have been given.
- Modelling and local analysis in LS-DYNA of drifting broadside ship impact with a 7,500 tons displacement supply vessel. The offshore wind turbine has been modelled to its full extent but the RNA, hub, and blades are simplified by being represented by a point mass. A parametric study with increased impact velocity, wall thickness, and yield strength is conducted to evaluate the response of the OWT.
- Modelling and global analysis in USFOS of broadside ship impact with impact velocities 2m/s and 3m/s, resulting in collision energies of 21MJ and 47MJ. The ship impact is represented with a combination of nonlinear spring and linear spring that

implements the force-deformation curve obtained in LS-DYNA.

- Investigation of the responses for the OWT in parked and operating condition.
- Examination of the global response of the OWT exposed to drifting broadside ship impact.
- Investigation of local buckling effects to the midsection of the OWT tower from the ship impact.

1.5 Thesis outline

The remaining part of this master's thesis is organised as follows:

- Chapter 2 presents the development of the offshore wind industry and challenges related to collision events with offshore wind turbines. Further, it discusses and assesses the risk of collision between an offshore wind turbine and a vessel. Contributing factors and potential consequences are also discussed. A literature study of previous work is presented.
- Chapter 3 presents the governing design principles based on relevant standards or recommended practices and the theory behind a ship collision.
- Chapter 4 describes the given ship section used in the analysis and the reference wind turbine used for modelling the offshore wind turbine in the thesis. A brief description of the given RNA, hub, blades and the control algorithm is given.
- Chapter 5 describes the local analysis conducted in the software program LS-DYNA and how the offshore wind turbine is modelled in this software. The chapter includes a parametric study of key parameters that may affect the dynamic response.
- Chapter 6 describes the global analysis done in the software program USFOS and how the OWT and ship are modelled.
- Chapter 7 presents the results from broadside ship impact with offshore wind turbine obtained from the global analysis in USFOS.
- Chapter 8 describes the local buckling analysis of the OWT conducted in USFOS, and the results from this analysis are presented.

- Chapter 9 presents a simple analytical approach to estimate the OWT response when subjected to ship impact.
- Chapter 10 includes the discussion and conclusion of this master's thesis.
- Chapter 11 gives recommendations for further work related to this work's subject.

Chapter 2

Background

2.1 Characteristics of an offshore wind turbine

An offshore wind turbine (OWT) consists of two main parts: the support structure and the rotor-nacelle-assembly (RNA). The support structure includes the tower, substructure, and foundation. The definitions of a wind turbine and its components can be seen from Figure 2.1 which additionally shows some different types of bottom-fixed foundations.

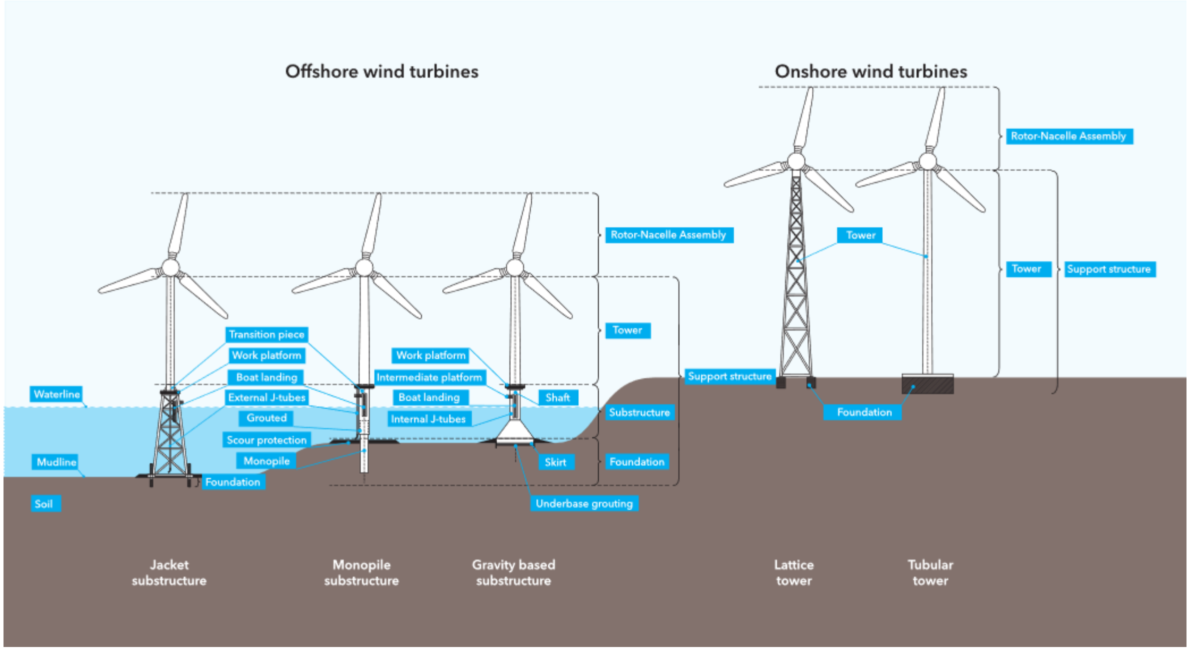

Figure 2.1: Definition of wind turbine components (DNV GL, 2018).

As mentioned previously, most OWTs are monopiles due to their simple shape, making them quick and cheap to fabricate and install. The monopile is part of the foundation and is hammered into the soil, anchoring the OWT to the seabed. When the foundation has been installed, the transition pieces are either bolted or grouted to the foundation and tower. This allows the tower and RNA to be fitted to the substructure and foundation, completing the OWT. The transition piece is essential as it transfers loads and moments between tower and foundation.

The size of the foundation depends on the water depth and the mounted turbine. With increased depth and turbine as well as a harsher environment, an increased diameter of the foundation follows. This is necessary to resist the static and dynamic forces from the sea, wind, and turbine (WindPower International, 2013). Up until recently, monopiles have been used in water depths of up to 30m. However, monopile designs are evolving. XL and XXL monopiles are on the rise and reaching deeper water depths.

2.2 Key trends and statistics

Due to the master's thesis specification mentioning the North Sea and Baltic Sea development, this thesis will explore the offshore wind industry in Europe. Therefore, information and background review is referenced to European development within this industry.

According to WindEurope (2020a), Europe installed 2.9GW of new capacity in 2020, giving Europe a total installed wind capacity of 25GW. The annual installed capacity has since 2010 increased by 733%, which can be seen from Figure 2.2. The figure further shows that Germany and UK contribute to the majority of the offshore wind capacity in Europe.

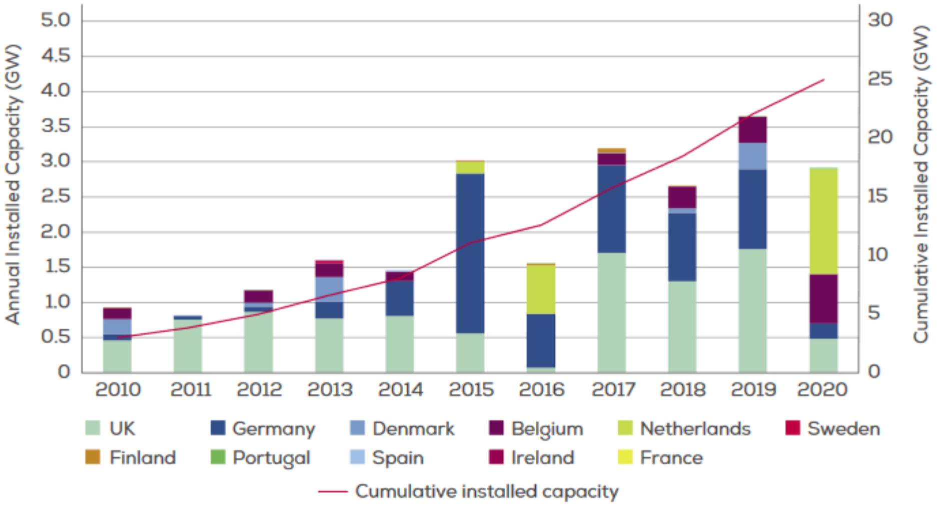

Figure 2.2: Annual offshore wind installations by country and cumulative capacity (GW) (WindEurope, 2021b).

Accordingly, 79% of the cumulative installed capacity in European sea basins are found in the North Sea as shown in Figure 2.3.

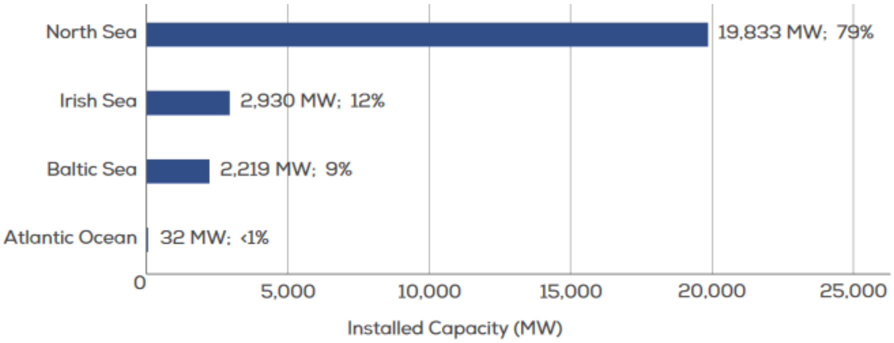

Figure 2.3: Cumulative installed capacity by sea basin (MW) (WindEurope, 2021b).

Therefore, it is coherent that average turbine capacity expands to provide the increase in installed capacity. This can be confirmed by Figure 2.4.

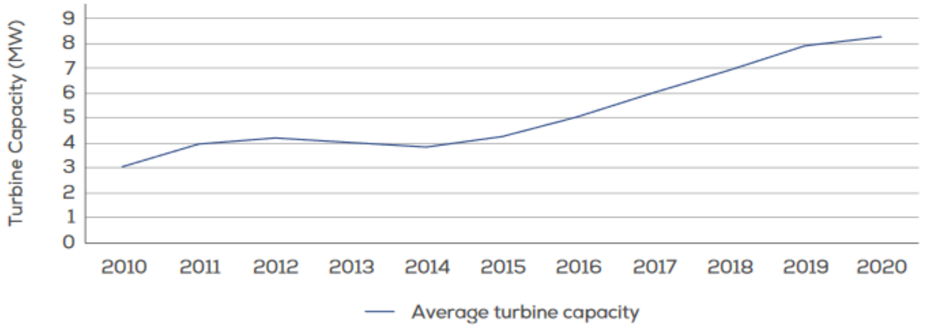

Figure 2.4: Yearly average of newly installed offshore wind turbines rated capacity (MW) (WindEurope, 2021b).

There are multiple substructures and foundations that can be used for an OWT, all depending on the installation environment. Some common types of foundations are shown in Figure 2.5.

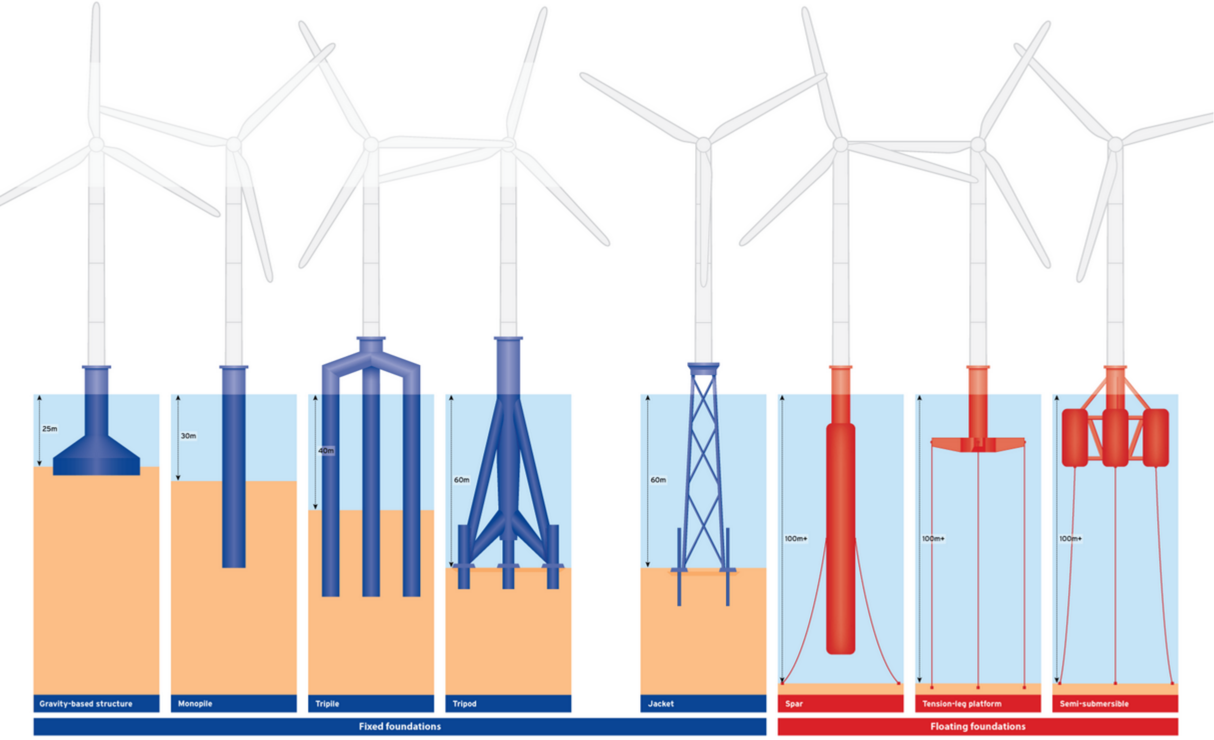

Figure 2.5: Foundations types and depth limits (WindPower Monthly, 2013).

Considering the common substructures that are used in the wind farms, one can see from Figure 2.6 that the monopile is the dominating one. This is due to the simplicity of calculations, fabrication, and transportation of the monopiles (WindPower International, 2013).

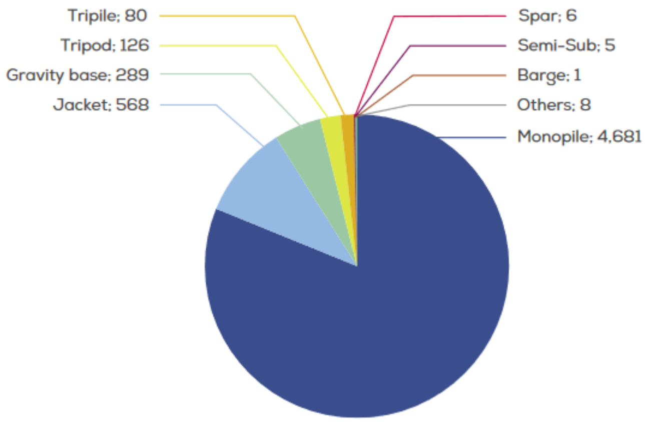

Figure 2.6: Cumulative number of foundations installed by substructure type - including all foundations installed with and without grid connection by the end of 2020 (WindEurope, 2021b).

Thus, it is of interest to investigate the monopile as the majority of OWTs are supported by these foundations. Likewise, due to the increasing application of monopiles at deeper water depths, they may continue to occupy more of the European seas.

2.3 Collision risks

Previous incidents of collisions with OWTs, based on the public database Caithness Windfarm Information Forum (CWIF) (Caithness Windfarm Information Forum, 2020), suggest that there are only seven relevant cases of service vessels colliding with an OWT (as of 1980 to July 4, 2020): One support and survey vessel, two barges, two crew transfer vessels and one unknown. Seven incidents since the 1980s is a low number and may indicate a low risk of collisions. However, it can be an indicator of negligence to report and document such incidents (Dai et al., 2013). Lack of transparency and access to information may also contribute to the low number of recorded collisions (Presencia & Shafiee, 2016). Consequently, it is not possible to base a risk analysis on these historical data. However, looking at the offshore oil and gas industry, more data is available and can be used as an indicator. It is interesting to mention that a semi-submersible has a higher risk of moderate to severe damage than a fixed bottom-standing platform. This may be due to the semi-submersible moving in waves and having higher impact velocities, leading to more significant damages. This information can indicate the extent of damage with a bottom-fixed versus a floating OWT during ship collisions (Dai et al., 2013).

The above discussion indicates a lack of information with regards to the frequency of collisions with OWTs. Therefore, it is interesting to study Figure 2.7 and Figure 2.8 shown below. Figure 2.7 presents the locations of the current wind farms where blue represents online OWTs, yellow represents partially online OWTs, and red represents under construction OWTs. Figure 2.8 shows the marine traffic density around the same area. The figures clearly show a large volume of marine traffic around the wind farms. Thus, it is evident that collision with an OWT exists and that this should be taken under consideration when constructing new OWTs.

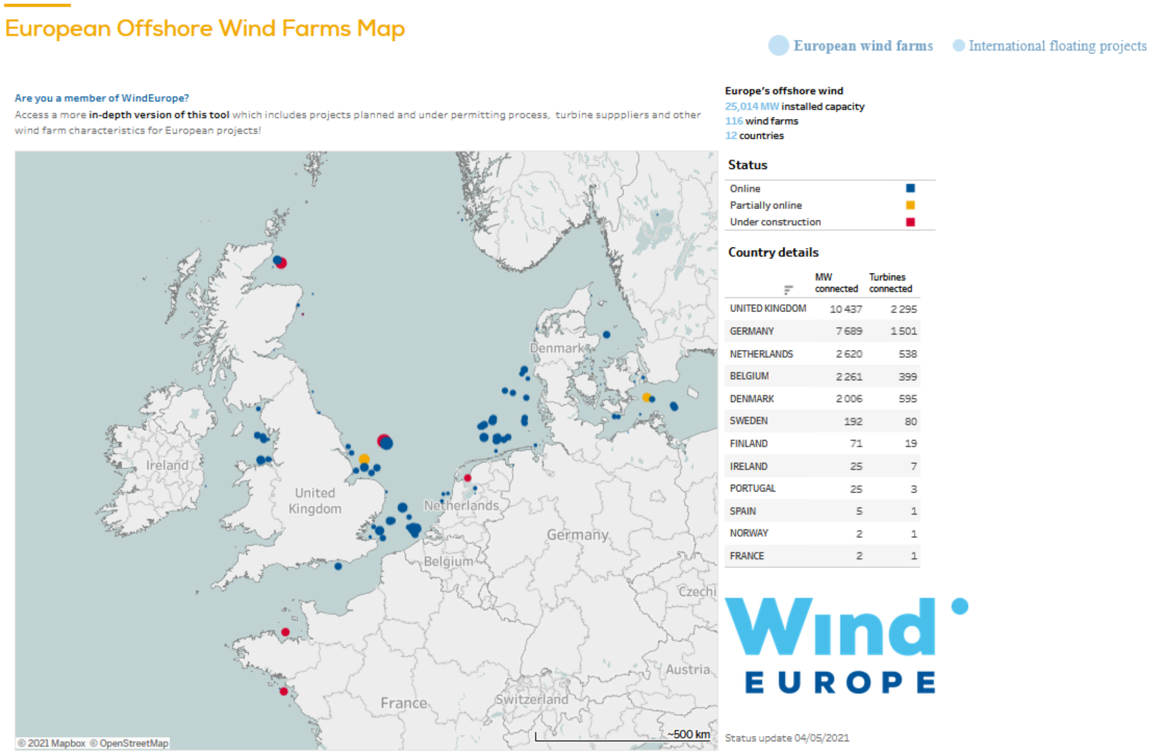

European Offshore Wind Farms Map

● European wind farms ● International floating projects

Are you a member of WindEurope?
Access a more **in-depth version of this tool** which includes projects planned and under permitting process, turbine suppppliers and other wind farm characteristics for European projects!

Europe's offshore wind
25,014 MW installed capacity
116 wind farms
12 countries

Status

Online	🟦
Partially online	🟨
Under construction	🟥

Country details

	MW connected	Turbines connected
UNITED KINGDOM	10 437	2 295
GERMANY	7 689	1 501
NETHERLANDS	2 620	538
BELGIUM	2 261	399
DENMARK	2 006	595
SWEDEN	192	80
FINLAND	71	19
IRELAND	25	7
PORTUGAL	25	3
SPAIN	5	1
NORWAY	2	1
FRANCE	2	1

Status update 04/05/2021

Figure 2.7: European offshore wind farms (WindEurope, 2021a).

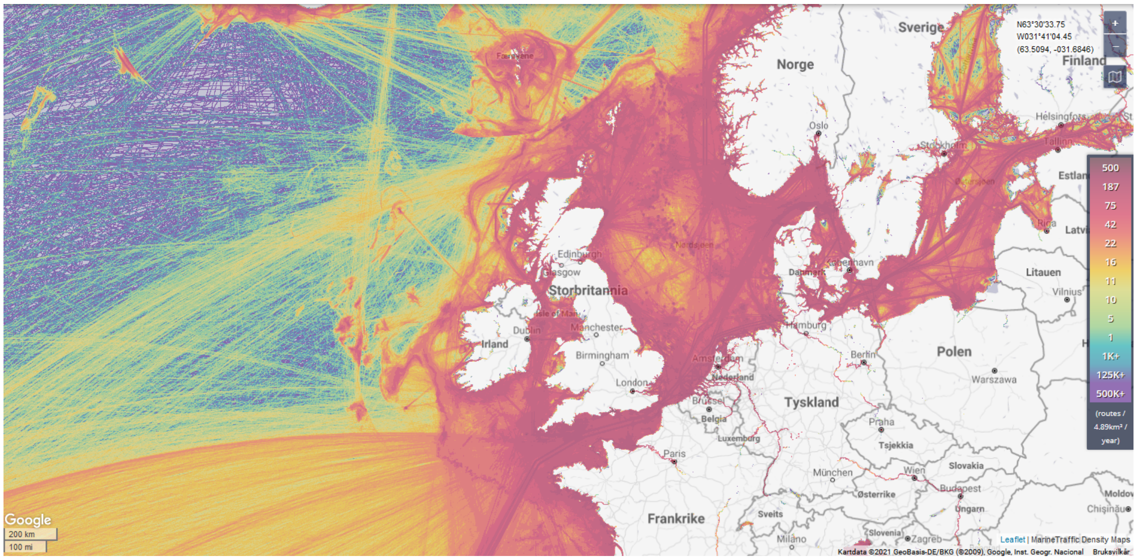

Figure 2.8: Density of maritime traffic (Marine Traffic, 2021).

Another important aspects to consider when evaluating collision risks are that offshore wind farms continue to expand. The size of the farms have almost doubled over the decade and are moving further away from shore, towards deeper waters (WindEurope, 2020b).

The average water depth in 2020 for offshore wind farms under construction was 36m, which is a slight increase from 2019. The average distance to shore has increased notably from 35km to 59km in 2019, but in 2020 it decreased due to the completion of four projects at a distance larger than 90km. These results indicate that the farms will encounter larger and more robust vessels, which might result in catastrophic collisions. OWTs are normally designed to withstand low-speed collisions from service vessels, and therefore, it is uncertain if the OWT can withstand higher speed impacts, larger vessels, or even both.

2.4 Contributing factors and potential consequences to ship collisions

To understand the collision risks, one must look at the factors causing collisions. Dai et al. (2103) list the following causes that may lead to impact between a ship and an OWT:

- Service vessel approaches an OWT:

  - The service vessel fails to stop when it reaches the OWT and hits the OWT at high speed
  - The vessel misjudges a turning or manoeuvring and hits the OWT at relatively low speed
- Service vessel remains alongside an OWT to perform a task related to the OWT:
  - The vessel loses power, or the dynamic positioning system fails, and the vessel drifts into the OWT due to wind and waves. The impact speed depends on the weather and sea conditions

Another important factor is the collision scenarios. The above events can lead to the categories as listed below. Some possible collision scenarios are shown in Figure 2.9.

1. Head-on collision
2. Manoeuvring collision
3. Drifting collision

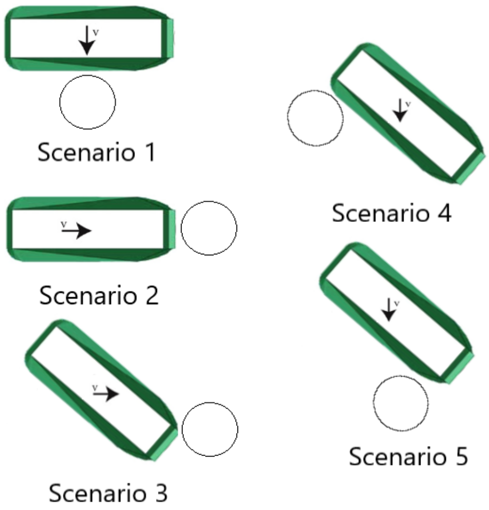

Figure 2.9: Example of ship collision scenarios.

These factors will have different consequences. Depending on the impact speed, the weight of the colliding object, and collision scenarios, the failure mechanisms, i.e., consequences, from a collision can be categorised into consequence classes and are listed below (Presencia & Shafiee, 2016):

- **Not significant** - The ship collision does not impact the wind turbine operation. The wind turbine continues to operate.
- **Considerable** - Wind turbine stops operating, but the damage due to collision is not significant.
- **Serious** - The wind turbine is seriously damaged due to the collision.
- **Catastrophic** - Large parts of the nacelle fall down, which may land on the ship's deck, and the wind turbine collapses.

It is interesting to consider and evaluate the last three, as these can lead to substantial consequences. Standards Norway (2013) defines substantial consequences as a failure of a joint or member that will entail to:

- Danger or loss of human life
- Significant pollution
- Major financial consequences

Classifying a collision scenario into a consequence class must be done correctly as it can have significant outcomes. Therefore, a criterion of failure will directly influence the assessment of collision consequences (Financial Insurance GmbH, 2012).

2.5 Literature review

Previous research on ship collisions with OWT has been explored to obtain knowledge on similar topics. As monopile foundations are of primary interest for this master's thesis, this is what has been mainly researched. The findings and a short description of the investigation are reviewed below.

2.5.1 Head-on collision with 10MW OWT with monopile foundation

Solvik (2020) investigated a head-on collision with a 7,500 tons displacement supply vessel with a bulbous bow on a 10MW OWT. The dimensions of the OWT are identical to the OWT used in this thesis. Impact velocities used were 3m/s and 5m/s. The analysis included the turbine in both parked and operating conditions. Earthquake analysis was also done but will not be discussed due to irrelevance for this thesis work. The LS-DYNA and USFOS set-up can be seen in Figure 2.10 where the ship is represented by a combination of nonlinear and linear springs in the USFOS analysis.

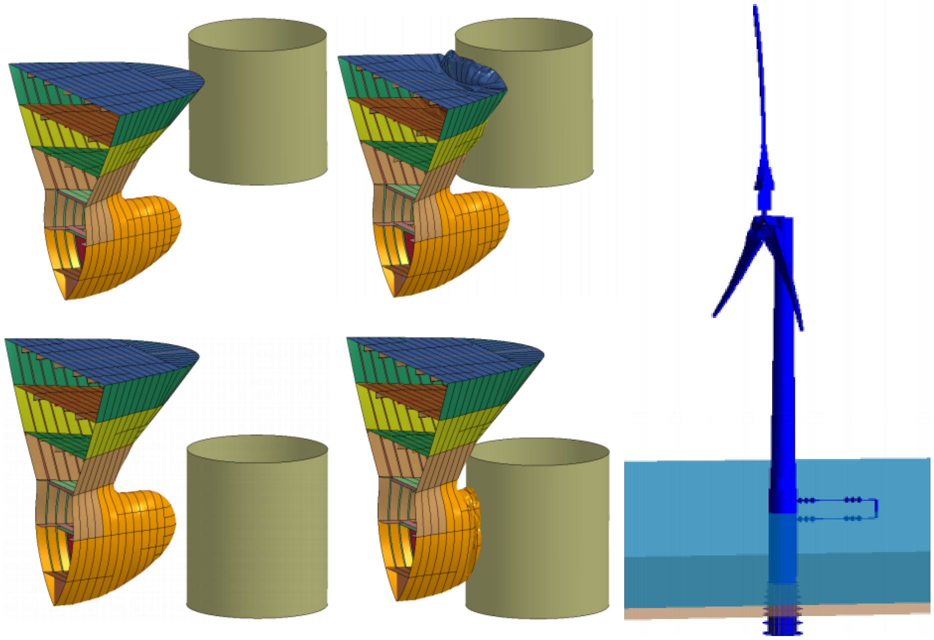

(a) LS-DYNA analysis. **(b)** USFOS impact.

Figure 2.10: Solvik (2020) master's thesis showing the deformation of the forecastle and bulb against the rigid cylinder, and the USFOS model with the spring system to represent impact and soil characteristics.

Solvik (2020) results show that the wind turbine, in general, had high resistance against global collapse. Most critical results showed forces at the bottom section of the tower and acceleration of the nacelle. The utilisation of the soil was higher in the upper layers and considerably lower in the deeper layers. The operating condition positively affected the soil utilisation but had a negative effect on moment forces in the bottom part of the tower.

The most critical scenarios were local buckling in the bottom part of the tower, but it did not collapse. All collapse mechanisms were found desirable as the wind turbine fell away from the vessel. Further evaluation of imperfections with two different methods, namely eigenvalue consideration, and dents, were conducted. The indentation method showed a higher concentration of strain than for eigenvalue method.

2.5.2 Broadside impact collision with a 10MW OWT with monopile foundation

Broersen (2020) investigated the bending moments in the support structure of an OWT subjected to ship collisions. The same vessel and OWT used in Solvik (2020) was used in this thesis, but the ship collides with its broadside. The analysis set-up can be seen in Figure 2.11. The ship collision is represented by a nonlinear and a linear spring in the global analysis. Broersen (2020) collisions were further varied with the direction of the wind by having the collision in parallel to the wind direction, opposite to the wind direction, orthogonal to wind direction, and lastly, no wind at all. Impact velocities from 1m/s to 5m/s were investigated. Different water levels were also investigated but showed marginal effects on the results. Variation in wall thickness was also taken into account.

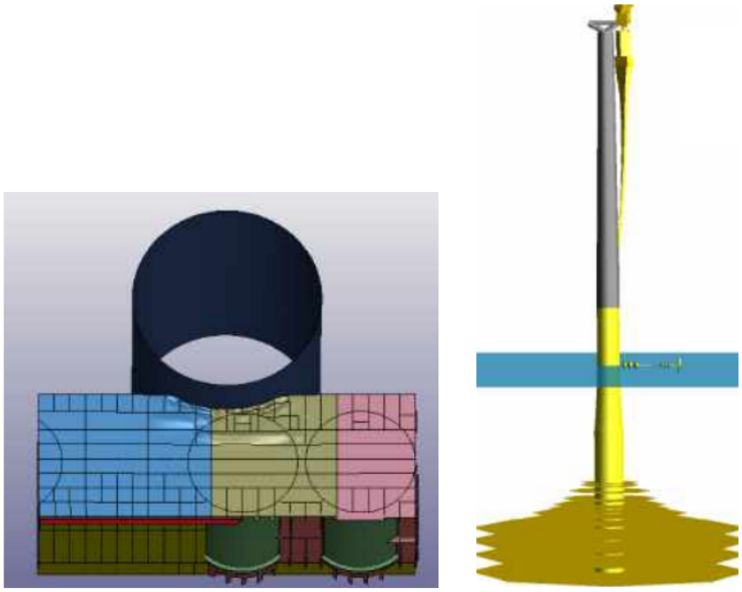

(a) LS-DYNA analysis. **(b)** USFOS analysis.

Figure 2.11: Broersen (2020) master's thesis showing the deformations of the ship section in LS-DYNA and the USFOS model with the soil condition and spring system representing the impact and soil characteristics.

Overturning moments at critical locations were observed to be at the seabed and tower bottom. Maximum bending moments were predominantly found in the first bending mode. Soil deformation showed to have a significant influence on permanent displacement. Wind direction and impact velocity proved to be significant for the maximum overturning moments. The second eigenmode strongly influenced the impact force curve with respect to the shape and period. Input force-time curve of the impacting ship had a considerable influence on the overturning moments. In addition, Broersen (2020) investigated indentations by variation of the wall thickness. A 100mm to 80mm wall thickness reduction showed a significantly larger indentation for the smaller thickness for the same resultant force. The highest moments at seabed were when the impact collision was in parallel with the wind direction, while the lowest was when the wind was in the opposite direction of the impact.

2.5.3 Head-on and broadside collision with a 5MW OWT with a jacket and a monopile foundation

Moulas et al. (2017) investigated both jacket and monopile structure for a 5MW OWT with two different vessel types, namely a utility vessel of 400 tons displacement and an offshore accommodation barge of the same displacement. The analysis set-up can be seen in Figure 2.12. Different collision scenarios were investigated where the vessels collided with the structures at 0° and 45° to the mean wind direction. The investigated impact velocities were 1, 2 and 4m/s.

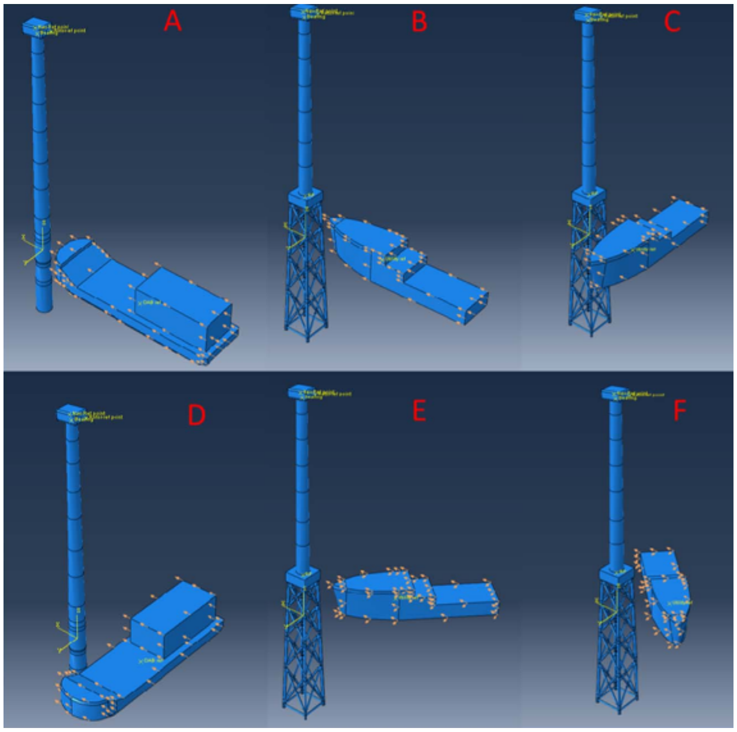

Figure 2.12: Moulas et al. (2017) analysis showing the different ship collision scenarios used.

Moulas et al. (2017) identified that the most critical factors were the collision energy, the height of the vessel, and the area of impact with respect to location according to legs and bracers for a jacket. This was found by investigating different impact angles and velocities. It was found that the indentation and local deformations increased as the impact area decreased. The monopile experienced a deformation close to the seabed for high impact velocities but did not collapse. Bow collision proved to cause the most significant deformation and indentation.

2.5.4 Head-on collision with monopile OWT

Bela et al. (2017) investigated the effects of a rigid striking ship of 5,000 tons displacement to better understand the structural behaviour of an OWT during a collision. Different configurations were used to highlight the modifications in behaviour as a result of changing soil conditions or the loading scenario. Further investigation was done using a deformable ship to examine the influence of the deformability of the striking ship on the OTW's behaviour. The monopile diameter ranged between 4.3 to 5m, the transition piece was 4.3m, and the tower ranged between 3m to 4.3m. The wind was accounted for using wind directions of 0°, which is the same direction as impact force, 90° and 180°. Impact velocities between 1m/s and 5m/s were investigated, three different impact locations on the OTW and clamped base vs soil stiffness modelled with springs were considered.

By only considering a rigid ship, the findings showed that impact velocity greatly impacted the structural behaviour. Tower height impact resulted in higher local indentation than for the monopile impact due to lower tower thickness. Figure 2.13 represents the deformation of the OWT at different impact velocities. However, a lower impact point resulted in lower critical velocity beyond which the OWT would collapse. It was further proved that wind direction influenced structural behaviour. Transverse wind resulted in no significant effect on the response, while the wind of opposite direction resulted in a collapse of lower impact velocity. Worst case, this could lead to the OTW falling directly onto the ship. Soil flexibility needs to be considered in the analysis. Not accounting for this will lead to an overestimation of the plastic deformation of the collided structure.

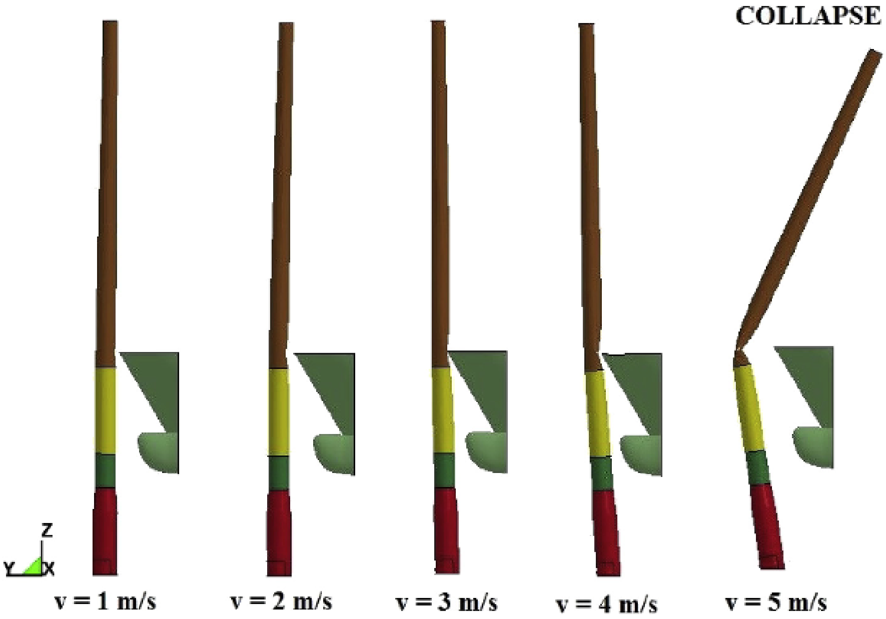

Figure 2.13: Bela et al. (2017) analysis showing the deformed shape of the OWT.

It was further shown that small impact velocities resulted in the striking ship absorbing more energy than the OWT. Contact was only between the bow area and the OWT. Higher impact velocities resulted in more dissipating energy of the OWT by plastic deformations taking place in both the contact area and near the mudline. Here, the bulb would also strike the monopile and dissipate more energy than the bow due to the high rigidity of the bulb. When adopting deformation of the striking ship, the deformations of the OWT are two times smaller, and the structure is able to withstand collisions of higher impact velocity. Lastly, because of the high accelerations at the top of the OWT, the electrical equipment might obtain significant damage even though the OWT structure can resist the collision. Since some electrical equipment is sensitive to high accelerations, this is also of importance.

2.5.5 Method to implement hydrodynamic forces

Decoupled methods are predominately used, meaning the problem is separated into external dynamics and internal mechanics as described in the design principles of this thesis. This method simplifies the effect of fluid as constant added masses. That means that the whole collision system is undamped, and the conservation of momentum principle is used. This allows for fast estimation of dissipated energy with acceptable accuracy. However, added mass is, in reality, frequency dependant. Therefore, Yu et al. (2016) researched the possibility of a coupled method and the accuracy of such a method compared to the decoupled one.

The coupled method implements the linear potential-flow theory in the 6 degrees of freedom (DOF) coupled simulation of ship collision and grounding accidents. The method presents a proposed model that allows for the transient effect of the fluid, global ship motions, impact forces, and structural damage to be predicted with high accuracy (Yu et al., 2016). The simulation is carried out with linear hydrodynamic loads based on linear potential-flow theory for transient conditions without simplifying collision forces. The method is used in the nonlinear finite element code LS-DYNA. This means that 6DOF ship motions can be studied during a collision by coupling the rigid-body motions and structural deformations, i.e., simultaneously predict 6DOF global ship motions and structural deformations.

The paper concludes that the method indicates better accuracy in both external dynamics and internal mechanics. Significant effects of fluid-structure interaction in ship collisions and grounding are captured. Wave loads and hydrodynamic interaction between colliding bodies are not considered, but there is no technical limitation to include them. The external dynamics model only captures the dissipated energy up to the end of the first impact period. That means when, or if, a second impact occurs, the decoupled method is non-conservative. Therefore, the coupled approach should be used to verify the critical cases before using the decoupled method. Lastly, the friction coefficient can significantly influence structural response in ship collisions (Yu et al., 2016).

Chapter 3

Design principles

3.1 General

One of the most important measures one can take to ensure a safe, feasible, and liable structure is to follow standards, regulations, and recommended practices when designing. Guidance for design and which load effects to considered are considered in e.g. DNVGL-RP-C204 (DNV GL, 2020a), DNVGL-ST-0126 (DNV GL, 2018) and NORSOK N-004 (Standards Norway, 2013). When designing a structure, different limit states must be considered. The limit states represent conditions where the structure or structural component beyond this state no longer satisfies the design/assessment criteria (International Organization for Standardization, 2019), i.e., relevant failure modes for the structure shall not exceed the limit state (Standards Norway, 2013). The limit states are as follows:

- Ultimate limit states (ULS).
- Fatigue limit states (FLS).
- Accidental limit states (ALS).
- Serviceability limit states (SLS).

ULS correspond to the maximum load-carrying resistance, FLS correspond to failure due to the effect of dynamic loading, ALS correspond to (1) maximum load-carrying capacity for (rare) accidental loads or (2) post-accidental integrity for damaged structures, and lastly, SLS correspond to tolerance criteria applicable to normal use (DNV GL, 2018). In this case, ALS is of interest as investigation on the OWT is related to ship collision, which is categorised as accidental loads.

Since ALS is to be used, DNVGL-RP-C204: Structural design against accidental loads (DNV GL, 2020a) is highly relevant. The recommended practice gives guidance on how to maintain the load-bearing function of steel structures during accidental events. The goal when designing structures against accidental loads is to avoid accidents disproportional to the original cause. This means that the main safety functions should not be impaired by failure in the structure due to the accidental loads (DNV GL, 2020a). The main safety functions are:

- Usability of emergency exits.
- Integrity of shelter areas.
- Global load-bearing capacity.

Typical accidental events are ship collisions, dropped objects, fire, and explosions, to mention a few. For this project thesis, ship collision and, therefore, ship impact loads are of interest.

The structure should be checked in two steps which is:

1. Loads from the accident on the structure.
2. Recheck structure for ordinary loads in case of reduced capacity towards ordinary loads from the accident.

When checking the structure for ASL, the requirement may be written as:

$$S_d \leq R_d \tag{3.1}$$

where S_d is the design load effect, and R_d is the design resistance. For ASL, the material factor should be taken as 1.0. Alternatively, limit states can be formulated as acceptable deformation based on energy formulation or as usual by force or moment (DNV GL, 2020a).

Ship collision load is characterised by kinetic energy, governed by the ship's mass, including hydrodynamic added mass and velocity of the colliding ship at impact. Depending on the impact conditions, some energy might remain after impact and must be dissipated as strain energy in the installation and, possibly, in the ship. The strain energy dissipation is estimated from the force-deformation relationship between installation and ship. The installation's load-bearing function shall remain intact after impact.

3.2 Energy formulation

DNVGL-RP-C204 states that nonlinear dynamic finite element analysis or energy considerations combined with simple elastic-plastic methods can determine the structural effects of the ship collision. By investigation of strain energy dissipation in the structure, it is convenient to mentioned the three different levels:

- A local cross-section.
- A component or substructure.
- The total system.

The interaction between these levels shall be considered. Strain energy dissipation should further be distinguished between the following and is represented in Figure 3.1:

- Strength design.
- Ductility design.
- Shared-energy design.

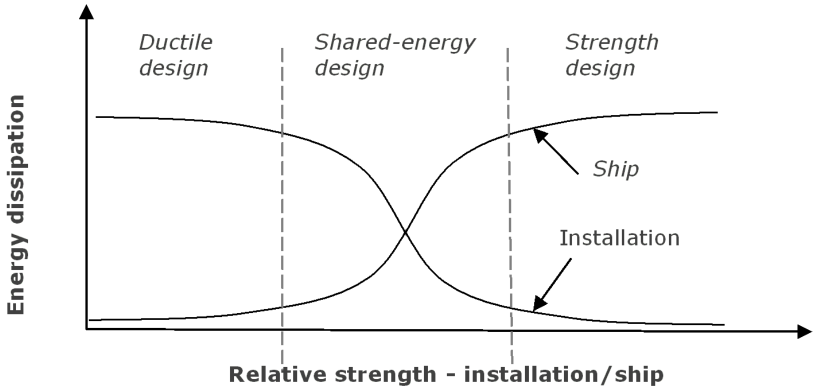

Figure 3.1: Energy dissipation for strength, ductile and shared-energy design(DNV GL, 2020a).

Strength, ductility, and shared energy design are described in DNVGL-RP-C204:

> *Strength design implies that the installation is strong enough to resist the collision force with minor deformation so that the ship is forced to deform and dissipate the major part of the energy. Ductility design implies that the installation undergoes large plastic deformations and dissipates the major part of the collision energy. Shared energy design implies that both the installation and ship contribute significantly to the energy dissipation.*

From a calculation point of view, strength design or ductility design is favourable because the response of the "soft" structure can be calculated based on simple considerations of the geometry of the "rigid" structure (Moan, 2003). For shared design, both the magnitude and distribution of the collision force depend on the deformation of both structures. It would need to be solved incrementally based on the current deformation field, contact area, and force distribution over the contact area (Moan, 2003).

3.3 Collision mechanics

The collision problem is composed of internal mechanics related to large, inelastic deformations at point of contact as well as global hull bending of the vessel and interaction with the surrounding fluid (Moan, 2003). Therefore, fully integrated analysis is relatively demanding and hence, it is found more convenient to split the problem into two uncoupled analysis. The uncoupled analysis consists of:

1. External collision mechanics.
2. Internal collision mechanics.

External collision mechanics deals with global inertia forces and hydrodynamic effects, while internal collision mechanics deals with energy dissipation and distribution of damage in the two structures (Moan, 2003). The dissipated strain energy can be calculated based on the principles of momentum and energy conservation (Verma, 2019). The energy can be estimated using the methods described in Section 3.2. The strain energy to be dissipated from the collision energy for a fixed installation may be taken as shown in Equation 3.2 when a central impact is assumed. This equation represents the external collision mechanics of the system.

$$E_s = \frac{1}{2}(m_s + a_s)v_2^2 \tag{3.2}$$

where:

m_s = ship mass
a_s = ship added mass
v_s = impact speed

The load-deformation relationship, as shown in Figure 3.2, illustrates the structural response of the ship and the installation. The strain energy dissipated equals the total area under this curve, under the condition of equal load, and is given by Equation 3.3. Equation 3.3 is the internal collision mechanics of the system.

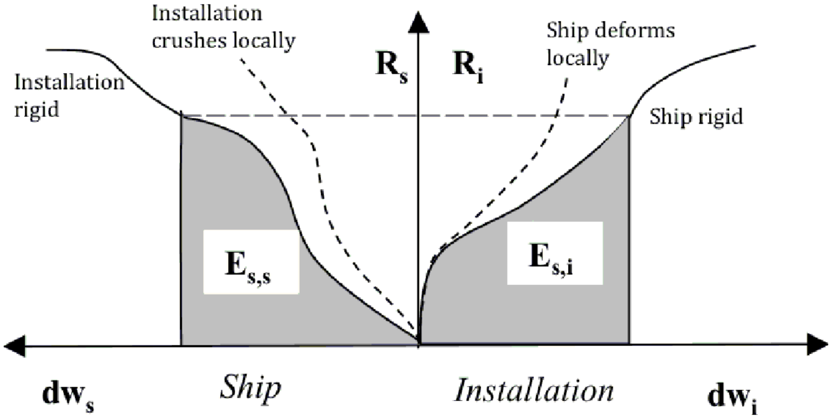

Figure 3.2: Dissipation of strain energy in ship and installation(DNV GL, 2020a).

$$E_s = E_{s,s} + E_{s,i} = \int_0^{W_{s,max}} R_s dw_s + \int_0^{W_{i,max}} R_i dw_i \tag{3.3}$$

where:

$$
\begin{aligned}
E_{s,s} &= \text{dissipated strain energy from ship} \\
E_{s,i} &= \text{dissipated strain energy from installation} \\
R_s &= \text{resistance of ship} \\
R_i &= \text{resistance of installation} \\
dw_s &= \text{deformation of the ship} \\
dw_i &= \text{deformation of the installation}
\end{aligned}
$$

This relationship is often established independently of each other, assuming the other object is infinitely rigid. It is essential to mention that this method has limitations, as both structures will dissipate some energy regardless of the relative strength (DNV GL, 2020a). The more robust structure will experience minor damage while the softer will experience more damage than what Equation 3.3 describes. Hence, the impact force will be distributed over a larger contact area. As a result, the resistance of the more robust structure increases and will cause an upward shift of the resistance curve for the more robust structure. This is represented by the dashed lines in Figure 3.2. To account for the interaction effect between the ship and the installation, an energy dissipation correction factor, β, is implemented as shown in Equation 3.4.

$$E_s = E_{s,s} + E_{s,i} = \beta \int_0^{W_{s,max}} R_s dw_s + \beta \int_0^{W_{i,max}} R_i dw_i \tag{3.4}$$

Force-deformation relationship for standard supply vessels with a displacement of 6,500-10,000 tones is given in Figure 3.3. The different curves are for broadside, bow, stern end, and stern corner impact.

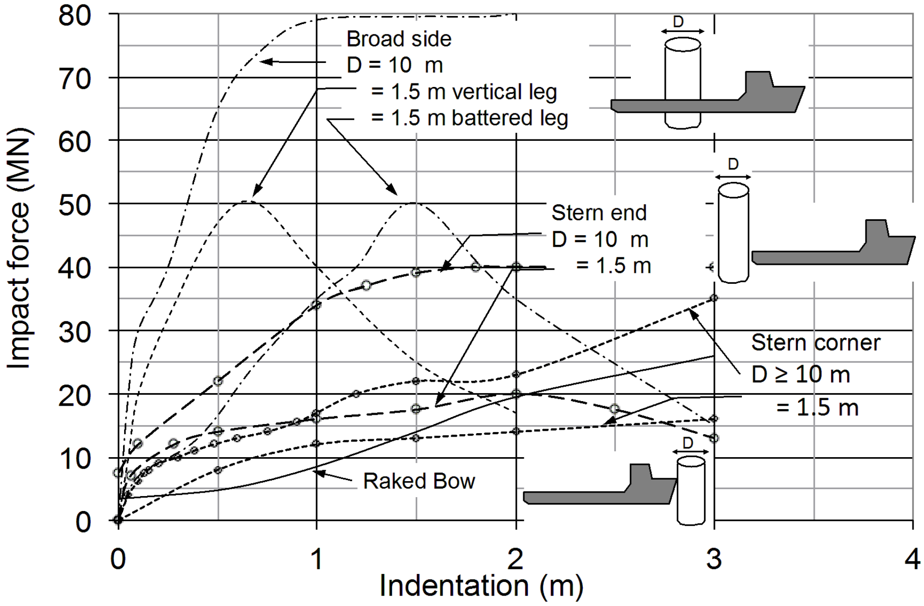

Figure 3.3: Recommended deformation curves for broadside, bow and stern impact(DNV GL, 2020a).

3.4 Buckling of cylindrical shells

DNV GL (2019) gives recommended practice (RP) on how to deal with buckling stability of shell structures based on the load and resistance factor design format (LRFD). If the RP does not explicitly provide buckling checks, a numerical analysis may be done using the finite element method (FEM). The following must then be accounted for:

- Imperfections.
- Material nonlinearities.
- Residual stresses.
- Possible interaction between local and global buckling.

Mesh sensitivity analysis shall also be carried out.

Stiffened and unstiffened cylindrical shells are critical structural elements in offshore structures, and the buckling behaviour is usually more violent than for plate and column structures (Amdahl, 2008). These elements are often exposed to compressive stresses, and therefore, it is crucial to design against buckling criteria. A theoretical load-end shortening curve representative for cylindrical shells subjected to axial compression can be seen in Figure 3.4. The figure shows that during initial loading, the structure will follow a linear primary equilibrium path. At some load level, the stable path will be intersected by an unstable secondary path. This intersection is a bifurcation point and is represented at point B. The buckling mode in the secondary path is quite different for the deformations in the stable and unstable state. Point L is a limit point.

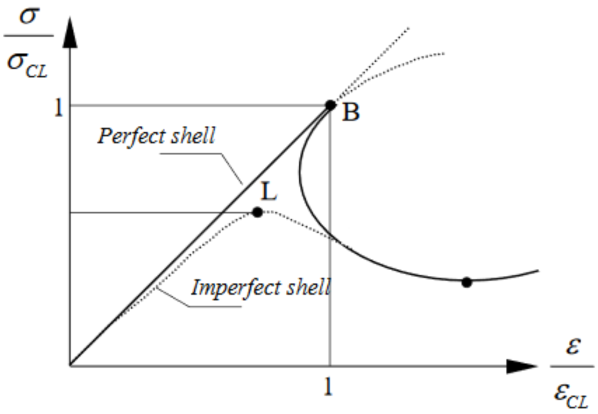

Figure 3.4: Equilibrium paths for perfect and imperfect shells (Amdahl, 2008).

In practice, theoretical bifurcation loads are difficult to reach because of the presence of initial imperfections. The imperfections will lead to the shell failing at a load level significantly smaller than the bifurcation load. Accordingly, the buckling will occur at the limit point, L, rather than the bifurcation point, B.

Small axisymmetric initial imperfection, δ_0, has a tremendous influence on the buckling load, N, of an axially loaded cylinder. This can be seen in Figure 3.5(a). The x-axis is the imperfections as an amplitude of the wall thickness, and the y-axis is the critical buckling load over a theoretical value. The figure further shows that an imperfection of 10% of the wall thickness will reduce the buckling load by 60% of the theoretical value. Figure 3.5(b) represents imperfection sensitivity from experimental buckling loads where a wide scatter of the results are observed. The design of cylindrical shells has to modify the theoretical load by empirical reduction due to this effect. This modification is called the *knock-down* factor.

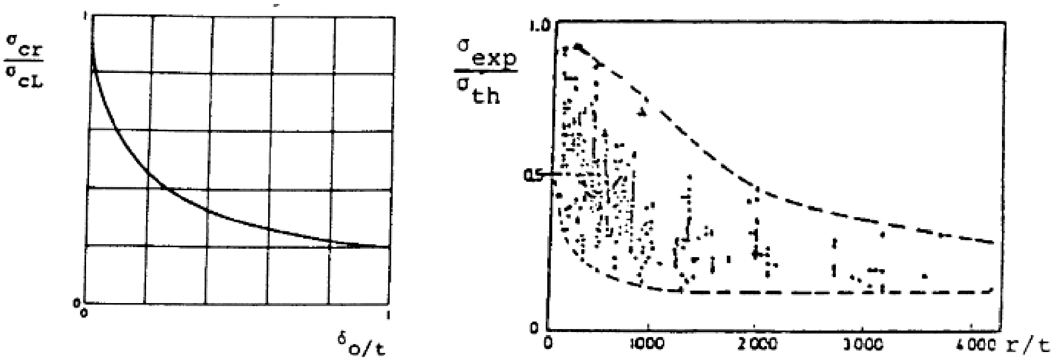

(a)

(b)

Figure 3.5: (a) Influence of axisymmetric imperfections on the buckling load of a cylinder. (b) Experimental buckling loads of axially loaded cylinders (Amdahl, 2008).

Buckling can occur due to a combination of loads such as axial compression, bending, external pressure, torsion, and thermal loads. Usually, this requires interaction formulas to calculate the resistance. However, in this work, bending is dominating. Therefore, simplified formulas are used to determine the buckling resistance when subjected to bending. The below formulas are obtained from Amdahl (2008).

Elastic buckling resistance is found by Equation 3.5.

$$\sigma_{cl} = 0.605\frac{Et}{r} \tag{3.5}$$

Due to the significant effect of initial imperfections, as previously mentioned, the knock-down factor is used to modify the theoretical load. The knock-down factor is given by Equation 3.6.

$$\rho_{kd} = \frac{0.5}{\sqrt{1 + \frac{r/t}{300}}} \tag{3.6}$$

Thus, the elastic buckling resistance accounting for imperfections becomes as shown in Equation 3.7.

$$\sigma_E = \rho_{kd}\sigma_{cl} \tag{3.7}$$

To account for the effects of plasticity, the ϕ method is commonly used with offshore shell structures, where ϕ is a function of reduced slenderness ratio, $\bar{\lambda}$. The reduced slenderness ratio is given by Equation 3.8 and the plasticity reduction factor, ϕ, is given by Equation 3.9.

$$\bar{\lambda} = \sqrt{\frac{\sigma_y}{\sigma_E}} \tag{3.8}$$

$$\phi = \frac{1}{\sqrt{1 + \bar{\lambda}^4}} \tag{3.9}$$

Finally, the elastic critical buckling stress, including effects of imperfections and plasticity, can be formulated by Equation 3.10.

$$\sigma_{cr} = \phi\sigma_y \tag{3.10}$$

3.5 Denting and bending capacity of tubular member

The impact from the ship introduces a local lateral load to the system and will cause denting to the member that has been struck. This is opposed to buckling, caused by axial force in compression or bending that creates axial compression forces. This means that there are two different collapse mechanisms. Collapse load will depend largely on the local plastic deformation. Large plastic deformations can develop in the impact between the OWT and the ship. These collisions are considered a dynamic collision response and should be analysed at the design stage. Elastic-plastic deformation modes of the structural system during a collision can be classified according to Bai and Jin (2016) as:

1. Indentation of the striking ship.
2. Local indentation of the hit member.
3. Overall deformation of the affected structure.

Failure characteristics of a tube are directly associated with the physical boundary conditions of the tube and are therefore essential. Indentation in a struck member will reduce the load-carrying capacity and suffer bending resistance and axial strength loss. This is due to reduced sectional modulus and increased axial load eccentricity. Local dents will transition to global bending and finally lead to global failure (Ong & Lu, 1996).

Nonlinear force-deformation relation is obtained to model the local indentation of a hit tubular member for the global response. This force-deformation relation can be obtained from LS-DYNA. The indentation can then be modelled as a nonlinear spring element in a global analysis, such as USFOS. The collision forces are a function of the relative indentation of the ship and the OWT (Bai & Jin, 2016).

According to DNV GL (2020b), the straightness of members, which are based on buckling calculations according to DNV GL (2019), shall be within the tolerance as given by Equation 3.11. This equation represents the maximum imperfection for a circular cylindrical shell.

$$\delta = \frac{0.01g}{1 + \frac{g}{r}} \tag{3.11}$$

Here, r is the radius of the cylinder, and g is the length of the rod as given in Figure 3.6.

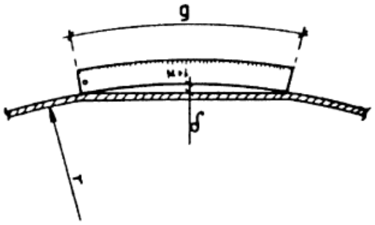

Figure 3.6: Tolerance for straightness and definition of factors used for calculations of maximum imperfections (DNV GL, 2020b).

Nonlinear analysis methods must be able to predict these failures in accordance with recognised failure criteria. That means in addition to modelling stiffness and capacity, yield characteristics, post ultimate behaviour, and ductility limits should also be represented, including local failure modes such as local buckling and local denting. To simulate local buckling, one method is to use a dented tube. This is done by assuming an initial dent and accounting for the growth of the buckle as the member deforms (Moan, 2003). The model is applied for dents imposed by, e.g. accidental loads such as it will be in this thesis. Shell modelling may capture local buckling, but initial geometric imperfections are generally needed to initiate the local buckle correctly.

In summary, the imperfections will always be present to some degree in a structure, causing the cylindrical shells to fail for a lower load level than the bifurcation load. Initial imperfection has a significant effect on the buckling capacity of the cylinder and is included using the knock-down factor. To ensure buckling behaviour such that potential consequences can be studied, the imperfections in the analysis needs to be big enough to trigger the buckling behaviour.

The bending capacity of a dented tubular member is given in DNV GL (2020a). Reduction in plastic moment capacity due to local denting can be seen in Figure 3.7. The flat part of the dented section shown in Figure 3.7 is conservatively assumed non-effective. This gives:

$$\frac{M_{red}}{M_p} = cos(\frac{\theta}{2}) - \frac{1}{2}sin\theta \tag{3.12}$$

where:

$$M_p = \sigma_Y D^2 t$$
$$\theta = acos(1 - \frac{2w_d}{D})$$

Here, w_d equal dent depth, as defined in Figure 3.7, M_{red} is the reduced plastic bending moment of the tube and M_p is the full plastic bending moment. If local denting $\frac{w_d}{D} > 0.5$ the cross-section acts like a hinge as the cross-section is heavily damaged.

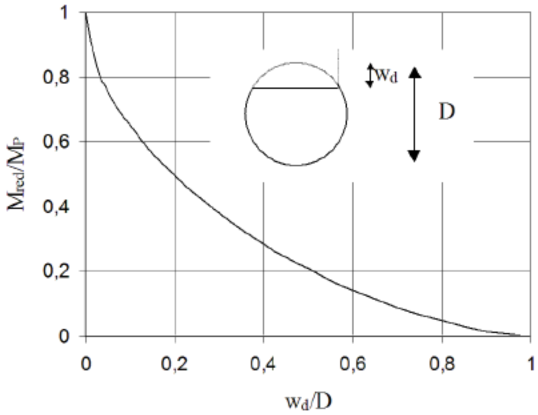

Figure 3.7: Reduction of moment capacity due to local dent (DNV GL, 2020a).

The figure shows that the plastic bending capacity at the point of impact is significantly reduced with an increasing dent. For a dent the size of 1/5 of the diameter, the plastic moment resistance will be half of the initial magnitude before indentation. Therefore, this should be considered during modelling, and critical moments should be investigated.

The monopile and the tower are unstiffened tubes, and the resistance to indentation may be taken from Figure 3.8 or alternatively be calculated from Equation 3.13.

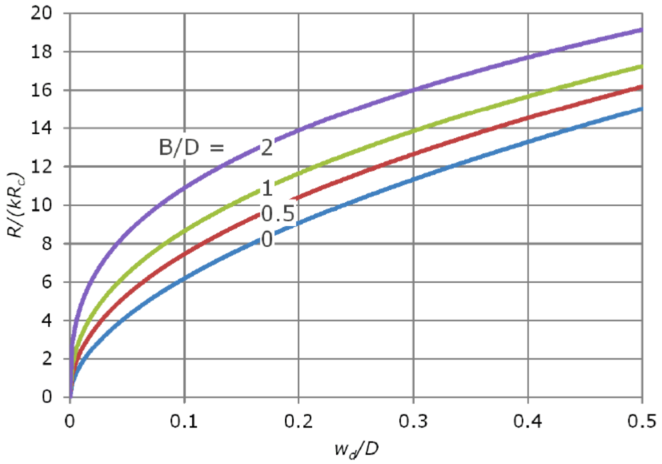

Figure 3.8: Resistance curve for local denting (DNV GL, 2020a).

$$\frac{R}{R_c} = kc_1(\frac{w_d}{D})^{c_2} \quad \text{for:} \quad \frac{w_d}{D} \leq 0.5 \tag{3.13}$$

$$R_c = f_y\frac{t^2}{4}\sqrt{\frac{D}{t}}$$

$$c_1 = 22 + 1.2\frac{B}{D}$$

$$c_2 = \frac{1.925}{3.5 + \frac{B}{D}}$$

$$k = \begin{cases} 1 & \text{if} \quad \frac{N_{Sd}}{N_{Rd}} \leq 0.2 \\ 1 - 2(\frac{N_{Sd}}{N_{Rd}} - 0.2) & \text{if} \quad 0.2 < \frac{N_{Sd}}{N_{Rd}} < 0.6 \\ 0 & \text{if} \quad \frac{N_{Sd}}{N_{Rd}} \geq 0.6 \end{cases}$$

where:

N_{Rd} = design axial compressive force
N_{Sd} = design axial compressive resistance
B = width of contract area
w_d = dent depth
D = diameter of tubular member
t = thickness of tubular member

The curves in Figure 3.8 are inaccurate for small indentation and, therefore, should not be used to verify a design where the dent damage is required to be less than $w_d/D = 0.05$. Theoretically, the width of the contact area may be equal to the height of the vertical plane section of the ship side that is in contact with the tubular member (DNV GL, 2020a).

Chapter 4

Description of reference offshore wind turbine and ship structure

This chapter describes the reference wind turbine (RWT) and broadside ship structure provided by the supervisors. The reference offshore wind turbine structure will be used as the basis for the tower located on top of the monopile. Some minor adjustments will be made to increase the realism of the structure. The second structure provided is the broadside ship structure which is modified to include added mass.

4.1 Reference offshore wind turbine structure

The offshore wind turbine model used in this thesis is based on the DTU 10MW Reference Wind Turbine (RWT) by Bak et al. (2013) which consist of tower, blades, and the rotor-nacelle-assembly (RNA). A brief description is given here, but for a detailed description, reference is made to Bak et al. (2013) as well as Hansen and Henriksen (2013) for the controller.

This RWT is used as it has a traditional design and open access to its structural data, allowing a more straightforward modelling process and comparison and validation of the model. Some modifications and simplifications have been made to reduce computational time and give an increased realistic representation. The key parameters of the RWT are extracted and given in Table 4.1 while the tower dimensions are given in Table 4.2.

Table 4.1: DTU 10MW Reference Wind Turbine key parameters (Bak et al., 2013).

Parameter	DTU 10MW RWT
Wind regime	IEC Class 1A
Rotor Orientation	Clockwise rotation - Upwind
Control	Variable speed Collective Pitch
Cut in wind speed	4m/s
Cut out wind speed	25m/s
Rated wind speed	11.4m/s
Rated power	10MW
Number of blades	3
Rotor Diameter	178.3m
Hub Diameter	5.6m
Hub Height above MSL	119.0m
Drivetrain	Medium Speed Multiple-Stage Gearbox
Minimum Rotor Speed	6.0rpm
Maximum Rotor Speed	9.6rpm
Maximum Generator Speed	480.0rpm
Gearbox Ratio	50
Maximum Tip Speed	90.0m/s
Hub Overhang	7.1m
Shaft Tilt Angle	5.0deg
Rotor Precone Angle	-2.5deg
Blade Prebend	3.332m
Rotor Mass	227,962kg
Nacelle Mass	446,036kg
Tower Mass	628,442kg

Table 4.2: Characteristic dimensions of the OWT tower (Bak et al., 2013). MSL refers to the mean sea level.

Parameter	**Dimension**
Tower height above MSL	115.63m
Tower mass	628,442kg
Tower outer diameter (top to bottom)	5.5m - 8.3m
Tower thickness (top to bottom)	20mm - 38mm
Material (effective) density	8,500kg/m^3

The material for the tower is steel S355. However, the above material density of 8,500kg/m^3 is higher than the given steel's density. This increase is to account for secondary structures inside the tower. The monopile structure is modelled with the same steel but with a density of 7,850kg/m^3 as it is unstiffened.

When modelling the tower, a slight adjustment is made to account for the lack of support structure or soil. Tower thickness is increased by 20% to account for the stiffer supporting structure (Bachynski & Ormberg, 2015). This ensures that the structure is not too soft compared to the stiffer supporting structure and avoid a natural period below the 1P period which is the lowest blade passing frequency (Horn, 2018). Hence, the used modelling tower dimensions are represented in Table 4.3. Modelling specifics will be discussed in their respective chapters subsequently.

Table 4.3: Updated characteristic dimensions of the model OWT tower.

Parameter	**Dimension**
Tower height above MSL	115.63m
Tower mass	628,442kg
Tower outer diameter (top to bottom)	5.5m - 8.3m
Tower thickness (top to bottom)	24mm - 46mm
Material (effective) density	8,500kg/m^3

The RNA masses and their total mass is given in Table 4.4. Detailed modelling of the RNA is unnecessary as it will not affect the response of the OWT to the ship collision. Therefore, the nacelle and hub are represented as nodal masses in the structural model. The hub, drivetrain, generator and nacelle are modelled as pipe elements and given concentrated translational masses for nacelle and hub, and rotational masses for nacelle, hub and generator. The simplified model can be seen in Figure 4.1. The black cylinder on the tower represents the yaw bearing and is referenced as the top of the tower that expands 115.63m above mean sea level (MSL). The material properties are the same as for the tower, except the hub, which has a modified mass with a density equal to 6,530.7kg/m^3. The connection between the hub and the nacelle is modelled by a zero-length spring which is torsion-free but fixed in all other directions due to its large stiffness. This allows for free rotation of the drivetrain. The generator has a maximum torque of 15MNm and a maximum speed of 1.34rad/s, which is 12.8RPM.

Table 4.4: Characteristic dimensions of RNA (Bak et al., 2013).

Parameter	**Dimension**
Blade mass	41,716kg
Hub mass	105,520kg
Rotor (blades + hub)	230,667kg
Nacelle	446,036kg
Total mass of RNA	676,703kg

Figure 4.1: Hub, drivetrain, generator and nacelle represented by pipes.

The design of the blades is based on Blade Element Momentum (BEM) theory with numerical optimisation and are evaluated using Computational Fluid Dynamics (CFD). They are modelled by 20 beam elements each and include prebending. Each blade elements are given specific input values for the cross-section area, torsion moment of inertia, moment of inertia, plastic torsional section modulus, plastic sectional modulus, and shear area in each direction (Solvik, 2020). The prebended blades do not include coning and uses sheared blade shape, meaning each section of the blade sets the x- and y-rotation angles to zero. The prebend ensures tower clearance and gives a clearance of 18.26m without loads. This clearance includes tilt, cone, and prebend of the blades. However, both tilt and cone are neglected due to the simplifications of the RNA as described above, and thus the clearance becomes lower. This will be accounted for when blade tip clearance is investigated. Twist angles are given to each blade section and defined along the blade, and high yield strength is applied to avoid plasticity effects. Wedge-shaped Gurney flaps are used to increase the aerodynamic performance at the inner part of the blade and are implemented using aerodynamic coefficients and mass/stiffness properties. The blades are made from glass fibre reinforced composites and balsa wood that are used as sandwich core material (Bak et al., 2013). Figure 4.2 illustrated the blade shape.

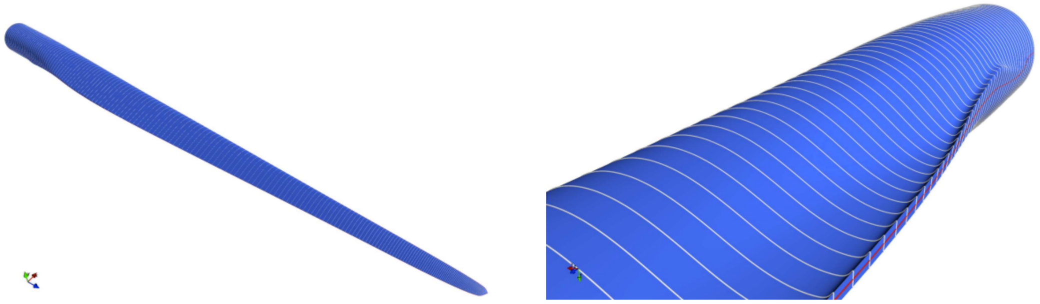

(a) 3D blade shape for the straight blade.

(b) Detailed view of the root of the blade showing the Gurney flaps.

Figure 4.2: Illustration of blades including detailed view of the root of the blade showing the Gurney flaps (Bak et al., 2013).

The basic DTU Wind Energy Controller used in this thesis features both partial and full load operation capabilities. In addition, a switching mechanism ensures smooth switching between the two modes of operation (Hansen & Henriksen, 2013). Classical proportional-integral control theory is used for the partial and full load controllers. Further, mitigation of the influence of rotor speed-dependent variations in the feedback is obtained by filters such as a notch filter and an optional drivetrain damper. The primary feedback sensor is the generator speed. To smoothen the switching between the load operations, the reference generator power is used as a feedback term. The wind turbine is controlled by using the collective blade pitch angle and electromagnetic generator torque.

4.2 Model for broadside ship impact

This thesis looks at a supply vessel with 7,500 tons displacement and is represented by a section of the beam ship side. The beam ship side of a supply vessel is provided by the Department of Marine Technology at NTNU with implemented material properties as shown in Table 4.5. The height of the structure mid-ship is 7.6m, width of 5.5m and length of 15.6m. Shell thickness of the components in the structures varies from 7.5mm to 25mm. The thickness of the side girders in the bilge area is 9.5mm, and the frame spacing is 650mm. Figure 4.3 shows the ship section, where the purple sections indicate the rigid material used to represent the added mass.

Table 4.5: Material properties for ship and OWT.

Parameter	**Ship**
Young's modules, E [Pa]	2.07×10^{11}
Poisson ratio, μ [-]	0.3
Yield stress, σ_Y [Pa]	2.75×10^{8}
Material density, ρ $[kg/m^3]$	7850
Strength coefficient, K [Pa]	7.4×10^{8}
Hardening exponent, n [-]	0.24
Plastic failure strain, ϵ_F [-]	0.15

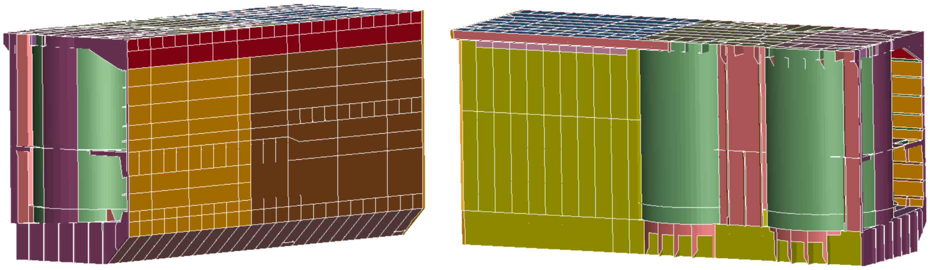

(a) Impact side of the ships. **(b)** Cross-section side of the ship.

Figure 4.3: Broadside ship section from LS-DYNA.

Chapter 5

Local analysis of ship impact in LS-DYNA

This chapter describes the modelling procedure of the OWT in LS-DYNA, which is used to perform a local analysis of the ship impact. A force-deformation curve for a broadside ship impact is of primary interest as this curve is implemented in the global analysis in USFOS to represent the collision event. Lastly, the chapter presents a parametric study investigating key parameters that may affect the dynamic response of the OWT.

LS-DYNA is a general-purpose nonlinear finite element code for analysing the large deformation static and dynamic response of the structure, and the solution methodology is based on explicit time integration (Llivemore Software Technology, 2006). The software is used to investigate the local effects from the ship impact on the OWT by computing the relative strength and deformation of the ship when subjected to an impact. It further determines the level of energy in the ship collision event.

Before starting the modelling, it is beneficial to understand the different aspects that are related to a ship collision—this aid in creating a realistic but efficient model. Simplifications are needed for efficiency, but the analysis needs to provide reliable results of the behaviour of an OWT when subjected to a ship impact. Figure 5.1 displays some essential elements such as components, loads and critical bending moments for the combined system.

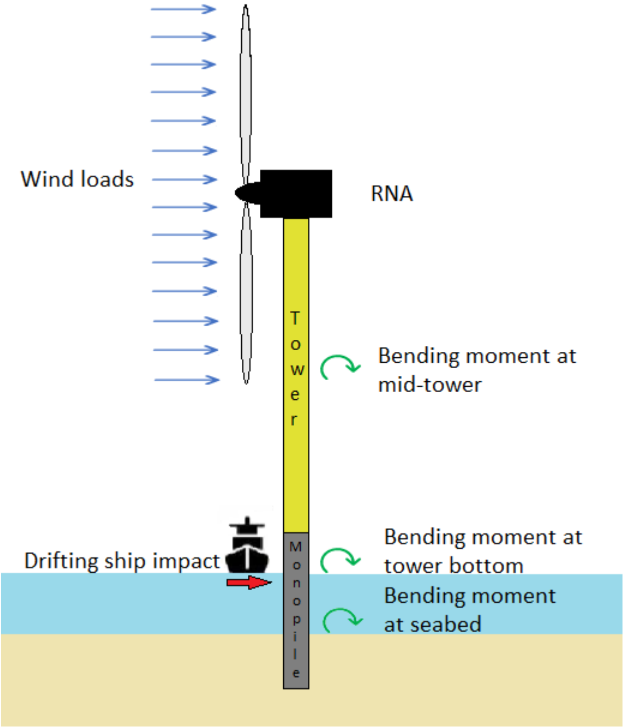

Figure 5.1: Important elements, loads and critical bending moments for the system.

5.1 Shell and beam elements

The shell elements used in the LS-DYNA analysis is the Belytschko-Lin-Tsay shell element formulation which is the default option. This default option is the most economical and recommended to use if no particular features from other formulations are necessary. Additionally, it is significantly more computationally efficient than its alternative, the Hughes-Liu shell element formulation. For a shell element with five through-thickness points, it will require roughly 80% less mathematical operations than the Hughes-Liu element. Thus, the Belytschko-Lin-Tsay shell element formulation is chosen. The shell element formulations are based on a combined co-rotational and velocity-strain formulation (Llivemore Software Technology, 2006).

The beam elements in the analysis use Hughes-Liu beam element formulation, which is the default option. Hughes-Liu element formulation uses cross-section integration.

5.2 Simplified model of the OWT

A simplified model of the OWT is made to reduce computational time and avoid unnecessary modelling, which will not significantly affect the result anyway. The OWT consists of beam and shell elements and a nodal point mass to represent the RNA, hub and blades, and a spring to represent the soil.

The tapered tube representing the tower was divided into constant diameter and wall thickness sections to simplify the geometry. These sections are denoted "beams" in Figure 5.2. The monopile is represented by the shell sections, Beam 1 and the rotational spring. Shell modelling captures critical local effects caused by the ship collision, including membrane, bending, and shear deformation. It is assumed central ship impact, which is conservative as it will give the most energy.

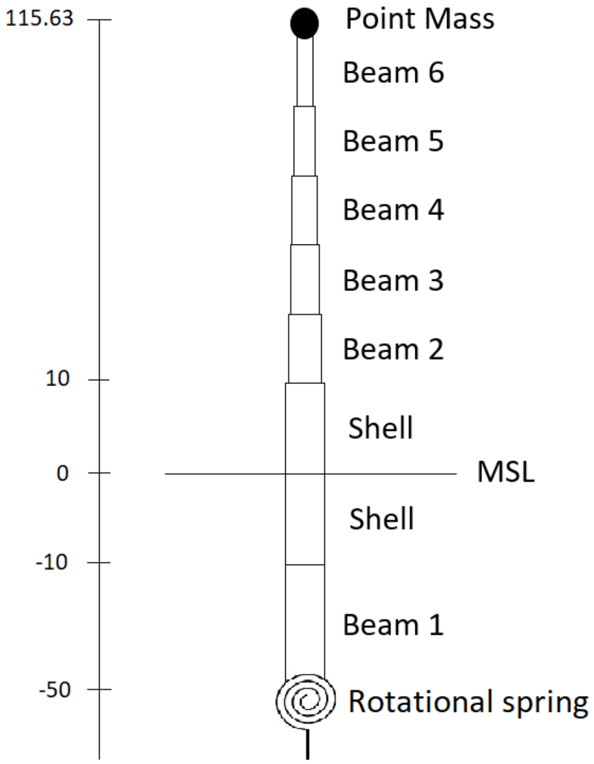

Figure 5.2: Illustration of the simplified model.

Table 5.1 represents the dimensions for the different sections. These average calculations are based on the five sections and the known top and bottom diameter. Some modifications from the RWT is made as it does neither include the support structure nor the soil. This is included to some extent here by increasing the tower thickness by 20% to account for the stiffer supporting structure (Bachynski & Ormberg, 2015) and a rotational spring to represent the soil. A nodal point mass is located at the top of the tower to represent the RNA mass.

Table 5.1: Average dimensions of the OWT tower and monopile.

Section	**Length [m]**	**Average outer diameter [m]**	**Average inner diameter [m]**
Beam 1	40	9.000	8.840
Beam 2	13.126	8.141	8.052
Beam 3	23.126	7.581	7.500
Beam 4	23.126	6.900	6.830
Beam 5	23.126	6.340	6.279
Beam 6	23.126	5.780	5.728
Shell	20	9.000	8.840

The rotational spring is made by a beam element to obtain the desired degrees of freedom (DOF). After the finite element model was created, a connection between the beam elements and shell elements is made. This is done by merging the node at the end of the beam with a node in the centre of the cylindrical shell section's top and bottom. Then, a connection between the nodes on the circumference of the shell top and bottom section with the cylindrical shell section circumference is obtained by again merging the nodes. In addition, a rigid connection was obtained by having a rigid material property at the top and bottom surface of the shell. By applying a rigid material, the connection between shell and beam avoids large deformations. The top and bottom shell section is illustrated in Figure 5.3. The black marks represent the centre of the sections and the connection between beam and shell elements.

Figure 5.3: Shell top and bottom sections.

The OWT's material properties are applied as an isotropic plasticity model with strain rate effects which uses a power-law hardening rule (Livemore Software Technology, 2017). The rigid material has been given the same material properties as the OWT. The material parameter can be seen in Table 5.2.

Table 5.2: Material properties for OWT.

Parameter	**OWT**
Young's modules, E [Pa]	2.1×10^{11}
Poisson ratio, μ [-]	0.3
Yield stress, σ_Y [Pa]	3.55×10^{8}
Material density, ρ [kg/m^3]	7,850 or 8,500
Strength coefficient, K [Pa]	9.0×10^{7}
Hardening exponent, n [-]	0.19
Plastic failure strain, ϵ_F [-]	0.15

The seabed is represented by a linear spring, which is a simplification as the soil gives nonlinear effects. Therefore, it is more common to use nonlinear elastic springs. As mentioned above, the spring is made by creating a beam element by a certain length and material properties. Soil stiffness is determined based on the desire to obtain 1° of rotation in the spring for a thrust force of 1.4MN (Amdahl, J., personal communication, December 7, 2020). The spring stiffness in LS-DYNA is based on the formula $4EI/L$ where E is

Young's modulus, I the moment of inertia, and L is the length of the spring. From this, the spring stiffness is approximated to $1.3 \times 10^{10} Nm/rad$. The spring stiffness could be tuned to fit the desired eigenperiod value. The final characteristics of the spring can be seen in Table 5.3. An eigenvalue analysis is explained hereinafter.

Table 5.3: Spring properties.

Section	**Length [m]**
Length	15m
Outer diameter	1.6m
Inner diameter	1.58m
Material density	$7850 kg/m^3$
Young's modulus	2.50×10^{12}

Lastly, the nodal point mass that represents the RNA, hub and blades is appointed to the top node of beam 6.

5.2.1 Eigenvalue analysis in LS-DYNA

An eigenvalue analysis was conducted to ensure that the correct spring stiffness is implemented. It is desired that the OWT has an eigenperiod for the first mode around 4.5s and for the second mode around 1s. Hence, the spring is tuned by changing Young's modulus in the eigenvalue analysis to achieve this. For a spring stiffness of 1.1E+10Nm/rad the eigenfrequencies and eigenperiods for side-side and fore-aft in Table 5.4 are obtained.

Table 5.4: Eigenvalues.

Mode	**Eigenfrequency [Hz]**	**Period [s]**
1st side-side	0.228	4.39
1st fore-aft	0.221	4.52
2nd side-side	1.273	0.79
2nd fore-aft	1.244	0.80

5.3 Broadside ship section and analysis set-up

The collision into the OWT is a broad ship side collision of a supply vessel. It hits as a central impact, meaning that both centres of mass for the ship and the OWT lies in the line of impact. Further, the kinematic energy is dissipated as strain energy, either plastic or elastic, in the ship and the OWT (Bai & Jin, 2016). This is expected to provide the most unfavourable and conservative collision event. The ship is located in the middle of the shell section and the middle of the ship's width. Figure 5.4 shows the location of the ship section relative to the OWT.

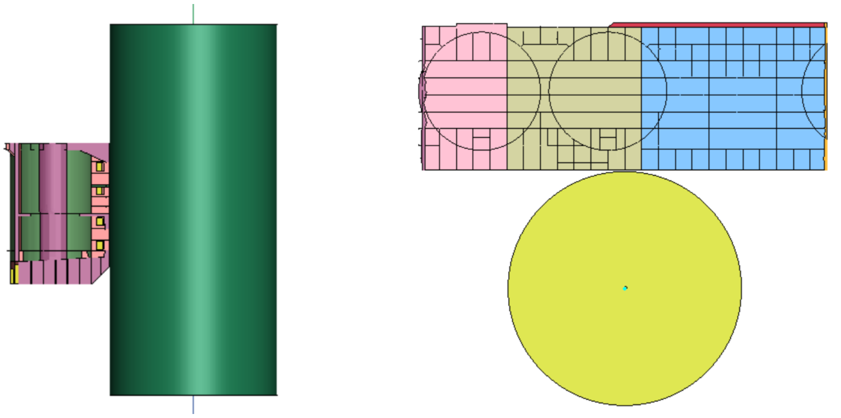

(a) Front view of ship section and OWT.

(b) Top view of the ship section and OWT.

Figure 5.4: Location of the ship section relative to the OWT.

The ship side is modelled with Belytschko-Lin-Tsay shell elements. The ship's displacement is 7,500 tons, and a constant added mass of 40% of this displacement is applied for the broadside ship impact by creating rigid sides with high density to achieve the correct displacement of the ship.

5.3.1 Boundary conditions and motion

Boundary conditions (BC) are given to the bottom and top node of the spring by constraining the bottom node in all displacements while the top node can rotate about x- and y-direction. See Figure 5.6 for coordinate system. The ship side section is constrained in both transverse and longitudinal cross-sectional direction, which can be seen in Figure 5.5, where the black marks represent the applied BC. Regarding the motions of the elements, they are only allowed to move in one direction, which is towards the OWT. That means the elements are only allowed to move in the y-direction and constrained in all other directions.

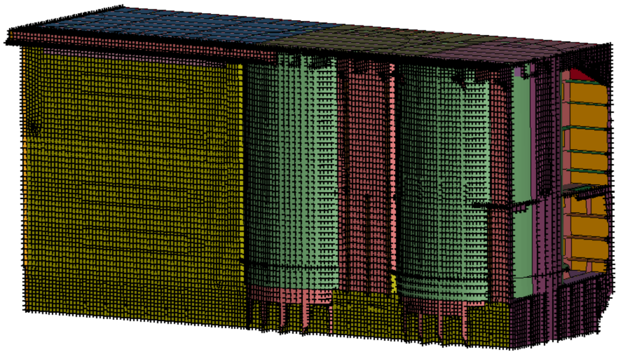

Figure 5.5: Boundary conditions for the ship section.

Constraining the ship section like this will prevent the corners of the ship section from being crushed. The crushing of the corners is not realistic due to the presence of the rest of the ship. However, this solution may hinder the bending of the vessel, which might occur during ship impact.

An initial velocity is generated on the ship section to make the ship move towards the OWT, and the generated velocity is applied to the ship section as a part. Two schemes of contact conditions are used in the analysis; self-contact and master-slave contact. The self-contact is applied only to the ship to enable contact between parts of the bodies if they were to deform onto themselves. The master-slave contact acts as the main contact between the vessel and the OWT. In LS-DYNA, these contacts are defined as automatic single surface (self-contact) and automatic surface to surface (master-slave) contacts. Static contact friction is set to 0.3 for all contacts (Yu et al., 2019).

The complete system of a drifting broadside central ship impact with an OWT can be seen in Figure 5.6 and includes the coordinate system in LS-DYNA.

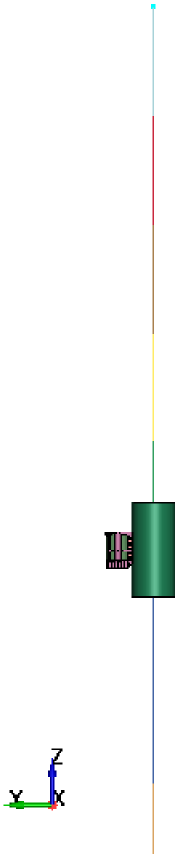

Figure 5.6: Complete model including the coordinate system.

The final step is to run the analysis. The computational capacity required to run this analysis is significant, and for a regular computer, this can take days. Thus, a supercomputer is needed to conduct the analysis. It was granted computational time on the supercomputer *Fram* allowing for a reduced computational time from days to only a few hours. The deformed ship section and OWT can be seen in Appendix A and B for impact velocities of 2m/s and 3m/s, respectively. The von Mises stress can be seen in Appendix C and D, and effective plastic strain can be seen in Appendix E and F for impact velocities of 2m/s and 3m/s, respectively. Appendix A shows how the web frame crushes and ends up buckling. Appendix C and D shows how the material of the OWT is yielding while Appendix E and F indicates how the effective plastic strain grows when the material is actively yielding.

5.4 Force-deformation curve and impact energy

As previously mentioned, the force-deformation curve is needed to conduct the global analysis in USFOS. It is obtained by the reduced diameter of the OWT and adding it together with the reduced width of the ship, which will give the total deformation. This is the case when neither of the structures is assumed infinitely rigid. This is then plotted against the total impact force. The curve is interpolated to achieve a discrete number of points used as input in USFOS. Figure 5.7 shows the force deformation curve while Table 5.5 shows the discrete points.

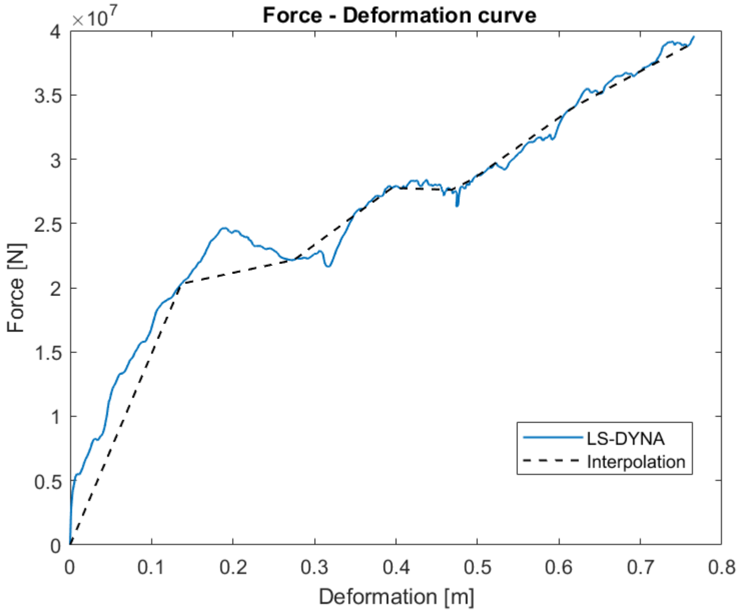

Figure 5.7: Force-deformation curve for broadside impact.

Table 5.5: Force-deformations points used in USFOS for an impact velocity of 2m/s.

Force[MN]	Deformation[m]
0	0
20.31	0.137
22.16	0.275
27.76	0.395
27.09	0.468
28.47	0.495
34.11	0.620
38.85	0.759

The design initial impact energy for 2m/s is 21MJ based on Equation 3.2. The impact energy, i.e. kinetic energy, can be seen in Figure 5.8. As seen from the figure, there is good correspondence with the design initial impact energy and what is obtained from LS-DYNA. There is no kinetic energy before the impact, and after impact, the kinetic energy oscillates around 3.5MJ. The reduction of kinetic energy is the transformed collision energy into strain energy in the deformed structures. The remaining energy is due to the OWT moving back and forth after impact.

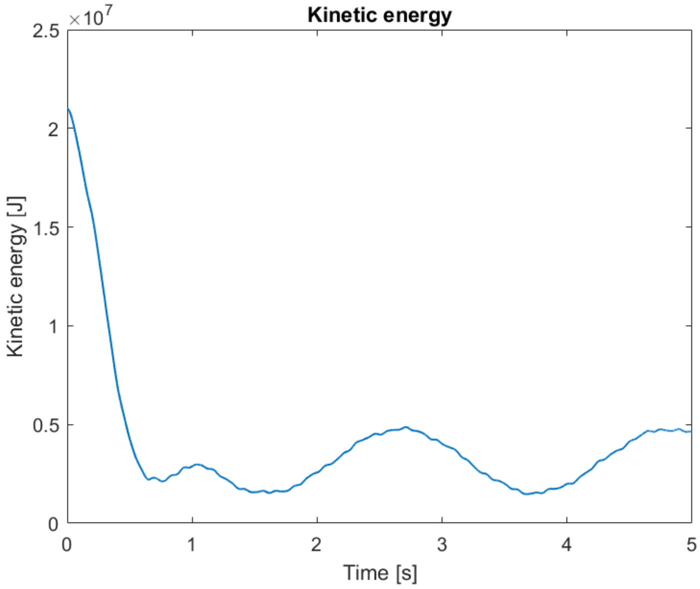

Figure 5.8: Kinetic energy for an impact velocity of 2m/s.

5.5 Parametric study with increased impact velocity, monopile thickness and monopile yield strength

A parametric study is conducted to investigate the effects on the dynamic response of the OWT. Three cases are studied and are as follows:

- Increased impact velocity of the ship collision from 2m/s to 3m/s.
- Increased monopile wall thickness from 80mm to 100mm.
- Increased monopile yield strength from 355MPa to 455MPa.

The three study cases will first be presented by their force-deformation curves along with a discussion before a comparison of the dynamic responses of the three are evaluated.

5.5.1 Impact velocity increased to 3m/s

The first parametric study is the investigation of the effects of higher impact energies. The impact velocity of 3m/s is chosen as it is a realistic impact velocity during drifting impact collisions. The monopile wall thickness and yield strength will remain the same, i.e. 80mm and 355MPa.

Figure 5.9 shows the force-deformation curve with interpolated points. The interpolated points are displayed as this study case will be used later on. This will become clearer after reading the comparison of the three study cases. As expected, the force and deformation have increased due to a larger impact energy resulting in more strain energy needing to be dissipated. The impact energy for an impact velocity of 3m/s is 47MJ. Table 5.6 shows the discrete points which will be used as input in USFOS.

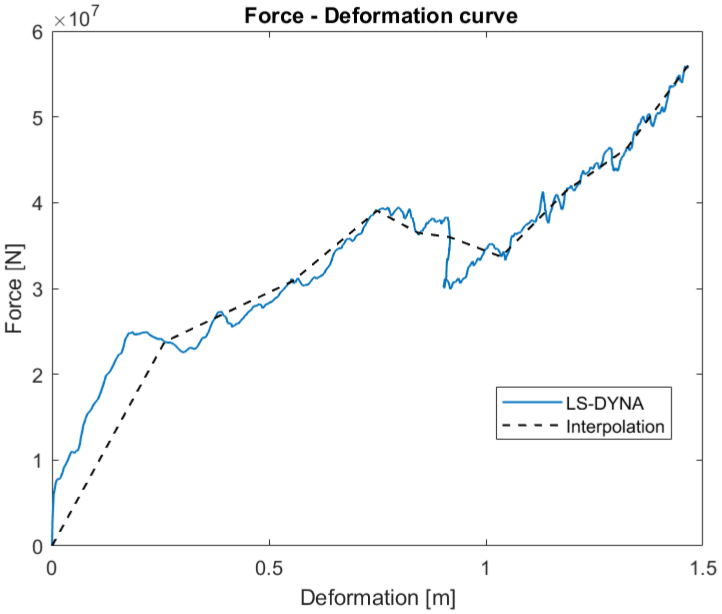

Figure 5.9: Force-deformation curve for broadside impact with increased velocity.

Table 5.6: Force-deformations points used in USFOS for impact velocity of 3m/s.

Force[MN]	Deformation[m]
0	0
23.78	0.260
30.86	0.555
39.06	0.749
36.49	0.843
35.97	0.917
33.70	1.035
41.44	1.186
46.28	1.324
55.97	1.466

5.5.2 Monopile wall thickness increased to 100mm

The second parametric study is to investigate the effects of the increased wall thickness of the monopile. The wall thickness is increased to 100mm while the impact velocity is

2m/s and the yield strength is 355MPa. Figure 5.10 illustrates the force-deformation curve when the monopile thickness is 100mm. The force and deformation are lower than both the previous cases, which is expected due to the additional material, resulting in increased strength due to a larger area to distribute the forces.

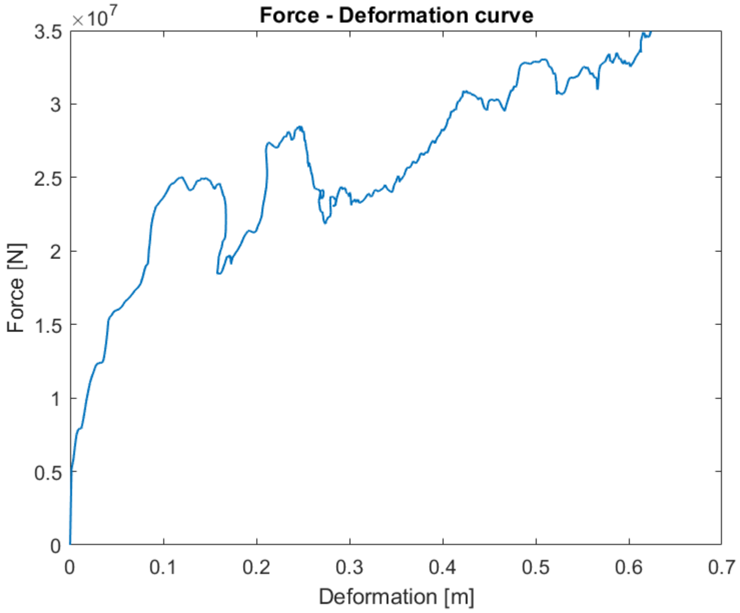

Figure 5.10: Force-deformation curve for broadside impact with increased wall thickness.

5.5.3 Monopile yield strength increased to 455MPa

The third parametric study is the effect of increased yield strength of the monopile material. The yield strength increases to 455MPa while the impact velocity is 2m/s and wall thickness is 80mm. Figure 5.11 illustrates the force-deformation curve when the monopile yield strength is 455MPa. It can be seen that the force-deformation curve is similar to that of the increased thickness but with more significant deformations. This is due to the elastic part of the stress-strain curve that increases, meaning the stress-strain curve will decrease at a higher magnitude than with lower yield strength. Thus, the strain increases, which gives higher deformation.

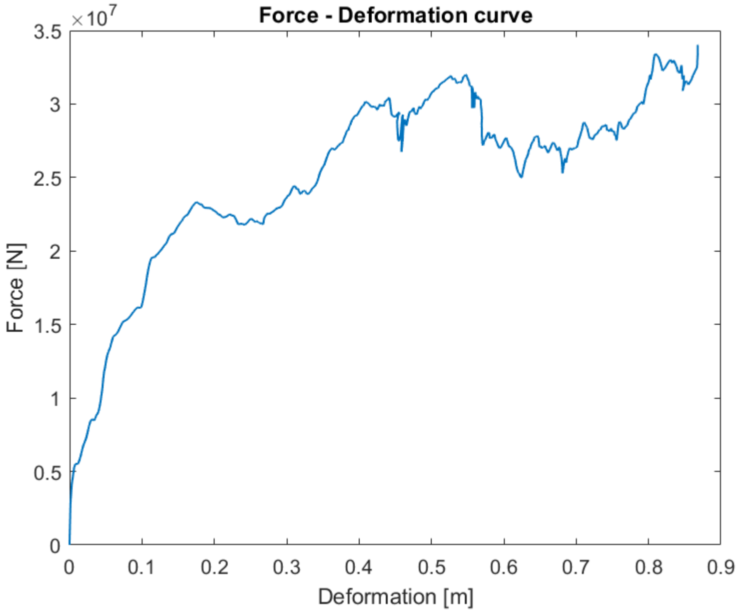

Figure 5.11: Force-deformation curve for broadside impact with increased yield strength.

5.5.4 Comparison of LS-DYNA results from parametric study

Some key parameters are studied to evaluate the response of the OWT between the three cases. These are kinetic energy, acceleration and displacement of tower top, and the most significant moment at the bottom of the OWT.

As discussed briefly, the impact energy, i.e. the kinetic energy, will increase with increasing impact velocity. Figure 5.12 shows the kinetic energy for the three cases, where the impact velocity equal to 3m/s results in 47MJ while impact velocity equal to 2m/s equal to 21MJ. It is observed that the remaining energy is slightly lower for the higher yield strength.

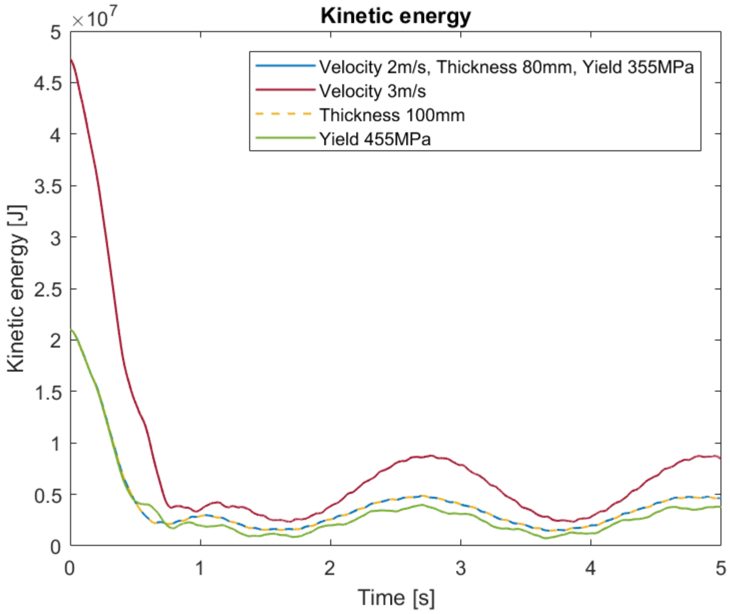

Figure 5.12: Kinetic energies for the parametric study.

Larger impact energy will lead to larger acceleration amplitudes which can be seen in 5.13. Increased wall thickness results in slightly larger accelerations at the beginning than that of lower wall thickness but then stabilises to a lower accelerations magnitude. There is a slight increase in the acceleration for the higher yield strength compared to that of lower yield strength and lowest wall thickness. The most significant accelerations are found for the most considerable impact energy marked red in the figure below, followed by the increased yield strength marked green, which again is followed by the initial run marked blue. The lowest acceleration is found for the case with the highest wall thickness marked yellow in the figure.

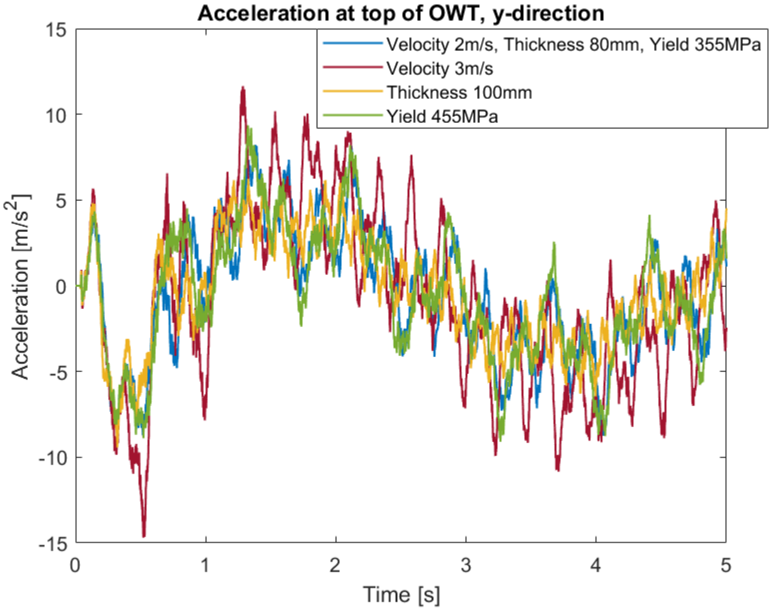

Figure 5.13: Acceleration at OWT top for the parametric study.

The displacement at the top of the OWT can be seen in Figure 5.14. The most significant displacement occurs for the most considerable impact velocity, while the lowest displacement occurs for the highest wall thickness. This is due to the additional material area, which provides more stiffness to the system.

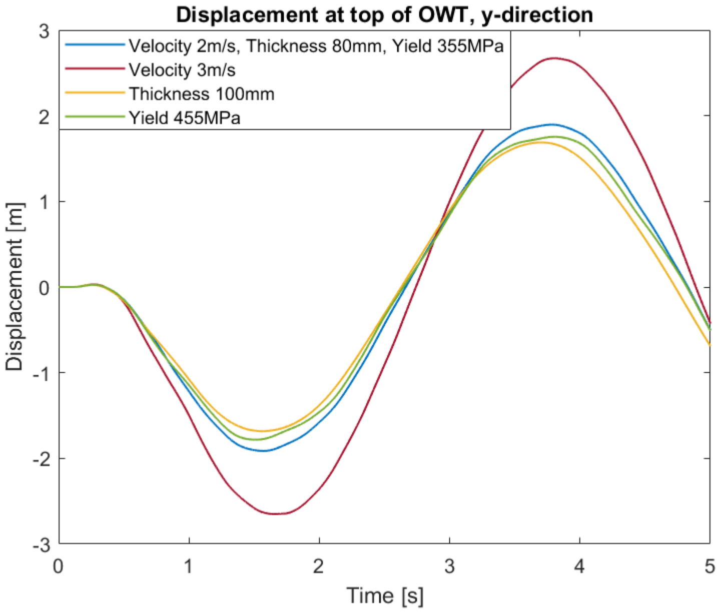

Figure 5.14: Displacement for OWT top for the parametric study.

Lastly, the moment at the bottom of the OWT is investigated as this is the largest moment. Figure 5.15 illustrated the moments for the different cases. As expected, the largest impact velocity results in the largest moment, while the increased yield strength results in the average lowest moment. The increased wall thickness and initial case, i.e. the blue line, shows similar average values of the moment.

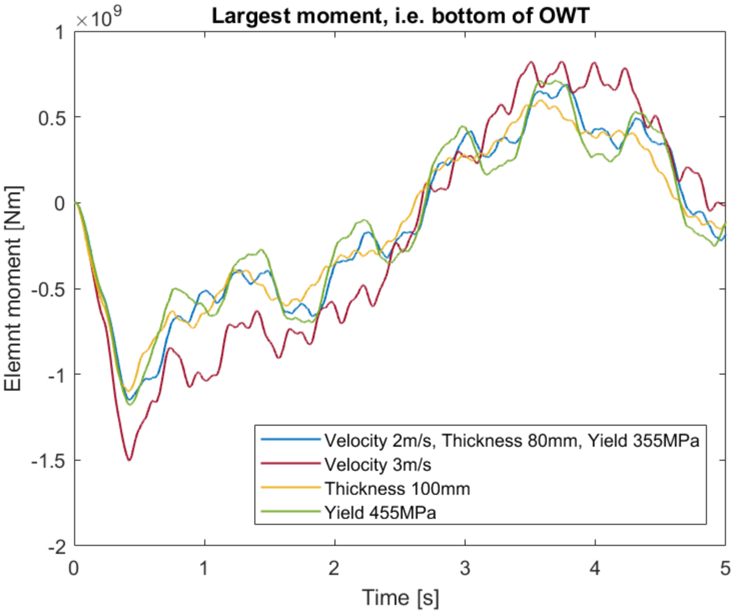

Figure 5.15: Largest moment in the OWT, which is located at the bottom of the OWT, for the parametric study.

Based on the above discussion, it is concluded to perform global analysis on the impact velocities of 2m/s and 3m/s, where the wall thickness is equal to 80mm, and the yield strength is equal to 355MPa. This is due to the significant difference between the two cases.

Chapter 6

Modelling for global analysis in USFOS

This chapter describes the modelling procedure of the OWT and ship model in USFOS. The modelling descriptions include modelling of the environmental loads, tower, soil conditions, ship impact and shell section with imperfections. An eigenvalue analysis of the complete system is presented at the end of the chapter.

USFOS is a software program used for collapse and accidental load analysis for fixed offshore structures. The software is based on simple engineering concepts and combines classical, analytical solutions, accurate numerical procedures and conventional finite element formulations (USFOS Reality Engineering, n.d.).

6.1 Modelling of environmental and applied loads

The main contribution to the applied loads is the gravitational loads on the body, the torque rotating the blades, and the loads on the blades generated from the wind. The environmental loads are the waves and the wind. A dummy wave is applied with zero wave height to represent the sea surface, and thus the effect of wave loads are not considered. The waves are input as Airy wave theory, and the wind field is uniform with a wind velocity of 10m/s.

6.2 Modelling of OWT tower

The tower used for the USFOS modelling is that of the DTU 10MW RWT with some small adjustments as mentioned in Chapter 4, Section 4.1. Compared to the LS-DYNA model, the tower now consists of tapered beam pipes, i.e., a variable cross-section. This is to obtain increased realism of the OWT as the RNA, hub, and blades will now be included in the structural model. The main characteristic dimensions of the OWT tower is given in Table 4.2 in Chapter 4, Section 4.1. Figure 6.1 shows the tower with the RNA, hub, and blades.

Figure 6.1: Tower with RNA, hub, and blades.

6.3 Modelling of soil conditions

Geotechnical design and procedures for developing soil models are complicated and require their own field of research. Therefore, only a brief description and a simplified method will be presented. Soil exhibits nonlinear behaviour and thus should be accounted for. Not accounting for soil flexibility means the plastic deformation of the collided structure will be overestimated (Bela et al., 2017).

Kühn (2001) presents three different methods to represents the soil stiffness. These are a distribution of lateral springs along the length of the monopile, apparent fixity length, and lastly, rotational spring, and possibly, in addition, a translation spring. The different methods can be seen in Figure 6.2. Using the distribution of springs along the length of the monopile provides the most accurate results but require more computational time (Sørum, 2017). The apparent fixity length assumes the length below the seabed is rigidly clamped to obtain the same fundamental eigenfrequency. The rotational spring represents the soil stiffness but will give no information of the response below the seabed. The two latter methods are used during preliminary design to make crude estimates, while the distribution of springs is used in the final stage to model the subsoil behaviour correctly.

For this thesis, a simple rotational spring is used to represent the soil stiffness. This is to simplify the modelling procedure.

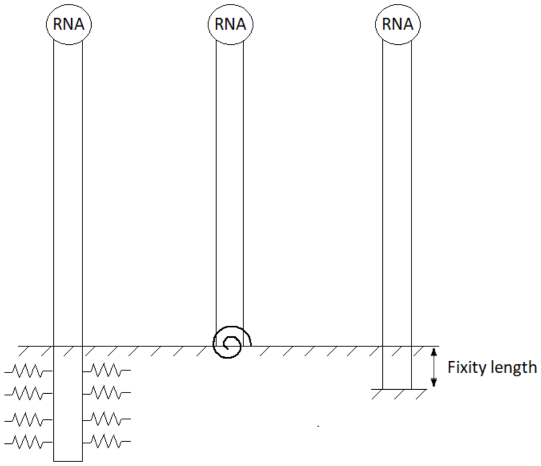

Figure 6.2: Methods to represents soil stiffness. Distributed spring (left), rotational spring (centre) and apparent fixity length (right).

The monopile is modelled using the same method as the tower since the seabed and soil behaviour is represented by a rotational spring.

Again, to obtain the desired eigenperiods of the OWT, an eigenvalue analysis is conducted to find the spring stiffness. For the simplified model where a point mass represents the RNA, hub and blades, the spring stiffness needs to be 1.8E+11Nm/rad to achieve the desired eigenperiod of 4.5s for the first mode and 1s for the second mode. Table 6.1 display the eigenperiods achieved for the simplified USFOS model without the RNA, hub and blades. A complete eigenvalue analysis with the RNA, hub, and blades will be discussed at the end of this chapter.

Table 6.1: Eigenperiods in USFOS for simplified model where the RNA, hub and blades are represented by point mass compared to LS-DYNA.

Mode	**USFOS eigenperiods [s]**	**LS-DYNA eigenperiods [s]**
1st side-side	4.51	4.39
1st fore-aft	4.51	4.52
2nd side-side	0.77	0.79
2nd fore-aft	0.77	0.80

6.4 Modelling of ship impact

As previously mentioned, the collision scenario is a broadside collision of a supply vessel. It hits as a central impact which is expected to provide the most unfavourable and conservative collision event. The ship impact will occur in both parked and operating condition. In USFOS, the ship impact is modelled by a spring system containing a linear and a non-linear spring located at the mean sea level (MSL). Figure 6.3 shows the spring system representing the broadside impact.

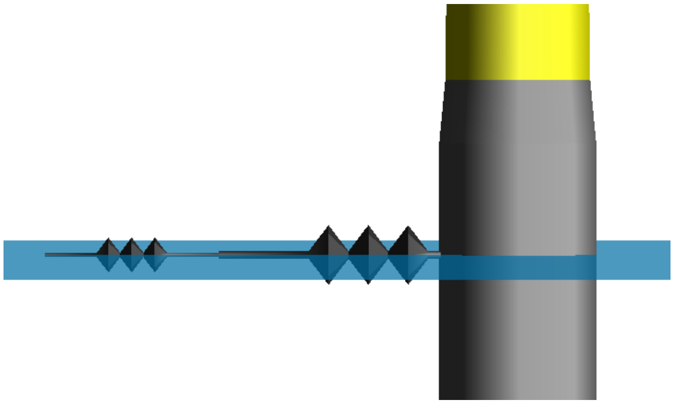

Figure 6.3: Spring system representing the ship collision. Consist of one nonlinear spring and one linear spring.

The nonlinear spring contains the force-deformation curve obtain from LS-DYNA and represents the true stiffness of the ship. This spring has a point mass representing the mass of the ship and an initial velocity to initiate the impact. To ensure the ship disconnects from the OWT, a linear spring is used. The linear spring is given a low to zero stiffness in tension and a large stiffness in compression of 100MN/m. This ensures no energy is dissipated in the spring and that the spring force is close to zero as the ship gets pushed back by the resistance of the OWT.

The complete OWT model and characteristic lengths are shown in Figure 6.4.

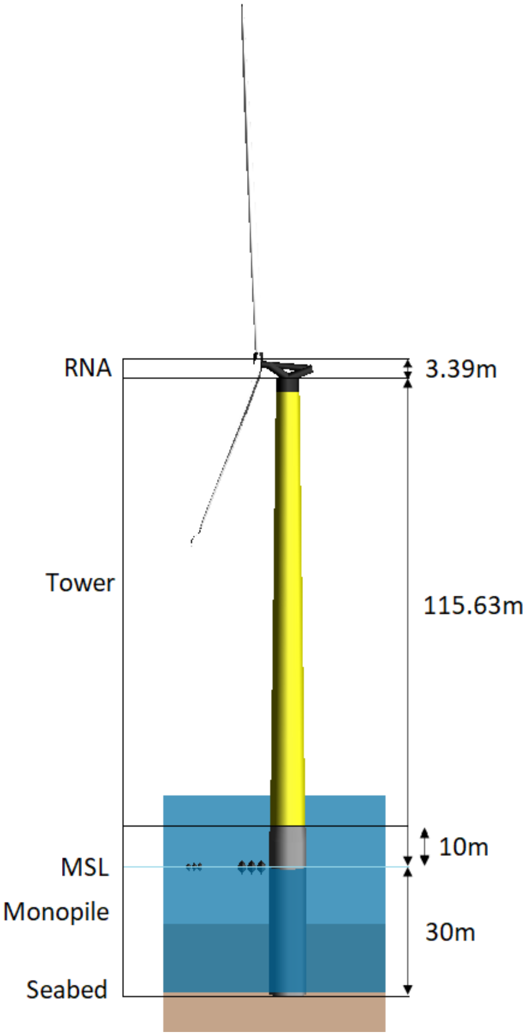

Figure 6.4: Complete USFOS model of the OWT with characteristic lengths.

6.5 Modelling of shell and imperfections

To investigate critical areas for buckling, shell elements are modelled to capture the local effects. Critical areas mean that there is a high utilisation factor with respect to the buckling capacity. Buckling capacity was discussed in Chapter 3, Section 3.4. To locate the critical areas, the global analysis is investigated based on the beam model in USFOS. By investigating the axial and von Mises stress, seen in Appendix G, it can be seen that the most critical areas were at the seabed and the midsection of the tower of the OWT. Only the midsection of the tower is investigated as it is here the majority of the largest stresses occur. In addition, the knock-down factor is smaller, which provides a lower elastic buckling resistance. Hence, this area is more critical. This will be further discussed in Chapter 8.

Consequently, this area is isolated and converted to shell elements to investigate potential buckling. USFOS provides an easy conversion between beam elements and shell elements by using the integrated function SUBSHELL. This function allows for user-specified elements to be automatically replaced by newly generated shell elements. The properties of the beam element will be transferred to the shell elements. To adjust the mesh density, another integrated function is used which is the MESHPIPE. A coarse mesh of 20cm×20cm is used for the buckling analysis to reduce the computational time. The length of the shell section is 5m. Figure 6.5 shows the location of the shell section and a close-up that illustrates the mesh of the section.

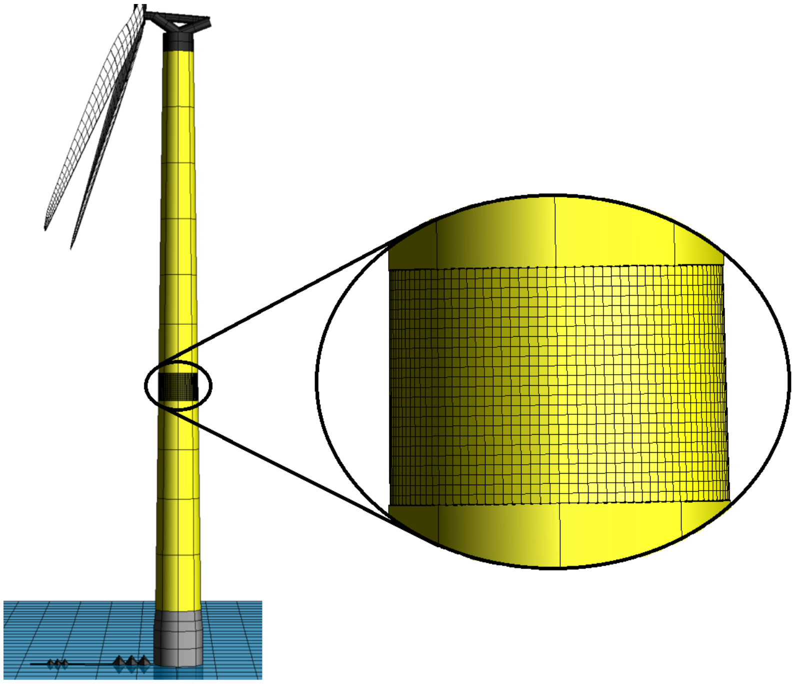

Figure 6.5: Shell section located at the midsection of the tower.

To account for imperfections, the integrated function BUCKMODE is used. The function applies initial imperfections by performing an eigenvalue analysis of the shell model. The eigenmode will then be scaled and added to the initial nodal coordinates of the model. To determine the scale factor, one has to go back to the discussion made in Chapter 3, Section 3.5 about denting and bending capacity of the tubular member. Here, the straightness tolerance is discussed based on DNV GL (2020b) and the maximum imperfection for a circular cylindrical shell which is given by Equation 3.11. The radius, r, is 3.64m, and the length of the rod, g, is estimated to be 2.86m based on eight half-waves in the circumferential direction. This results in a maximum imperfection, δ_0, of 16mm. It should be noted that the length of the section and the boundary conditions may affect the realism of the imperfections. Additionally, BUCKMODE is stiffer in the longitudinal direction than that of the transverse direction. Figure 6.6 shows the shell section with imperfections, scaled up for visualisation purposes.

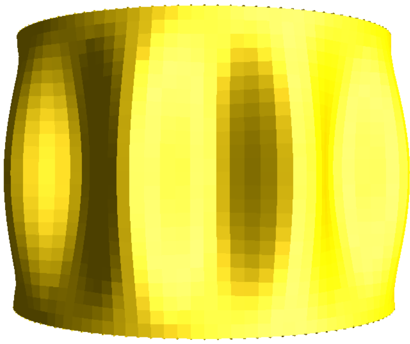

Figure 6.6: Imperfection representation using BUCKMODE. Scaled up for visualisation.

6.6 Eigenvalue analysis in USFOS of the complete OWT

An eigenvalue analysis is performed with the RNA, hub, and blades to ensure the eigenperiods is within the desired range. Table 6.2 shows the obtained eigenperiods for the system with the detailed turbine, i.e. with RNA, hub, and blades, with a nodal point mass representing the RNA, hub, and blades and from LS-DYNA. As can be seen, there is a slight increase in the eigenperiods when the RNA, hub, and blades are included in the model. This is likely due to additional mass for when the RNA, hub, and blades are correctly represented and not only represented as a nodal point mass. The difference is

45.6 tones between the two representations of the system. Additionally, the eigenmodes of the blades may contribute. Figure 6.7 illustrated the eigenmodes for the OWT with the RNA, hub, and blades.

Table 6.2: Eigenperiods in USFOS for simplified model with RNA and hub compared to LS-DYNA.

Mode	**USFOS eigenperiods [s] with RNA, hub, and blades**	**USFOS eigenperiods [s], RNA, hub, and blades as point mass**	**LS-DYNA eigenperiods [s]**
1st side-side	4.79	4.51	4.39
1st fore-aft	4.84	4.51	4.52
2nd side-side	0.80	0.77	0.79
2nd fore-aft	0.82	0.77	0.80

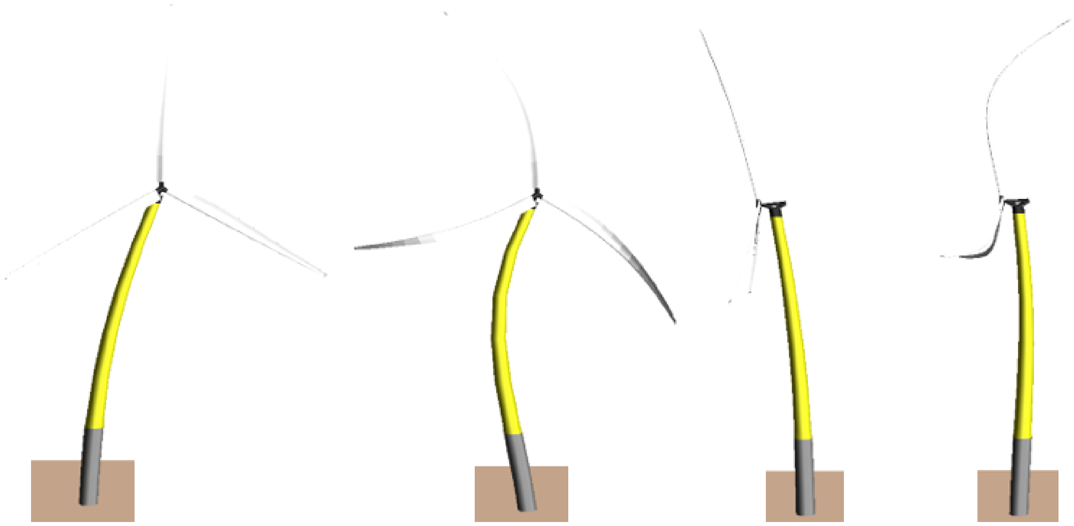
(a) 1st side-side mode. **(b)** 2nd side-side mode. **(c)** 1st fore-aft. **(d)** 2nd fore-aft.

Figure 6.7: 1st eigenmode of the OWT model. Scaled by 20 for visualisation purposes.

For verification purposes, the natural frequencies are compared to the RWT from Bak et al. (2013). Table 6.3 displays the eigenfrequencies obtained from Bak et al. (2013) and the obtained eigenfrequencies for this thesis. As the table displays, there is good correspondence between the eigenvalues. The relatively large difference for the tower mode is due to the DTU model not including the monopile, while this thesis does.

Table 6.3: Eigenvalue properties with DTU 10MW RTW.

Mode	**Natural frequency [Hz] DTU**	**Natural frequency [Hz] USFOS**	**Deviation [%]**
1st Tower side-side	0.25	0.209	17.9
1st Tower fore-aft	0.25	0.207	18.8
1st asymmetric flap with yaw	0.55	0.554	0.7
1st asymmetric flap with tilt	0.59	0.579	1.9
1st collective flap mode	0.63	0.679	7.5
1st asymmetric edge1	0.92	1.005	8.8
1st asymmetric edge 2	0.94	1.015	7.7
2nd Tower side-side	Not stated	1.248	-
2nd Tower fore-aft	Note stated	1.216	-

Chapter 7

Global analysis results from USFOS

This chapter presents the results of interest from the global analysis performed in USFOS. The procedure of the global analysis for this work has been to evaluate the global response of the OWT beam model before investigating the local effects using a shell model. Based on the results, the monopile is little affected by the collision loads, and thus, the focus is directed to the tower.

The global responses are kinetic energy, acceleration and displacement of tower top, critical area moments and the force at the nonlinear spring. As previously discussed, the shell model location is based on critical areas and was implemented with imperfections. The local effects of importance are buckling.

The interest results are presented separately for the parked and operating condition, and a comparison between the two is subsequently discussed. Concurrently, the results are discussed as they are presented. The parked and operating condition are subjected to impact velocities of 2m/s and 3m/s. It is essential to specify that the ship impact is applied at a time equal to 60s. This is to ensure the operating condition is fully initiated before the impact is applied.

7.1 Impact energy and force-deformation curves

Common for the parked and operating condition are the kinetic energy and force-deformation curves. A comparison between the output results from LS-DYNA and USFOS is made to validate an accurate representation of the ship impact model.

Previous discussions revealed that the design initial impact energies were 21MJ for an impact velocity of 2m/s and 47MJ for an impact velocity of 3m/s. Figure 7.1 shows kinetic energy obtained from USFOS for both impact velocities. As can be seen, there is good correspondence both with the initial impact energies and the kinetic energy obtained from USFOS. There is no kinetic energy before the impact, and after the impact, the kinetic energy will oscillate around 10MJ and 20MJ, for impact velocity 2m/s and 3m/s, respectively. The reduction of kinetic energy is due to collision energy being transformed into strain energy when the structures deform. The remaining kinetic energy is due to the OWT moving back and forth after the impact. The RNA and blades will induce this motion further as they have a large weight and obtain large velocities.

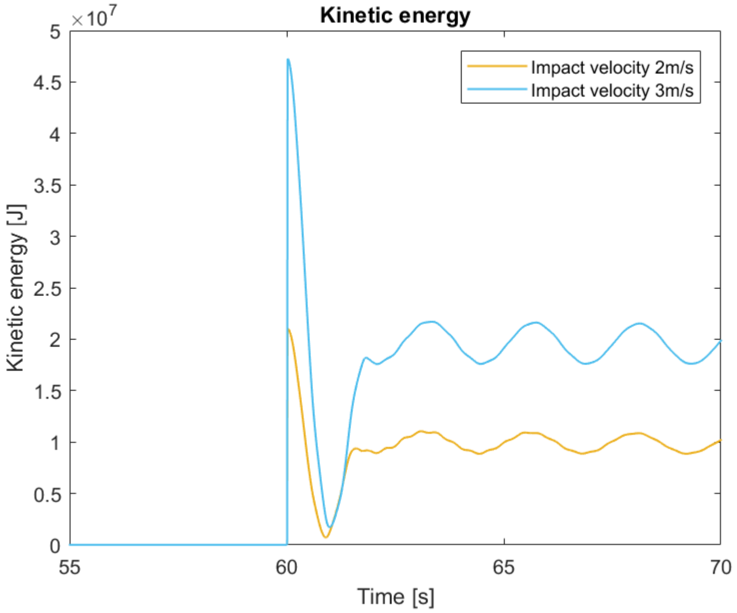

Figure 7.1: Kinetic energy obtained from USFOS for impact velocities of 2m/s and 3m/s.

Comparing the LS-DYNA kinetic energies, as displayed in Figure 5.12, with the USFOS kinetic energies, it can be seen that the LS-DYNA energies oscillate at a lower magnitude. For an impact velocity of 2m/s, it oscillates at 4MJ, and for an impact velocity of 3m/s, it oscillates at 7MJ. This is due to more collision energy being transformed into strain energy as LS-DYNA models the ship and OWT more accurately. Additionally, LS-DYNA conducts more accurate calculations as the ship, and OWT is modelled using shell elements.

The force-deformation curve is validated by comparing the force-deformation curve obtained from LS-DYNA based on the interpolated curve used as input in USFOS. This is represented in Figure 7.2 for an impact velocity of 2m/s and in Figure 7.3 for an impact velocity of 3m/s. Both figures show that the two curves coincide well. A distinct difference is that the USFOS output curve includes an offloading effect, represented by the straight line after reaching maximum, modelled by the linear spring. For an impact velocity of 2m/s, the deformation is 0.58m before offloading, and for an impact velocity of 3m/s, the deformation is 1.2m before offloading.

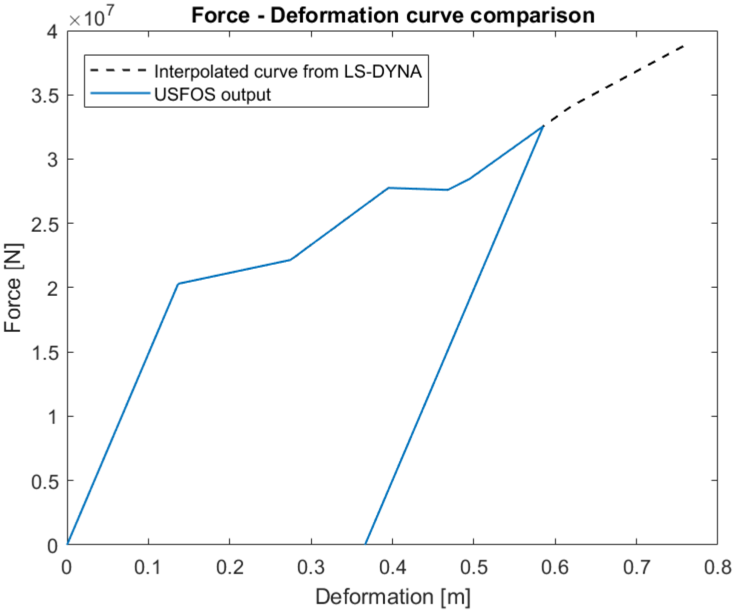

Figure 7.2: Force-deformation curve comparison of interpolated values from LS-DYNA and USFOS output for broadside impact. Impact velocity equal to 2m/s.

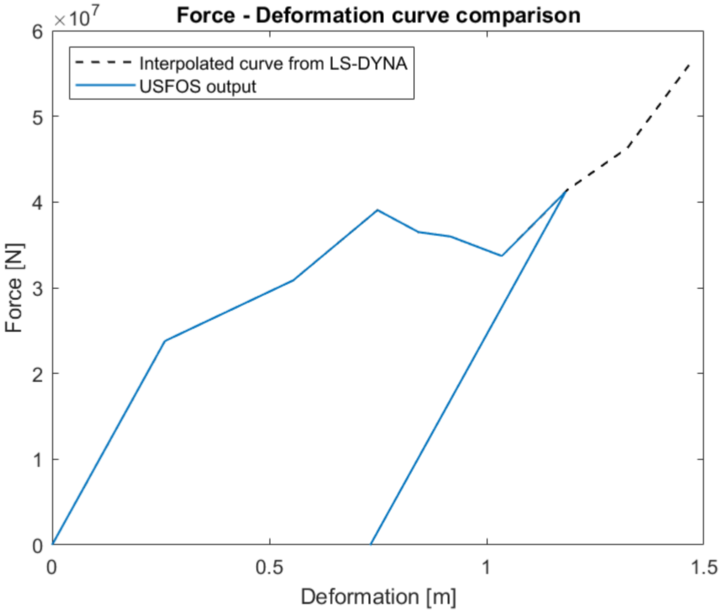

Figure 7.3: Force-deformation curve comparison of interpolated values from LS-DYNA and USFOS output for broadside impact. Impact velocity equal to 3m/s.

Additionally, the USFOS output curves estimate how much dissipated energy is obtained in the ship after deformation. By integrating the force-deformation curve, an impact velocity of 2m/s gave dissipated energy of 9MJ, while for an impact velocity of 3m/s, the dissipated energy is 25MJ. Thus, the remaining energy must be dissipated by the OWT or remain as kinetic energy. This fits well with the earlier discussion on kinetic energy.

7.2 Analysis of ship collision with OWT in parked condition

This section presents the results for the parked OWT subjected to a broadside ship impact. The results of interest are the tower top acceleration and displacement, the moment forces at the critical area and force at the nonlinear spring. Both impact velocities will be presented in the same figure for comparison and to evaluate the differences. All cases have the impact applied at a time equal to 60s.

7.2.1 Tower top acceleration

The tower top acceleration is of interest as the ship collision may lead to large accelerations at this location. This represents a risk to the electrical equipment of the OWT, in particular, the generator, as it is sensitive to high accelerations (Bela et al., 2017). Thus, the accelerations should be investigated even though the OWT structure can withstand the collision to ensure no significant damage occurs to the electrical equipment.

Figure 7.4 shows the acceleration of the tower top for the two impact velocities where (a) shows the acceleration in the time domain while (b) is in the frequency domain.

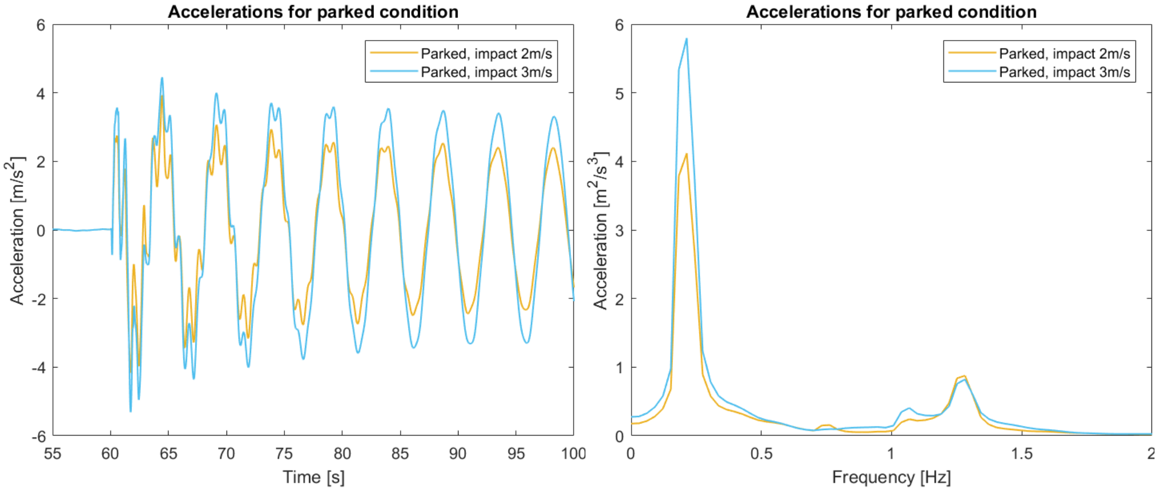

(a) Time domain. **(b)** Frequency domain.

Figure 7.4: Accelerations at tower top in parked condition for impact velocities of 2m/s and 3m/s.

As expected, the highest impact velocity generates the largest accelerations, as can be seen in Figure 5.13(a). The accelerations further follow the same pattern and oscillate due to the tower moving back and forth after impact. The largest peak occurs for the first oscillation period. The largest acceleration is 4.2m/s^2 and 5.3m/s^2 for impact velocity of 2m/s and 3m/s, respectively, in the time domain. This corresponds to 0.43g and 0.54g, where g is the gravitational acceleration.

From the eigenvalue analysis, it is known that the eigenfrequencies are 0.2Hz and 1.2Hz for the tower's first and second mode. Accordingly, the peaks are shown in Figure 7.4(b) concur with these modes and will excite the structure.

Little literature is found to verify the maximum allowable acceleration of the tower top of an OWT. The manufacturer of the OWT may provide this information as stated in Liu et al. (2015) where SIEMENS provided the maximum allowable acceleration of the nacelle of the OWT in question. Nejada et al. (2019) states that a common practice in the industry is to determine an operational limit for the tower top maximum axial acceleration to a range of 0.2g-0.3g, but this is not explicitly specified in design codes.

Nejada et al. (2016) investigated a 5MW monopile OWT that obtained 0.1g for high wind speeds near cut-out with only environmental loads, i.e. no ship collision was investigated. The work indicates that the maximum axial acceleration of the tower top is primarily a function of the tower motion. By comparing the above results with Solvik (2020), a good correlation between the maximum top acceleration where the acceleration is approximately $4m/s^2$ for an impact velocity of 3m/s was found. However, based on the maximum axial acceleration in the range of 0.2-0.3g, the most significant accelerations are roughly twice as large as this range and thus, exceed the operational limit.

7.2.2 Tower top displacement

The tower top displacement is of interest as large displacements can alter the effect of the acting forces as they may be distributed differently. Since this thesis' axial forces are relatively small, the forces that may be altered are the bending moments.

The tower top displacement can be seen in Figure 7.5 where (a) shows the displacement in the time domain and (b) illustrates the frequency domain. As expected, the displacement of the tower top increases with increased impact velocity. The most significant displacement is 1.6m and 2.3m for impact velocities of 2m/s and 3m/s, respectively.

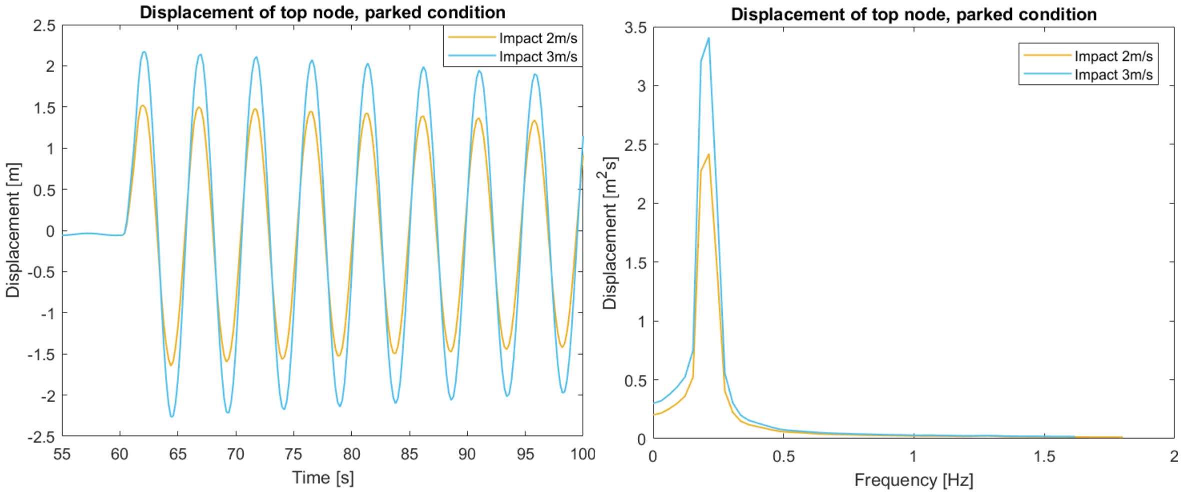

(a) Time domain.

(b) Frequency domain.

Figure 7.5: Displacement of tower top in parked condition for impact velocities of 2m/s and 3m/s.

Figure 7.5(b) shows that only the first eigenmode excites the displacement. The second mode should, in theory, contribute slightly to the displacement of the tower top. However, since the node for the second bending mode is below the tower top, this displacement is small and does not affect the result in this case.

7.2.3 Moment force in the midsection of the tower

The moment force at the critical area is investigated. For this thesis, the critical area was found to be at the midsection of the tower, and the moment force can be seen in Figure 7.6 where (a) represents the time domain and (b) represent the frequency domain. The most significant moment forces are 263MNm and 348MNm for impact velocities of 2m/s and 3m/s, respectively.

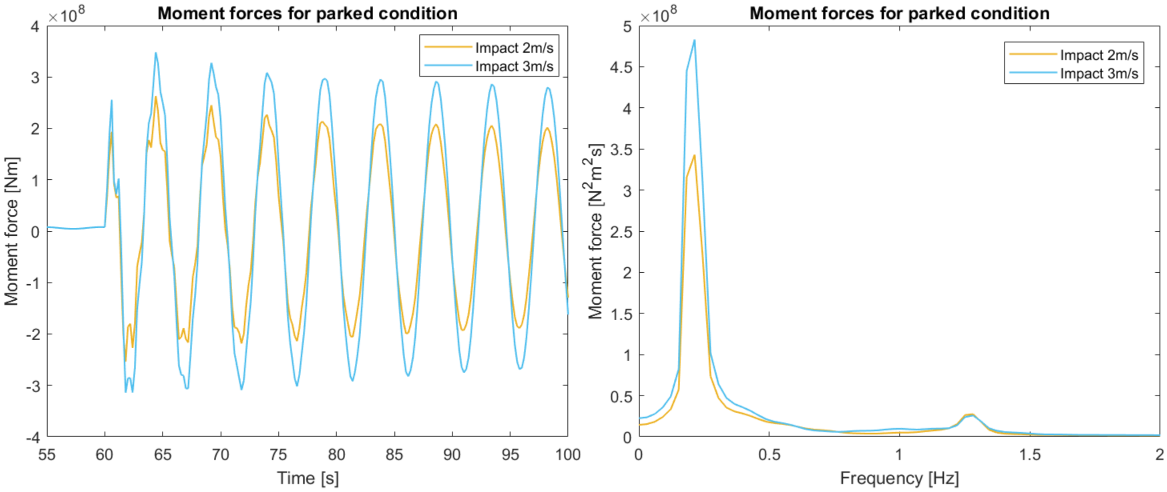

(a) Time domain.

(b) Frequency domain.

Figure 7.6: Moment forces in the middle of the tower for parked condition for impact velocities 2m/s and 3m/s.

As illustrated in (a), the moment force at the midsection follows the same pattern for both impact velocities. (b) shows how the first and second eigenmode excites the moment force.

7.2.4 Force at nonlinear spring

Figure 7.7 shows the impact force, i.e. the force at the nonlinear spring. The most significant impact force is 32MN and 41MN for impact velocities 2m/s and 3m/s, respectively.

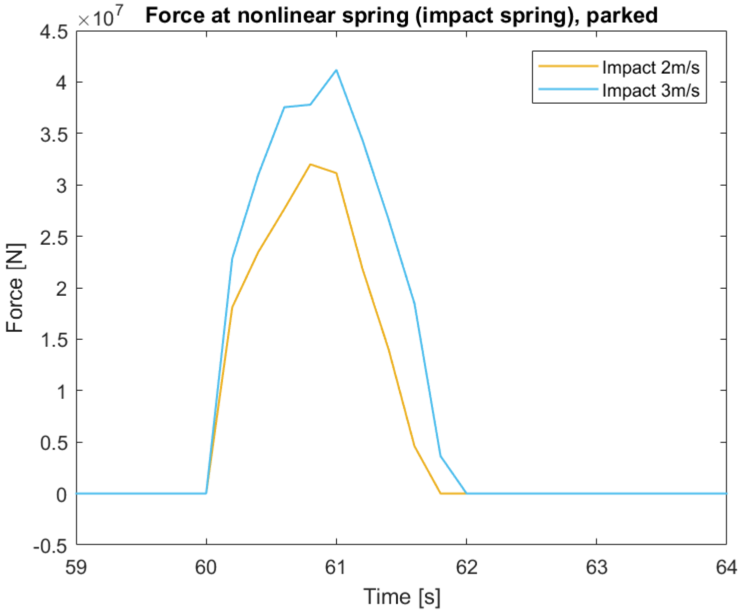

Figure 7.7: Force at nonlinear spring for parked condition for impact velocities of 2m/s and 3m/s.

The force-time curve is used to investigate the impulse, which can be obtained by finding the area under the curves. By integrating the yellow line, representing the impact velocity of 2m/s, it was found that the impulse is equal to 34.7MNs. Integration of the blue curve, representing the impact velocity 3m/s, gave an impulse equal to 50.7MNs. Impulse is further discussed in Section 7.4 when comparing the parked and operating conditions.

7.3 Analysis of ship collision with OWT in operating condition

Likewise, the two impact velocities are presented in the same figures for easy comparison for the operating condition. The responses for the operating condition are similar to those of parked conditions. In addition, to the above results, the blade tip clearance is investigated to conclude if the blades will hit the tower or not.

7.3.1 Tower top acceleration

An illustration of the tower top acceleration in operating condition when subjected to a ship impact is seen in Figure 7.8 where (a) represents the time domain and (b) represents the frequency domain. The largest accelerations are $3.8 m/s^2$, or 0.39g, and $4.3 m/s^2$, or 0.44g, for impact velocities of 2m/s and 3m/s, respectively. Again, the accelerations are above the maximum axial acceleration range, as discussed earlier.

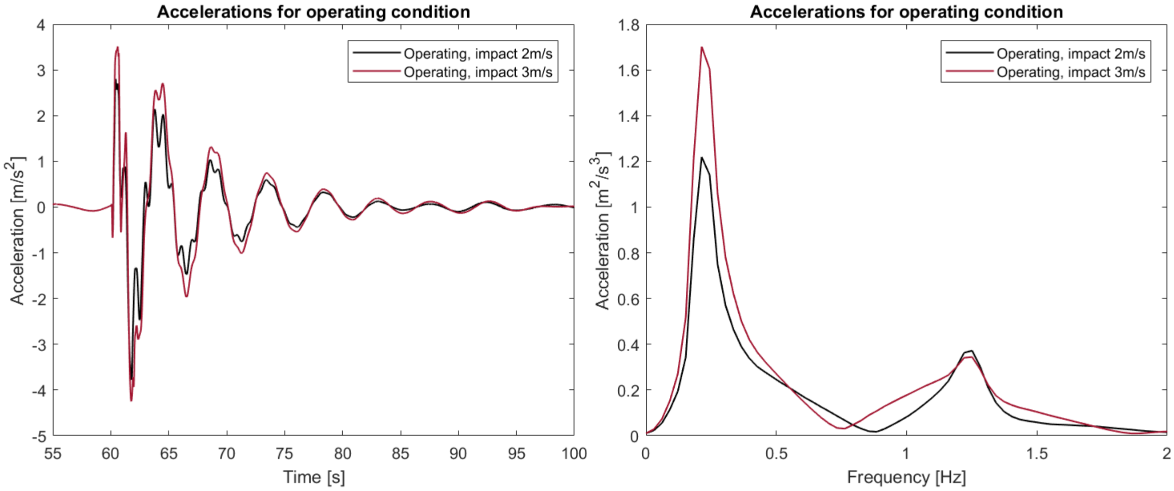

(a) Time domain.

(b) Frequency domain.

Figure 7.8: Comparison of accelerations at tower top in operating condition for impact velocities of 2m/s and 3m/s.

The accelerations for the two impact velocities follow the same oscillatory pattern. The largest impact velocity obtains the most significant accelerations, which is similar to that of the parked condition. Note the decay of the oscillations. This is due to the aerodynamic damping implemented in the control algorithm for the OWT. This effect can be seen in the following results as well.

Figure 7.8(b) shows how the first and second eigenmodes excite the structure and influences the accelerations.

7.3.2 Tower top displacement

Figure 7.9 depicts the displacement of the top node for the operating condition in the time domain and the frequency domain. The largest displacements are 2.3m and 2.9m for impact velocities of 2m/s and 3m/s, respectively.

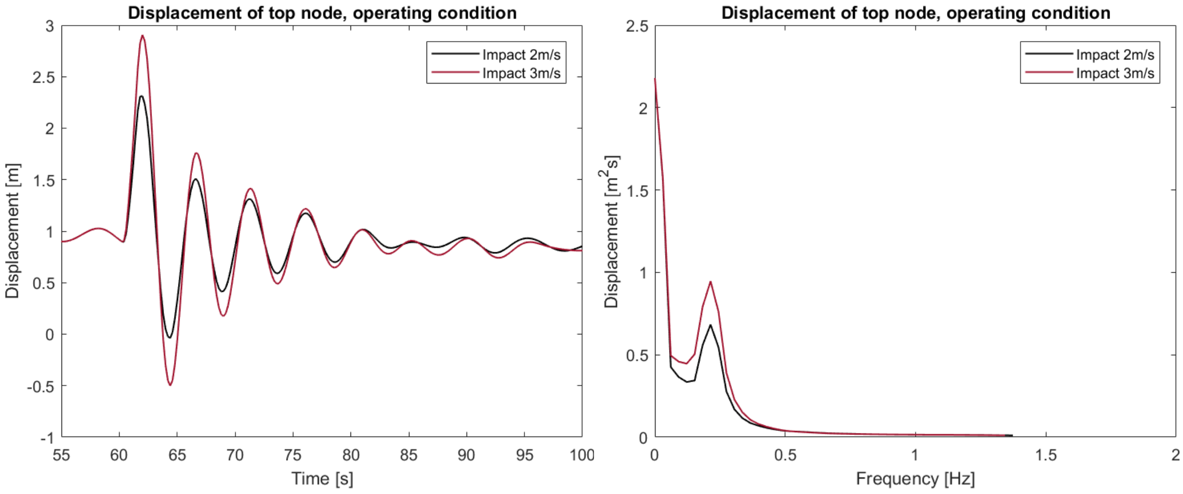

(a) Time domain. **(b)** Frequency domain.

Figure 7.9: Comparison of displacement of tower top in operating condition for impact velocities of 2m/s and 3m/s.

Again, the curves follow the same oscillating pattern in the time domain. The largest impact velocity gives the most significant tower top displacement, which is similar to that of the parked condition. One major difference is the initial displacement of 0.99m due to the wind- and rotational loads. This results in an upwards shift of the displacement curve. Likewise, the aerodynamic damping included in the controller algorithm can be seen as the displacement oscillations decrease over time.

Likewise, for the parked condition, the displacement of the tower top for the operating condition does not show excitation from the second eigenmode. A distinct difference is that the frequency domain starts at a displacement of 2.2m. This is due to the response spectrum, and the start value represents the constant for this spectrum.

7.3.3 Moment force in the midsection of the tower

Moment forces for the critical area, which is the midsection, is shown in Figure 7.10 where (a) illustrates the time domain and (b) illustrates the frequency domain. The most significant moments are 377MNm and 424MNm for impact velocities of 2m/s and 3m/s, respectively.

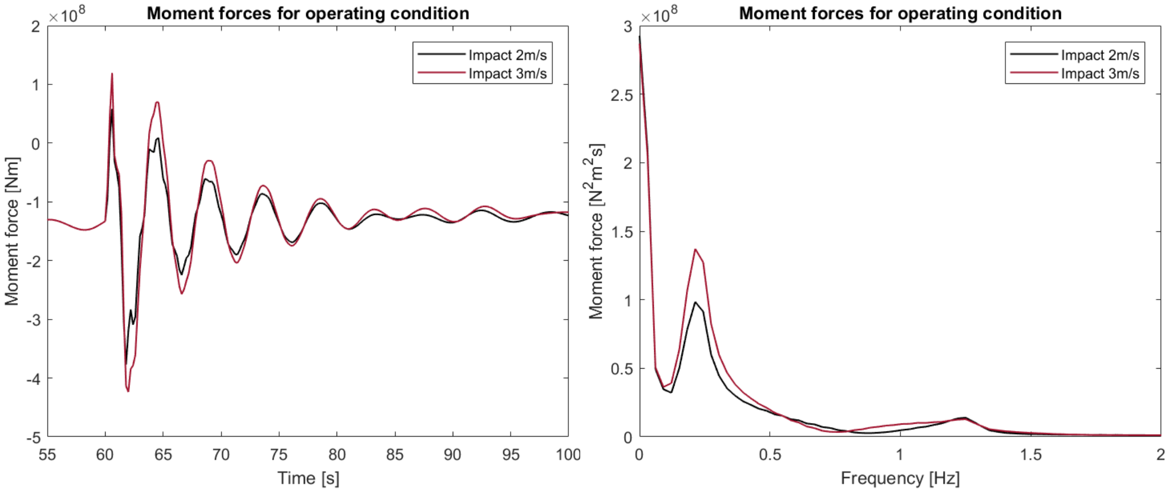

(a) Time domain. **(b)** Frequency domain.

Figure 7.10: Moment forces in the middle of the tower for operating condition for impact velocities 2m/s and 3m/s.

The response is similar to that of the parked condition, but there is one major difference compared to the parked condition. That is the initial moment force of 135MNm due to the wind- and rotational loads. This results in a downward shift of the moment force curve, which can be seen in the figure above. The response of the moment forces in the time domain follows the same oscillatory pattern, and the most significant moments are obtained from the largest impact velocity. The aerodynamic damping is again gradually reducing the moment force.

The moment force is excited from both eigenmodes of the structure, which can be seen in Figure 7.10(b). Similar to the displacement, moment forces in the frequency domain starts at 287MNm, which is due to the constant in the response spectrum.

7.3.4 Force at nonlinear spring

Figure 7.7 shows the impact force, i.e. the force at the nonlinear spring. The most significant impact force is 32MN and 41MN for impact velocities 2m/s and 3m/s, respectively.

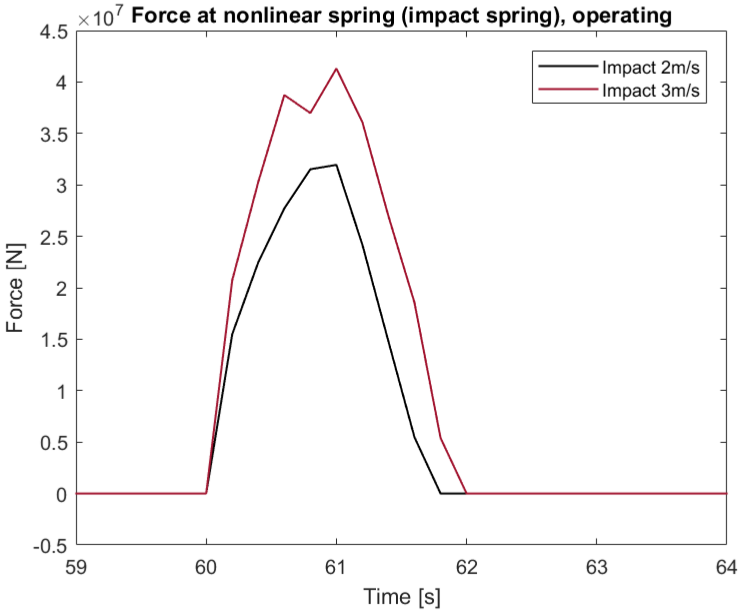

Figure 7.11: Comparison of force at nonlinear spring for operating condition for impact velocities 2m/s and 3m/s.

The impulse for the black curve, representing the impact velocity of 2m/s, is 34.7MNs, while for the red curve, representing the impact velocity of 3m/s, it is 51.0MNs.

7.3.5 Clearance between blade tip and tower

Due to the high flexibility of the blades, making the blades able to experience large deformations, it is of interest to investigate the blade tip clearance between blades and tower. Figure 7.12(a) shows the full blade tip clearance in operating condition for the two impact velocities, while (b) shows a close up of the blade tip clearance. The local minimums represent the blade at the bottom of its rotations. At this point, the blade may hit the tower structure if the deformations of the blades are too large during impact.

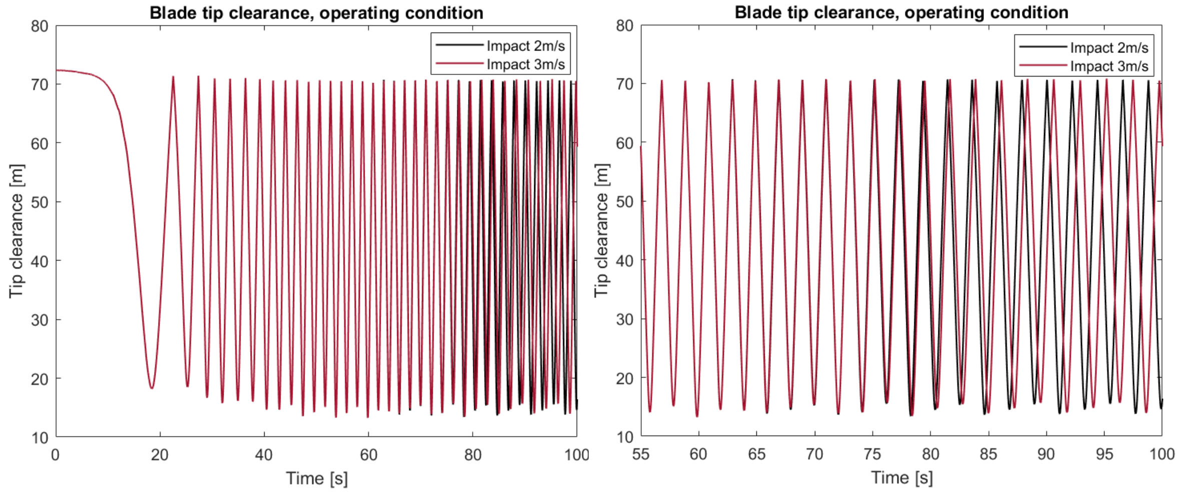

(a) Full blade tip clearance.

(b) Close up of blade tip clearance.

Figure 7.12: Blade tip clearance for operating condition for impact velocities of 2m/s and 3m/s.

The average distance between blade and tower at the bottom location was found to be 14.6m and 14.7m for impact velocities of 2m/s and 3m/s, respectively. The minimum distance between blade tip and tower was found to be 13.3m for both velocities. However, this was found at a time equal to 59.9s, i.e., before the impact took place. This is due to the blade not being directly in front of the tower when the impact occurs. Therefore, this is investigated further by timing the impact of one blade directly in front of the tower. The ship impact is now applied at a time equal to 48s. Figure 7.13 shows the new blade clearance when the ship impact is applied at a time equal to 48s.

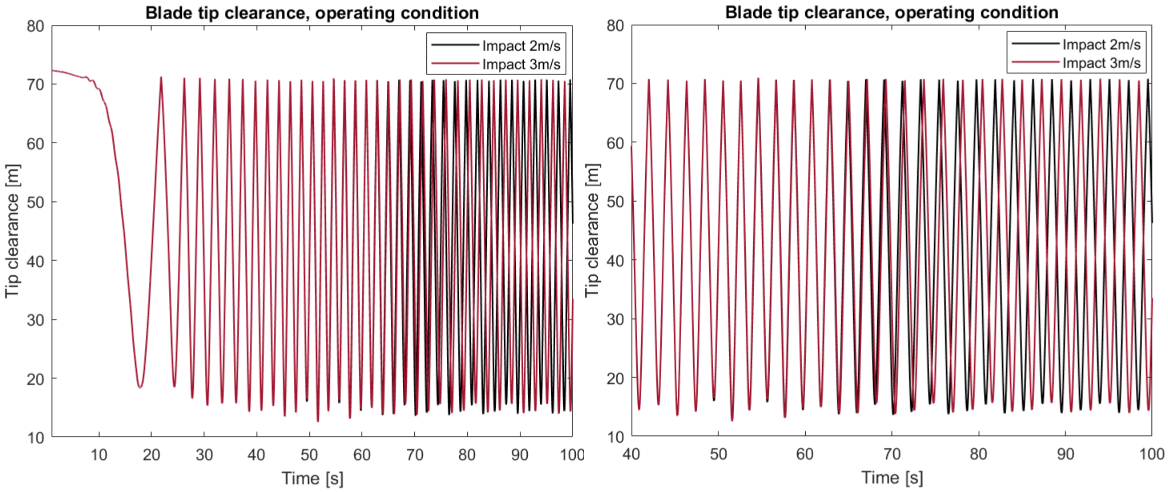

(a) Full blade tip clearance. **(b)** Close up of blade tip clearance.

Figure 7.13: Blade tip clearance for operating condition for timed impact velocities of 2m/s and 3m/s.

The average distance between blade and tower at the bottom location is 14.8 and 14.9m for impact velocities of 2m/s and 3m/s, respectively. The minimum distance between blade tip and tower is 12.7m for an impact velocity of 2m/s and 12.6m for an impact velocity of 3m/s. Hence, the minimum distance between blade tip and tower has been reduced by roughly 1.3m. A discussion regarding this will be performed in Chapter 10.

7.4 Comparison of impact response between parked and operating condition

This section uses the results presented above to compare the parked and operating condition of the OWT. The aim is to identify if the inertia effects from the blades and wind energy will influence the response negatively or positively with respect to potential failures. Each topic is presented separately with its related discussion. As a reminder, the ship impact is applied at a time equal to 60s.

7.4.1 Tower top acceleration

The comparison between the tower top acceleration of parked and operating condition for both impact velocities can be seen in Figure 7.14.

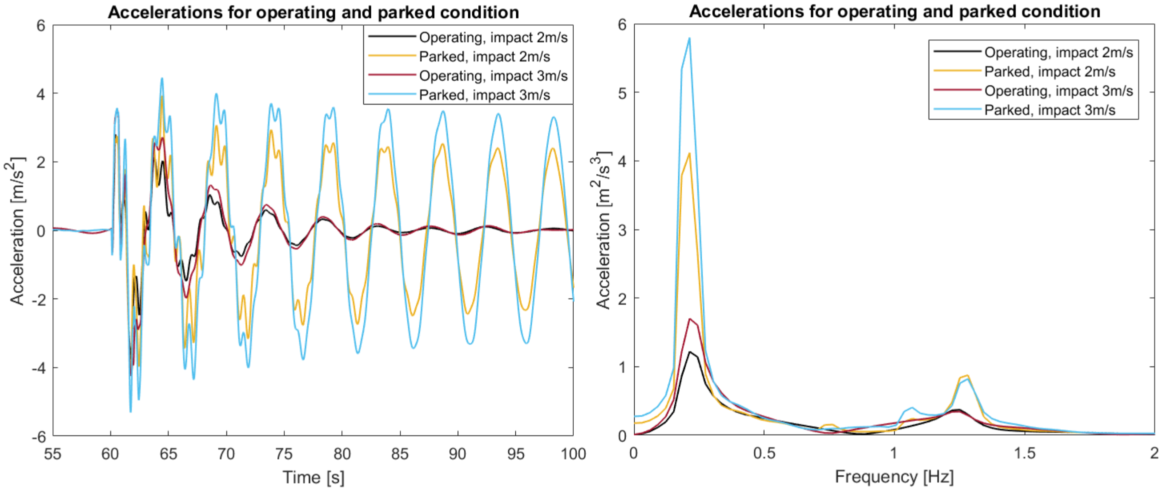

(a) Time domain.

(b) Frequency domain.

Figure 7.14: Comparison of accelerations at tower top in operating condition for impact velocities of 2m/s and 3m/s.

As can be seen from the figure, the accelerations are approximately the same for the first oscillation period before the aerodynamic damping from the controller reduces the acceleration for the operating condition for both impact velocities. Table 7.1 summarises the largest tower top accelerations.

Table 7.1: Comparison of tower top accelerations for parked and operating condition for impact velocities of 2m/s and 3m/s.

Condition	**2m/s**	**3m/s**
Parked	0.43g	0.54g
Operating	0.39g	0.44g

7.4.2 Tower top displacement

Figure 7.15 represents the comparison of the tower top displacement for the parked and operating condition for both impact velocities.

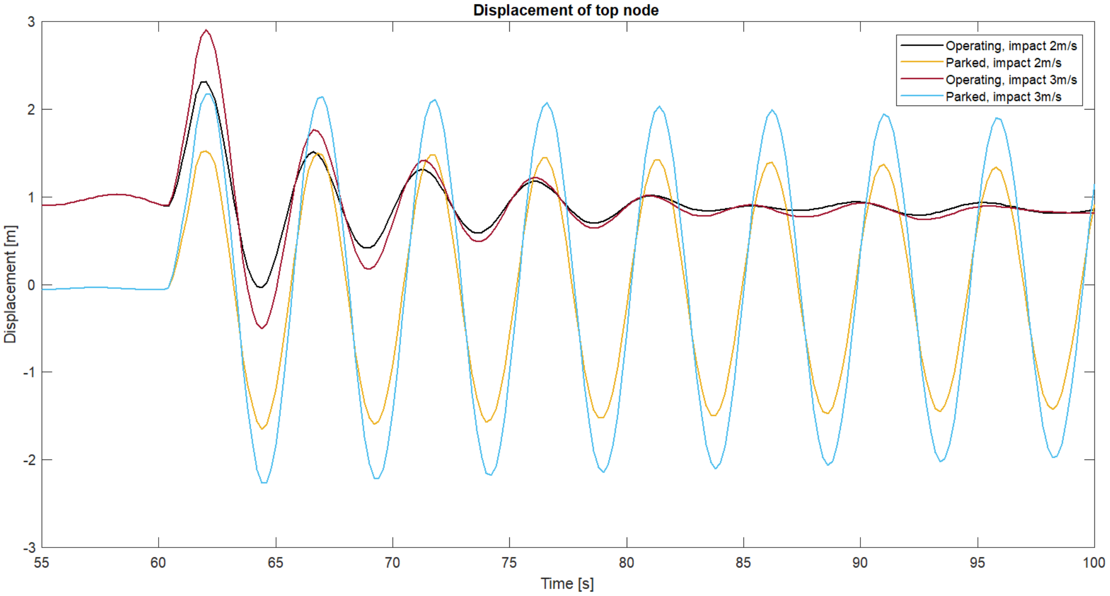

(a) Time domain.

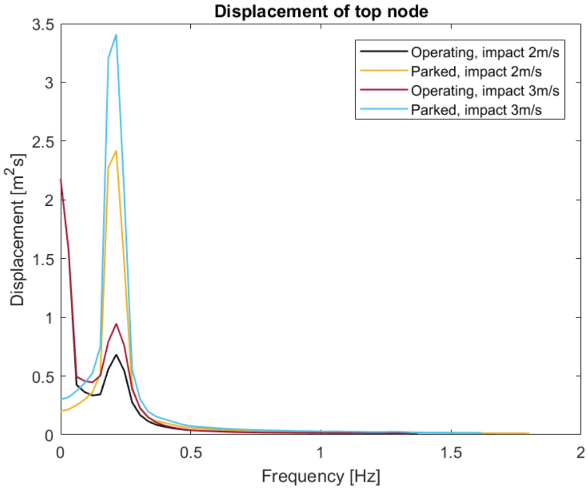

(b) Frequency domain.

Figure 7.15: Comparison of displacement of tower top in operating condition for impact velocities of 2m/s and 3m/s.

Due to the upwards shift for the operating conditions, the most significant displacement of the tower top will occur at an earlier stage than that of the parked condition. For operating condition, the largest displacements occur at 62s, while for parked conditions, it occurs at 64s. Table 7.2 summarises the largest tower top displacements.

Table 7.2: Comparison of tower top displacement for parked and operating condition for impact velocities of 2m/s and 3m/s.

Condition	**2m/s**	**3m/s**
Parked	1.6m	2.3m
Operating	2.3m	2.9m

7.4.3 Moment force in the midsection of the tower

The moment forces in the midsection of the tower for the parked and operating condition for both impact velocities are shown in Figure 7.16.

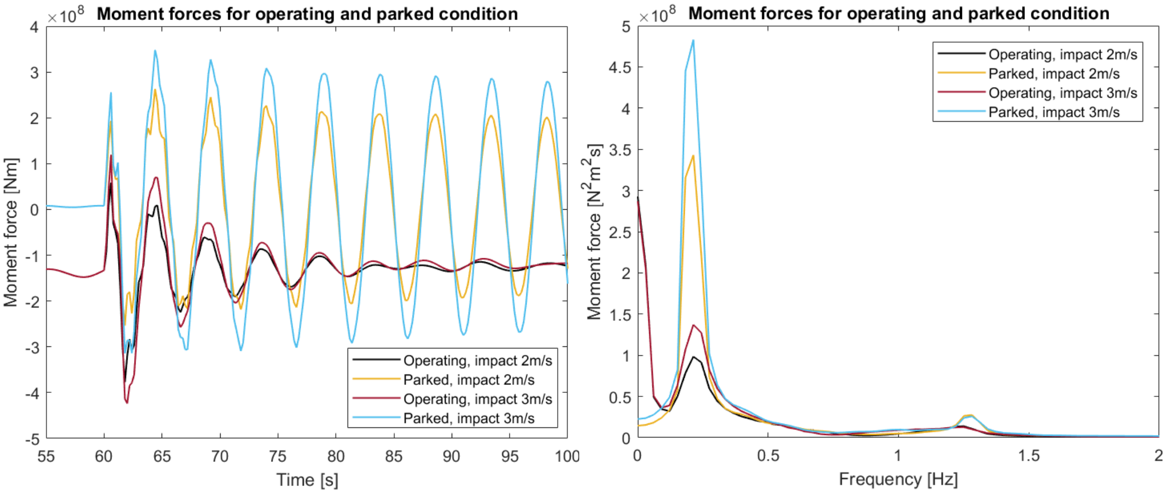

(a) Time domain.

(b) Frequency domain.

Figure 7.16: Comparison of moment forces in the middle of the tower for parked and operating condition for impact velocities of 2m/s and 3m/s.

Due to the moment's downward shift, the most significant moment force of the midsection occurs at different times for the parked and operating condition. For the operating condition, the most significant moment force occurs at 61.8s, while for the parked condition, it appears at 64.4s. Table 7.3 summarises the most significant moment forces for the midsection of the tower.

Table 7.3: Comparison of midsection moment force for parked and operating condition for the impact velocities of 2m/s and 3m/s.

Condition	**2m/s**	**3m/s**
Parked	263MNm	348MNm
Operating	377MNm	424MNm

Since moment forces may lead to a critical collapse mechanism, which is the tower falling towards the ship, it is of interest to investigate when the most significant moment force occurs. It is desirable that this is when the OWT moves away from the ship, i.e. the OWT motion is away from the ship, to avoid impact. The most significant moment forces mentioned above corresponds to an OWT motion away from the ship for the operating condition but towards the ship for the parked condition. This means that a potential collapse mechanism can happen at a critical point for the parked condition. However, as seen from Figure 7.17 and Figure 7.18, low plastic utilisation is seen at these times and likewise before the highest moment forces occur. Hence, it is improbable that the collapse mechanism will happen. This will be further investigated in Chapter 8 when a local analysis is conducted. The highest plastic utilisation is for an impact velocity of 3m/s at time 64.2s.

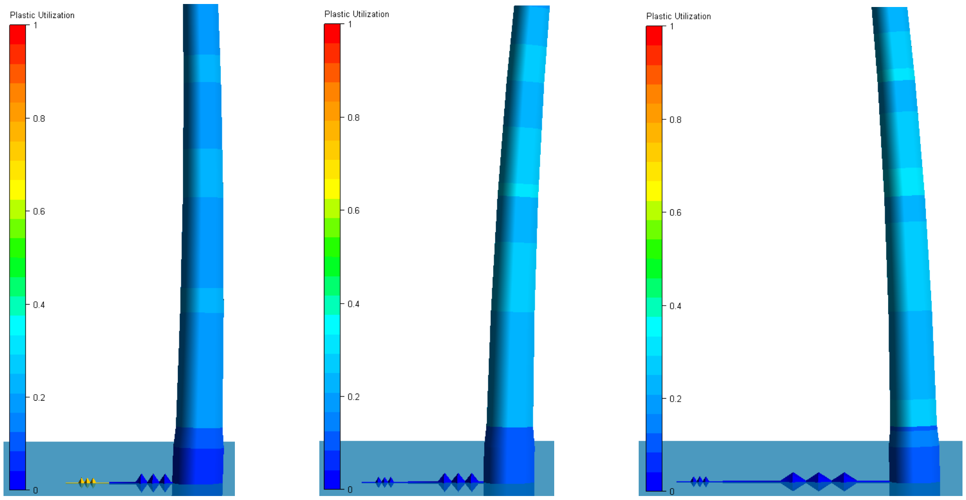

(a) Time = 60.6s **(b)** Time = 61.8s **(c)** Time = 64.4s

Figure 7.17: Plastic utilisation in parked condition at impact velocity 2m/s. Fringe range from 0 (dark blue) to 1 (red). Scaled up for visualisation.

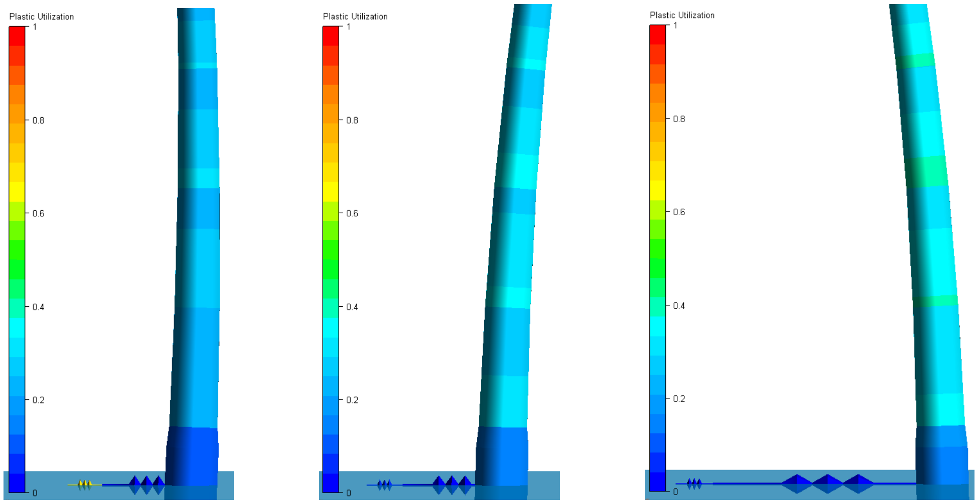

(a) Time = 60.6s **(b)** Time = 61.8s **(c)** Time = 64.4s

Figure 7.18: Plastic utilisation in parked condition at impact velocity 3m/s. Fringe range from 0 (dark blue) to 1 (red). Scaled up for visualisation.

7.4.4 Force at nonlinear spring

The forces at the linear spring are shown in Figure 7.19. It is expected that the forces for the parked and operating condition are similar due to the impact velocity. The below figure confirms this.

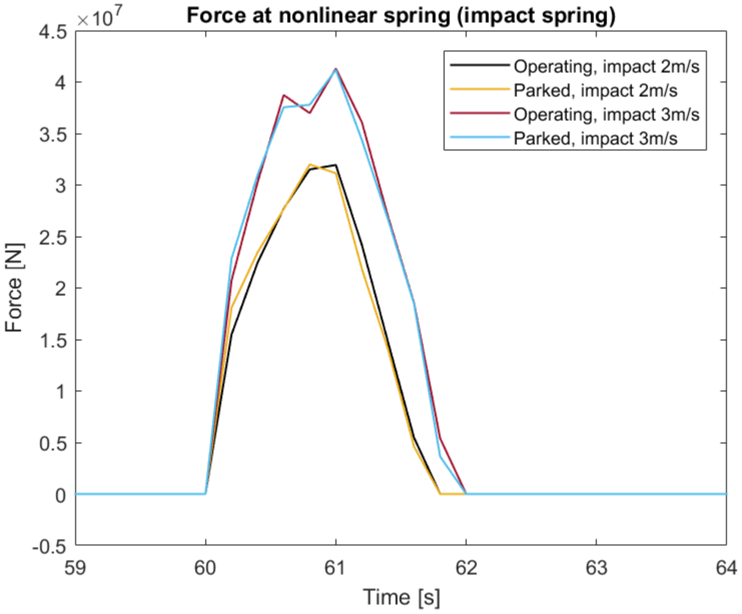

Figure 7.19: Force at nonlinear spring for both parked and operating condition for impact velocities 2m/s and 3m/s.

The largest impact forces for the nonlinear spring is summarised in Table 7.4. Table 7.5 summarises the impulses for each graph.

Table 7.4: Comparison of nonlinear spring force for parked and operating condition for the impact velocities 2m/s and 3m/s.

Condition	**2m/s**	**3m/s**
Parked	32MN	41MN
Operating	32MN	41MN

Table 7.5: Comparison of impulses for parked and operating condition for the impact velocities of 2m/s and 3m/s.

Condition	**2m/s**	**3m/s**
Parked	34.7MNs	50.7MNs
Operating	34.7MNs	51.0MNs

The impulses (momentum) describe the changes in the ships velocity and the movement of the OWT. There are two impact periods: 1) up to equal velocity at the contact point and 2) recovery of elastic strain energy. The ship has a velocity of approximately 0.5m/s away from the OWT after impact in the present case. Thus, a significant recovery takes place, and parts of the strain energy are interchanging with kinetic energy in the OWT.

Chapter 8

Local buckling analysis of the OWT

The global analysis revealed that it would be of interest to investigate the local effects of the midsection of the tower. The local effects of interest are the buckling of the tower as the most significant moment forces in parked condition appeared when the OWT are moving towards the ship. Thus, this chapter presents the local analysis concerning buckling of the midsection of the tower.

8.1 Calculations of buckling capacity

To give an indication of the structural utilisation of the tower, some simple calculations are performed. These calculations are then compared to the global analysis results, and an evaluation of the results is made. In Chapter 3, Section 3.4 about buckling of cylindrical shells these considerations and equations are discussed. Hence, only the results from Equation 3.5 to Equation 3.10 are presented.

The main dimensions of the midsection, bottom of tower and seabed is presented in Table 8.1. All three areas are evaluated here to confirm that the midsection is the critical area of the OWT.

Table 8.1: Main dimensions for midsection of tower, bottom of tower and at seabed.

Parameter	**Midsection of tower**	**Bottom of tower**	**Seabed**
Radius, r [m]	3.45	4.15	4.50
Thickness, t [mm]	35.9	46.0	80.0
Elastic modulus, E [GPa]	210	210	210
Yield stress, σ_Y [MPa]	355	355	355

By using Equation 3.5 to Equation 3.10 the elastic critical buckling stress, with consideration to imperfections and plasticity, is found. The results for each equation is found in Table 8.2.

Table 8.2: Calculations of buckling capacity

Parameter	**Midsection of tower**	**Bottom of tower**	**Seabed**
Elastic buckling resistance, σ_{cl} [MPa]	1322.8	1408.3	2258.7
Knock-down factor, ρ_{kd} [-]	0.435	0.438	0.459
Elastic buckling resistance w. imperfections, σ_E [MPa]	575.6	617.4	1036.4
Reduced slenderness ratio, $\bar{\lambda}$ [-]	0.79	0.76	0.59
Plasticity reduction factor, ϕ [-]	0.85	0.87	0.95
Elastic critical buckling stress incl. imperfections and plasticity, σ_{cr} [MPa]	302.2	307.8	335.8

As the above table displays, the lowest elastic buckling resistance is found at the midsection of the tower. Previously, it was mentioned that the seabed displayed high stresses, as seen in Appendix G. However, as Table 8.2 shows, the critical buckling stress is higher at the seabed. Previous work has indicated that the bottom of the tower may also be a critical area. However, based on the stresses displayed in Appendix G and the above table, this can not be concluded here. Herein, the focus is on the midsection based on the above discussion.

8.2 Buckling response of OWT during ship collision

To evaluate the elastic critical buckling stress, the bending stress in the tower's midsection is obtained from the global analysis. The bending stresses are the highest obtained values for the midsection for each condition and impact velocity. Even though it was found that the parked condition with an impact velocity of 2m/s had the least favourable outcome, both conditions and impact velocities are presented to gain a complete overview.

The bending stress values are compared to the elastic critical buckling stress to indicate which scenario may cause buckling. The maximum obtained bending stresses are displayed in Table 8.3. As the table shows, no case exceeds the critical buckling stress. This indicates that buckling will not occur.

Table 8.3: Maximum obtained bending stress at midsection of tower when subjected to ship impact.

Condition	**Impact velocity = 2m/s**	**Impact velocity = 3m/s**
Parked	185 [MPa]	212 [MPa]
Operating	254 [MPa]	285 [MPa]

Since the OWT is moving towards the ship for the largest moments in parked condition, plastic utilisation is investigated for this case as it is a potential collapse mechanism. Firstly, the calculated imperfection of 16mm is investigated. Figure 8.1 display the highest plastic utilisation areas for impact velocities 2m/s and 3m/s in parked condition. The analysis shows a high plastic utilisation at both the impact side and the backside of the OWT during impact. The fringe range has been narrowed down to obtain the maximum value locations.

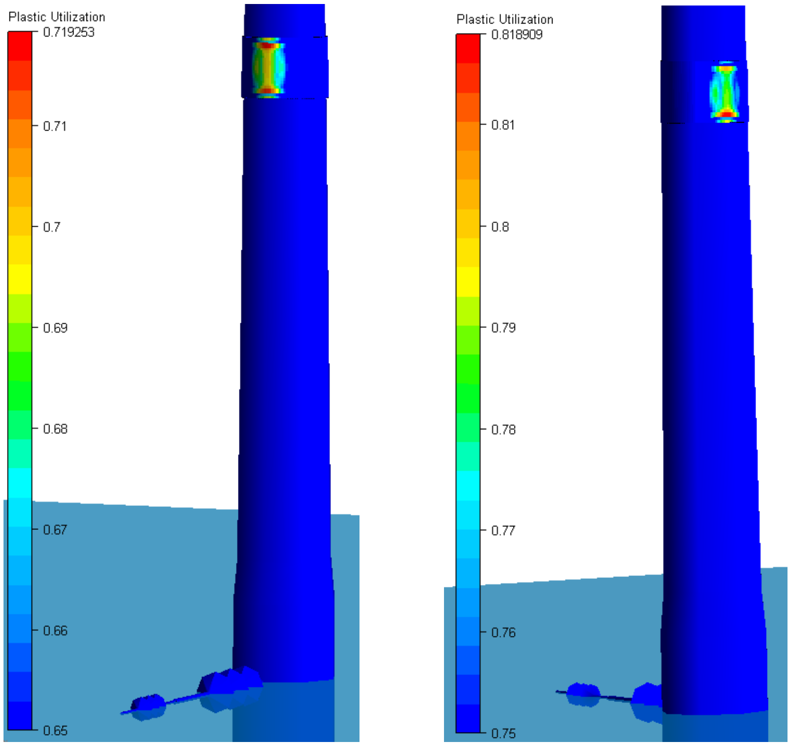

(a) Time = 64.8s. Fringe range from 0.650 (dark blue) to 0.719 (red).

(b) Time = 62.2s. Fringe range from 0.750 (dark blue) to 0.819 (red).

Figure 8.1: Highest plastic utilisation with imperfections equal to 16mm in parked condition at impact velocities 2m/s and 3m/s.

Overall it is observed high plastic utilisation at the impact and backside of the midsection during the first oscillations of the tower. However, the impact velocity of 2m/s is of concern due to the large plastic utilisation located at the ship impact side and the OWT moving towards to ship. Thus, the potential collapse mechanism of the tower falling on top of the ship may occur. Therefore, this is further investigated by reducing the tower thickness by 10% and increasing the imperfections to 40mm to initiate and trigger buckling. The increased imperfections will yield lower capacity while reducing the wall thickness is motivated by assuming an uncertainty in the load distribution and that the stresses are underestimated. The reduction in wall thickness may initiate buckling, implying that the structure is close to buckling at the current state.

The plastic utilisation of the section can be seen in Figure 8.2 for different cases. After conducting the analysis, the results showed no buckling of the midsection for reduced wall thickness and increased imperfections. Therefore, it is unlikely the OWT will collapse and hence, confirms the initial assumption made when evaluating the buckling capacity and bending stresses.

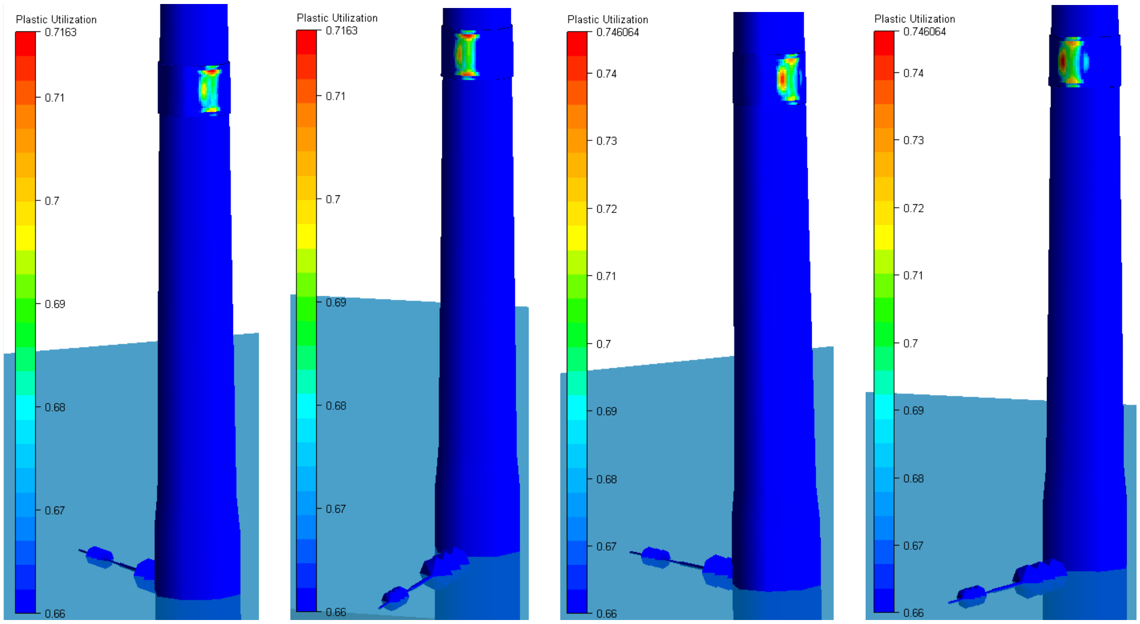

(a) Time = 62.0s and imperfection equal to 16mm. Fringe range from 0.660 (dark blue) to 0.716 (red).

(b) Time = 64.8s and imperfection equal to 16mm. Fringe range from 0.660 (dark blue) to 0.716 (red).

(c) Time = 62.0s and imperfection equal to 40mm. Fringe range from 0.660 (dark blue) to 0.746 (red).

(d) Time = 64.8s and imperfection equal to 40mm. Fringe range from 0.660 (dark blue) to 0.746 (red).

Figure 8.2: Highest plastic utilisation in parked condition with impact velocity of 2m/s for reduced thickness of the tower, and imperfections equal to 16mm and 40mm.

Chapter 9

Simple analytical model for ship collision with OWT

A simple analytical approach is used to estimate the OWT response when subjected to a ship impact. The response of the OWT is assumed as a linear summation between the deflections due to wind loads and the collision force separately. This means the interaction between the collision and wind loads can not be estimated. The following procedure for the analytical model is based on the works of Song et al. (2021).

The OWT is simplified to represent a cantilever beam, and the collision scenario can be approximated as a two-mass system. One mass represents the generalized mass of the OWT, m_t, and the other mass as the mass of the ship, including the added mass, m_a. This can be seen in Figure 9.1. L_1 is the total height of the monopile, while L_2 is the total height of the tower. F_w is the wind load, m_t is the generalized topside mass, u_t is the displacement of the topside, and F_t is the internal transmitted force, i.e. the generalized force. u_c is the displacement at the collision point, and F_c is the internal collision force. u_s is the displacement at the collision point of the ship, and k_s is the stiffness coefficient. t_1 and t_2 represents the duration of the first and second phase of the collision event, respectively.

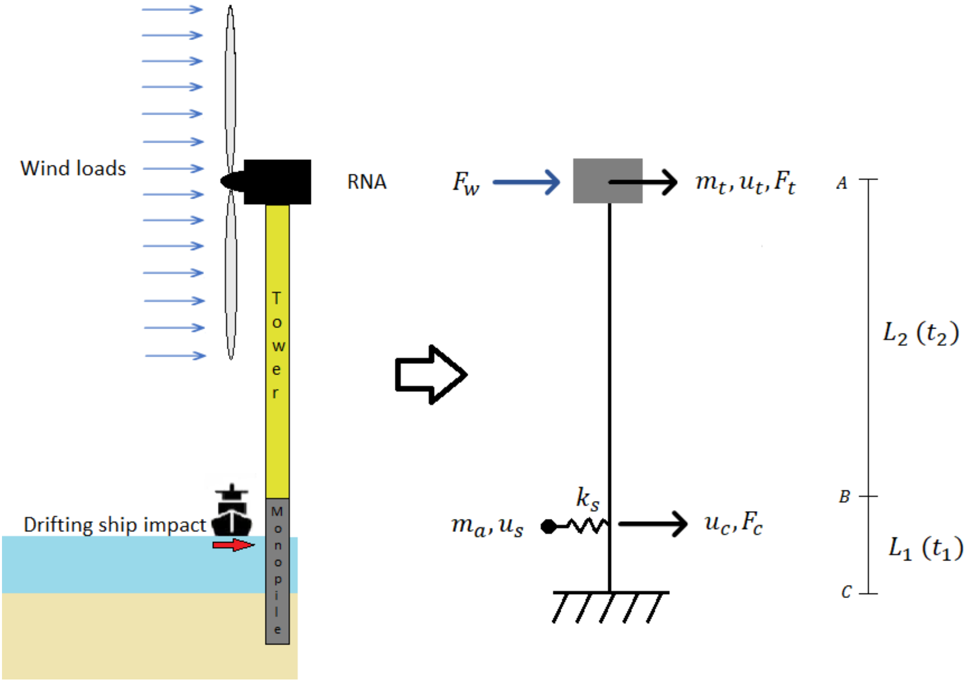

Figure 9.1: Simplified ship collision with OWT system for analytical model.

The deflection of the tower top under wind load is based on beam theory. The tower consists of a variable cross-section and is represented by section AB seen in Figure 9.2. The monopile has a constant cross-section and is represented by section BC. Due to the varying cross-section for the tower, the deflection needs to be calculated separately for the two sections.

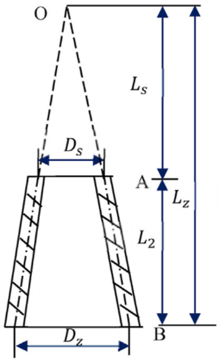

Figure 9.2: Schematic of the variable cross-section, AB.

For the variable cross-section, AB, the deflection of the tower top, A, is given as follows:

$$u_1 = \frac{F_w}{Ewtk^3}(A_1 + A_2) \tag{9.1}$$

$$A_1 = \frac{L_s}{L_z} - 1 + ln(L_z) \tag{9.2}$$

$$A_2 = \frac{L_s}{2}(\frac{2}{L_z} - \frac{1}{L_s} - \frac{L_s}{L_z^2}) \tag{9.3}$$

where E is the Young's modulus, $k = \frac{D_z - D_s}{L_2}$, D_z is the diameter of the tower base and D_s is the diameter of the tower top, L_s is the height of the tower, $L_s = \frac{D_s}{kL_z} = L_s + L_s$, t is average wall thickness and w is the coefficient of inertia moment which is equal to 0.393 for circular cross sections (Song et al., 2021).

For the constant cross-sectional area, BC, the force and bending moment acting on point B are given by:

$$F_B = F_w \tag{9.4}$$

$$M_B = F_w L_2 \tag{9.5}$$

Then, the deflection and rotation angle at point B can be calculated by the following formulas:

$$u_2 = \frac{F_B L_1^3}{3EI} = \frac{F_w L_1^3}{3EI} \tag{9.6}$$

$$\theta_2 = \frac{F_B L_1^2}{2EI} = \frac{F_w L_1^2}{2EI} \tag{9.7}$$

$$u_3 = \frac{M_B L_1^2}{2EI} = \frac{F_w L_2 L_1^2}{2EI} \tag{9.8}$$

$$\theta_3 = \frac{M_B L_1}{EI} = \frac{F_w L_2 L_1}{EI} \tag{9.9}$$

where I is the moment of inertia for the cross-section. The deflection of the tower top subjected to wind load is then obtained as

$$u_A = u_1 + u_2 + u_3 + (\theta_2 + \theta_3)L_2 \tag{9.10}$$

To calculate the effect of the ship impact, the principles of conservation of momentum and conservation of energy is used. The impact behaviour of the OWT can be expressed by the elastic stiffness relations which gives the internal collision force, F_c, in Equation 9.11 and the internal transmitted force, F_t, in Equation 9.12.

$$F_c = k_{11} u_c + k_{12} u_t \tag{9.11}$$

$$F_t = k_{21} u_c + k_{22} u_t = -m_t \ddot{u}_t + c_t \dot{u}_t \tag{9.12}$$

Here, c_t is the linear damping term, including structural damping (Rayleigh damping), radiation damping in the support structure, soil damping, and aerodynamic damping (Song et al., 2021).

The interaction between the OWT and ship is approximated by the relation seen in Equation 9.13.

$$F_c = \begin{cases} n k_s (u_s - u_c) & \text{for} \quad \dot{u}_s - \dot{u}_c \geq 0 \\ n0 & \text{for} \quad \dot{u}_s - \dot{u}_c < 0 \end{cases} \tag{9.13}$$

For the first phase of the impact, which is the crushing phase, the displacement of the topside, u_t, is assumed to be small, which consequently mean the damping is neglected. In addition, the maximum collision force is reached when ship velocity, $\dot{u}_s$, equals the contact point velocity, $\dot{u}_c$. This gives the velocity of the ship as given in Equation 9.14 based on

Equation 9.11. Thus. the generalized force, F_c, is approximated by Equation 9.15.

$$\dot{u}_s = -\frac{k_{12}}{k_{11}}\dot{u}_t \tag{9.14}$$

$$F_t = -\frac{k_{21}}{k_{11}}F_c \tag{9.15}$$

The conservation of momentum is given by Equation 9.16 and Equation 9.17.

$$I_c = m_a(V_0 - \dot{u}_s) = \int_0^{t_1} F_c(t)dt \tag{9.16}$$

$$I_t = -m_t\dot{u}_t = \int_0^{t_1} (F_t(t) - c_t\dot{u}_t)dt \approx \int_0^{t_1} F_t(t)dt \tag{9.17}$$

The velocity of the centre of gravity for the topside, $\dot{u}_t$, at maximum collision force, F_c, is found from Equations 9.14 - 9.17 and found as Equation 9.18.

$$\dot{u}_t = -\frac{V_0}{\frac{k12}{k11} + \frac{k11}{k21}\frac{m_t}{m_a}} \tag{9.18}$$

Here, V_0 is the impact velocity. Energy conservation yields Equation 9.19.

$$\frac{1}{2}m_aV_0^2 = \frac{1}{2}k_c\dot{u}_s^2 + \frac{1}{2}m_t\dot{u}_t^2 \tag{9.19}$$

Here, $k_c = \frac{k_{11}k_s}{k_{11}k_s}$ is the stiffness seen from the ship for zero deflection of the OWT mass.

The maximum collision force at the end of the first phase can then be found by Equation 9.20.

$$F_c = k_cu_s \tag{9.20}$$

The deformation energy that is absorbed as plastic deformation is given by Equation 9.21.

$$E_{ship} = \frac{1}{2}F_c(u_s - u_c) = \frac{F_c^2}{2k_s} \tag{9.21}$$

The deformed energy and damping energy are assumed to be the existing energies at the end of the second phase of the collision. This does not include the absorbed plastic deformation energy. Thus, these energies are given by Equation 9.22.

$$\frac{1}{2}m_a V_0^2 - E_{ship} = \frac{1}{2}(F_t' u_t' + F_c' u_c') + \int_{t_1}^{t_2} c_t \dot{u}_t d_{u_t} \tag{9.22}$$

At the end of the second phase, the collision force, F_c', is considered small. Thus, the energy distribution effect from this force is neglected and $F_c' u_0' \approx 0$. It is further assumed linear damping-displacement relationship during the second phase. Rewrite Equation 9.22 to Equation 9.23.

$$\frac{1}{2}m_a V_0^2 - E_{ship} = \frac{1}{2}F_t' u_t' + \int_{t_1}^{t_2} c_t \dot{u}_t d_{u_t} = \frac{1}{2}k_p (u_t')^2 + \frac{1}{2}c_t \dot{u}_t' u_t' \tag{9.23}$$

The deflection of the tower top subjected to a ship impact is then approximated to Equation 9.24.

$$u_t' = \frac{-c_t \dot{u}_t + \sqrt{(c_t \dot{u}_t)^2 + 4k_p (m_a V_0^2 - 2E_{ship})}}{2k_p} \tag{9.24}$$

Here, $k_p = \frac{k_{11}k_{22} - k_{12}^2}{k_{11}}$ which is the generalized stiffness of the unconstrained centre of gravity (Song et al., 2021).

Finally, the total deflection of the tower top subjected to wind load and impact load can be found from Equation 9.25.

$$u_{total} = u_A + u_t' \tag{9.25}$$

To summarise the procedure, the deflection of the tower top is separated into two scenarios:

1. Only the wind load acting on the simplified OWT and the response is based on beam theory.
2. Only the collision impact acting on the simplified OWT and the response is based on conservation of momentum and conservation of energy.

Two impact phases are used to make assumptions about the forces and displacements. This simplifies the equations. By combining the two scenarios, the total deflection of the tower is found.

Chapter 10

Discussion and conclusion

With the increasing energy demand, offshore wind turbines are an excellent option to capture the full potential of wind energy. However, with the increasing size of the wind farms and OWTs, they are more exposed to ship collisions. In addition, the OWTs are moving towards more hostile environments meaning the vessels increases in size. This will result in more severe collision impact energies that cause more damage to the OWTs and may result in catastrophic outcomes. Therefore, it is of interest to investigate such scenarios.

A 10MW OWT with monopile foundation located at a water depth of 30m is exposed to a drifting broadside impact from a 7,500 tons displacement supply vessel. The vessel collides with the monopile of the OWT, which has a diameter of 9m and a wall thickness of 80mm. The impact velocities are 2m/s and 3m/s, resulting in impact energies of 21MJ and 47MJ, respectively.

Local analysis has been conducted in the software program LS-DYNA, while the global response of the OWT has been investigated in the software program USFOS. Additionally, USFOS is used to investigate the local effects such as buckling.

10.1 Discussion

In LS-DYNA, the ship is represented by a small section of the whole ship. The boundary conditions applied to the ship do not allow the ship section to bend. This means that the ship section may not be represented in the most optimal way to replicate a realistic behaviour.

Both software programs simulated a dynamic response of the OWT. The top part of the OWT can be seen to move at a later stage than parts close to the impact. This is due to the large mass of the RNA that will give a large moment of inertia of the structure and hence, delay the displacement of the top of the OWT.

The global analysis results indicate that the OWT structure will endure the ship impact for both impact velocities of 2m/s and 3m/s. There are two results of concern: the high plastic utilisation on the ship impact side for an impact velocity of 2m/s and the high accelerations of the OWT top, both for parked condition. This indicates the structure may collapse on top of the colliding ship and that the electrical equipment in the nacelle may be damaged.

Based on the local analysis conducted in USFOS of the critical area showing the highest plastic utilisation, the wall thickness of the tower was reduced by 10%, and the imperfections were increased to investigate possible buckling and, thus, the potential collapse of the tower. By reducing the wall thickness, the stresses are underestimated, and by increasing the imperfections, the buckling will be triggered. However, no buckling was observed, and no collapse is expected to occur. It can be discussed if the fringe pattern indicates buckling behaviour, but as it is well below one and no visible deformation was observed, it is concluded that no buckling occurs.

As previously mentioned, no significant difference was observed for the blade tip clearance for the first impact. This is due to the location of the blade when the impact occurred. When the impact was timed such that one blade would be directly in front of the tower, a decrease in blade tip clearance could be seen of approximately 1.3m. In this thesis, the clearance between blade and tower always produced a good margin, and there was never a risk of the blades hitting the tower. It proves that the blades are well damped and hence, reduces the deformation they obtain during the impact. However, it is important to highlight that the effect of blade tip clearance could only be observed when the blade was directly in front of the tower. This means in order to observe the blade tip clearance and if the blade would it the tower, one blade has to be directly in front of the tower. Thus, the worst-case scenario is when the blade is directly in front of the tower during impact.

Further, it should be noted that the spring stiffness for the two software programs provides two very different values, as shown in Table 10.1. The spring stiffness in LS-DYNA is based on the formula $4EI/L$, while in USFOS, the spring stiffness is a direct input. Both springs have been tuned to give the desired eigenperiods obtained by an eigenvalue analysis. Unfortunately, no apparent reason was found to explain this difference.

Table 10.1: Spring stiffness comparison between USFOS and LS-DYNA.

Software	Spring stiffness [Nm/rad]	Difference[%]
USFOS	1.8E+11	177
LS-DYNA	1.1E+10	

Lastly, a brief discussion on the design principles are made. A comparison can be seen in Appendix H and I. The force-deformation relationship for denting of tubular members shows a large discrepancy. However, this is expected as $w_d/D < 0.05$, i.e. for small indentation. Secondly, the reduction of moment capacity due to local denting is evaluated. Again, due to small indentation, the comparison would be highly conservative as it is assumed that the flat part of the dented section is assumed non-effective, which is not the case. Finally, the force-deformation curves obtained from LS-DYNA and the recommended DNV GL (2020a) force-deformation curves shows that the force-deformation curve obtained from LS-DYNA produces lower force for the same deformation. This is due to neither of the structures being assumed infinitely rigid, which is the case in DNV GL (2020a).

10.2 Conclusion

The main aim of this thesis was to investigate the global response of a monopile supported offshore wind turbine subjected to ship impact by considering local deformations.

A local analysis of a broadside ship impact with the monopile of an OWT was conducted. The force-deformation curve for the system was obtained and interpolated to obtain input points for the global analysis. These points represent the deformation and strength of the ship and OWT and are represented by a nonlinear spring in the global analysis. The complete ship impact consisted of a nonlinear and a linear spring. The global analysis investigated the OWT in both parked and operating conditions, in addition to local effects such as buckling.

The OWT displayed high resistance to the collision scenarios, and the monopile was little affected. The most critical responses were found in the midsection of the tower and the acceleration of the nacelle. The most significant bending stresses for the midsection was found to be 285MPa for the operating condition when subjected to the largest impact velocity. The most significant accelerations of the nacelle were found to be for the parked condition with the largest impact velocity. In contrast, the most significant moment force was found for the operating condition for the largest impact velocity.

The investigation further showed that a potential collapse mechanism could occur for the parked condition for the lowest impact velocity as the most significant moment force was found when the OWT was moving towards the ship. Local analysis was conducted in USFOS using shell elements and imperfections to investigate the situation. Additionally, the wall thickness of the tower was reduced to underestimate the stresses and maximum imperfection was increased to trigger buckling. However, further investigation revealed that no buckling appeared and that the structure would endure the impact. High plastic utilisation was observed during the impact, where the most significant was for the largest impact velocity. The controller algorithm provided beneficial effects in operating condition by reducing the responses of the OWT.

All scenarios were desirable as the OWT would withstand the impact from the broadside of the vessel.

Chapter 11

Further work

The following are suggested for further work on this subject:

- Due to time constraints, sliding impact was not conducted. Hence, it is encouraged to investigate sliding impacts on OWTs as sliding impacts may be a more common scenario during ship impacts.
- Soil characteristics and soil effects were not included and investigated. Since the soil characteristics affect the response of the OWT, it should be implemented in further analysis.
- This thesis used a supply vessel of 7,500 tons displacement, but it would be interesting to evaluate the response of other vessels, e.g. ro-ro vessels or tankers.
- The transition piece (TP) was not modelled in this thesis. The TP is essential as it transfers loads and moment between the tower and the foundation. Additionally, the TP is part of the OWT and is likely where the impact will occur. Thus, it would enhance the realistic modelling by implementing one.
- OWTs are increasing in size, and it would be interesting to model larger OWT and investigate their responses to ship impacts, e.g. 12-14MW capacity turbines. This depends on available data.
- Further investigation of the simple analytic model of an OWT exposed to a ship impact should be performed. Due to time constraints, the presented analytical model was not validated, and thus, a verification of the simplified analytical model should be conducted.

- The effects of waves and currents was not included in this thesis, and as such, it would be interesting to investigate this. Waves may alter the impact point and cause wave loading on the damaged OWT, which may affect the response of the OWT.
- The wind direction has only been investigated in the same direction as the impact. Previous literature indicates that a wind direction on the opposite side of the impact may results in more significant effects on the structural behaviour. Thus, wind direction in the opposite direction of the ship impact should be investigated.
- Other bottom-fixed substructures would be of interest to investigate for comparison. This will help determine the most optimal choice for different load conditions.
- The dimensions of the monopile used in this thesis' could be challenged more to investigate potential collapse mechanisms of the support structure.

Bibliography

Amdahl, J. (2008). Buckling of Cylindrical Shells. *TMR4205 Buckling and Ultimate Strength of Marine Structures*. Department of Marine Technology, NTNU.

Bachynski, E. E. & Ormberg, H. (2015). Hydrodynamic modeling of large-diameter bottom-fixed offshore wind turbines. *ASME 2015 34th International Conference on Ocean, Offshore and Arctic Engineering, May 31 - June 5, 2015*. The American Society of Mechanical Engineers (ASME).

Bai, Y. & Jin, W.-L. (Eds.). (2016). Chapter 21 - Offshore Structures Under Impact Loads. In *Marine Structural Design* (2. edition, 427–446). Butterworth-Heinemann. https://doi.org/https://doi.org/10.1016/B978-0-08-099997-5.00021-6

Bak, C., Zahle, F., Bitsche, R., Kim, T., Yde, A., Henriksen, L. C., Natarajan, A. & Hansen, M. H. (2013). *The DTU 10MW Reference Wind Turbine* (DTU Wind Energy Report-I-0092). DTU Wind Energy.

Bela, A., Sourne, H. L., Buldgen, L. & Rigo, P. (2017). Ship collision analysis on offshore wind turbine monopile foundations. *Marine Structures*, *51*, pp. 220–241. https://doi.org/https://doi.org/10.1016/j.marstruc.2016.10.009

Broersen, A. (2020). *Analytical model to assess bending moments in wind turbine support structures subjected to ship collisions* (Master's thesis). Delft University of Technology.

Caithness Windfarm Information Forum. (2020, July 4). *Wind turbine accident and incident compilation*. http://www.caithnesswindfarms.co.uk/fullaccidents.pdf

Dai, L., Ehlers, S., Rausand, M. & Utne, I. B. (2013). Risk of collision between service vessels and offshore wind turbines. *Reliability Engineering and System Safety*, *109*, pp. 18–31. https://doi.org/10.1016/j.ress.2012.07.008

DNV GL. (2018). *Standard, DNVGL-ST-0126, Support structures for wind turbines.* https://rules.dnvgl.com/docs/pdf/DNVGL/ST/2018-07/DNVGL-ST-0126.pdf

DNV GL. (2019). *Recommended practice, DNVGL-RP-C202, Buckling strength of shells.* https://oilgas.standards.dnvgl.com/docs/pdf/2019-09/DNVGL-RP-C202.pdf

DNV GL. (2020a). *Recommended practise, DNVGL-RP-C204, Structural design against accidental loads*. https://oilgas.standards.dnvgl.com/docs/pdf/2020-06/DNVGL-RP-C204.pdf

DNV GL. (2020b). *Standard, DNVGL-OS-C401, Fabrication and testing of offshore structures*. https://rules.dnvgl.com/docs/pdf/DNVGL/OS/2020-07/DNVGL-OS-C401.pdf

Esteban, M. D., Diez, J. J., Lopez, J. S. & Negro, V. (2010). Why offshore wind energy? *Renewable Energy*, *36*(2), pp. 444–450. https://doi.org/10.1016/j.renene.2010.07.009

Financial Insurance GmbH. (2012). *Offshore Wind Farm Baltic Eagle - Preliminary Design - Collision Analysis Report for WTG-Foundation Structures* (90267-WTG-FOU-KOL-01). https://www.naturvardsverket.se/upload/stod-i-miljoarbetet/remisser-och-yttranden/tidigare/remisser-2013/esbo/baltic-eagle/baltic-eagle-kollisionsanalys-130327.pdf

Hansen, M. H. & Henriksen, L. C. (2013). *Basic DTU Wind Energy controller* (DTU Wind Energy E No.0028). DTU Wind Energy.

Horn, J.-T. (2018). *Statistical and Modelling Uncertainties in the Design of Offshore Wind Turbines* (Doctoral dissertation). Norwegian University of Science and Technology.

International Organization for Standardization. (2019). *ISO 19900 - Petroleum and natural gas industries - General requirements for offshore structures*. https://www.standard.no/

Kühn, M. (2001). *Dynamics and Design Optimisation of Offshore Wind Energy Conversion Systems* (Doctoral dissertation). Delft University of Technology.

Liu, C., Hao, E. & Zhang, S. (2015). Optimization and application of a crashworthy device for the monopile offshore wind turbine against ship impact. *Applied Ocean Research*, *51*, pp. 129–137. https://doi.org/http://dx.doi.org/10.1016/j.apor.2015.03.004

Livemore Software Technology. (2017). *LS-DYNA Keyword user's manual, Volume 2 Material Models*. https://www.dynasupport.com/manuals/ls-dyna-manuals/ls-dyna-manual-r10.0-vol-ii

Llivemore Software Technology. (2006). *LS-DYNA Theory manual*. https://www.dynasupport.com/manuals/additional/ls-dyna-theory-manual-2005-beta

Marine Traffic. (2021, June 9). *Live map*. https://www.marinetraffic.com/en/ais/home/centerx:-3.1/centery:55.4/zoom:5

Moan, T. (2003). *TMR4190: Finite Element Modelling and Analysis of Marine Structures*. Department of Marine Technology, NTNU.

Moulas, D., Shafiee, M. & Mehmanparast, A. (2017). Damage analysis of ship collisions with offshore wind turbine foundations. *Ocean Engineering*, *143*, pp. 149–162. https://doi.org/https://doi.org/10.1016/j.oceaneng.2017.04.050

Nejada, A. R., Bachynski, E. E., Lia, L. & Moan, T. (2016). Correlation between acceleration and drivetrain load effects formonopile offshore wind turbines. *Energy Procedia*, *94*, pp. 487–496. https://doi.org/https://doi.org/10.1016/j.egypro.2016.09.219

Nejada, A. R., Bachynskia, E. E., Lia, L. & Moan, T. (2019). Effect of axial acceleration on drivetrain responses in a spar-type floating wind turbine. *Journal of Offshore Mechanics and Arctic Engineering*, *141*(3), pp. 31901-7–31901-7. https://doi.org/10.1115/1.4041996

Ong, L. & Lu, G. (1996). Tubular beams loaded by a wedge-shape indenter. *Experimental Mechanics*, *36*, pp. 374–378. https://doi.org/https://doi.org/10.1007/BF02328581

Presencia, C. E. & Shafiee, M. (2016). Risk analysis of maintenance ship collisions with offshore wind turbines. *International Journal of Sustainable Energy*, *37*(6), pp. 576–596. https://doi.org/10.1080/14786451.2017.1327437

Ramboll. (2016). *150 monopiles in the North Sea push offshore wind into deeper waters*. https://ramboll.com/projects/re/150-monopiles-in-the-north-sea-push-offshore-wind-into-deeper-waters

Solvik, K. F. (2020). *Ship Collision and Earthquake Analysis of Monopile Offshore Wind Turbines* (Master's thesis). Norwegian University of Science and Technology.

Song, M., Jiang, Z. & Yuan, W. (2021). Numerical and analytical analysis of a monopile-supported offshore wind turbine under ship impacts. *Renewable Energy*, *167*, pp. 457–472. https://doi.org/https://doi.org/10.1016/j.renene.2020.11.102

Sørum, S. H. (2017). *Stochastic, Dynamic Analysis of Offshore Wind Turbines* (Master's thesis). Norwegian University of Science and Technology.

Standards Norway. (2013). *NORSOK Standard N-004: Design of steel structures*. https://www.standard.no/

USFOS Reality Engineering. (n.d.). *USFOS*. https://www.usfos.no/

Verma, A. S. (2019, November 25). *Analysis and design of offshore wind turbines subjected to ship collisions* (PowerPoint-presentation).

WindEurope. (2020a). https://windeurope.org/

WindEurope. (2020b). *Offshore wind in Europe - key trends and statistics 2019*. https://windeurope.org/data-and-analysis/product/offshore-wind-in-europe-key-trends-and-statistics-2019/

WindEurope. (2021a). *Interactive offshore maps*. https://windeurope.org/about-wind/interactive-offshore-maps/

WindEurope. (2021b). *Offshore wind in Europe - key trends and statistics 2020*. https://windeurope.org/data-and-analysis/product/offshore-wind-in-europe-key-trends-and-statistics-2020/

WindPower International. (2013, December 13). *Good foundations: The pros and cons of monopiles*. http://www.windpower-international.com/features/featuregood-foundations-the-pros-and-cons-of-monopiles-4158694/

WindPower Monthly. (2013, September 1). *Foundations types and depth limits - alternative solutions*. https://www.windpowermonthly.com/article/1210054/foundations-types-depth-limits---alternative-solutions

Yu, Z., Liu, Z. & Amdahl, J. (2019). Discussion of assumptions behind the external dynamic models in ship collisions and groundings. *Ships and Offshore Structures*, *14*(sup1), pp. 45–62. https://doi.org/10.1080/17445302.2018.1556234

Yu, Z., Shen, Y., Amdahl, J. & Greco, M. (2016). Implementation of linear potential-flow theory in the 6dof coupled simulation of ship collision and grounding accidents. *Journal of Ship Research*, *60*(3), pp. 119–144. https://doi.org/10.5957/JOSR.60.3.160012

This page is intentionally left blank.

Appendices

Modelling files

A selection of the modelling files used for the local analysis in LS-DYNA and the global analysis in USFOS are distributed to the supervisors as requested by the main supervisor.

For LS-DYNA, the following files are included:

- Broadside ship impact with impact velocity of 2m/s.

For USFOS, the following files are included:

- Broadside ship impact with an impact velocity of 2m/s in parked and operating condition.
- Ship impact file that includes the implemented shell, for both initial tower thickness and a 10% reduced tower thickness.
- Broadside ship impact file with an impact velocity of 3m/s.

A Deformed ship and OWT for an impact velocity of 2m/s

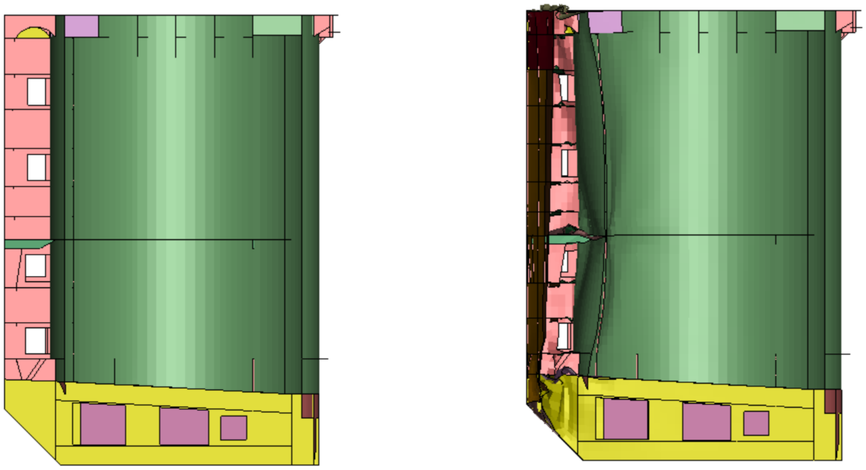

(a) Undeformed ship section **(b)** Deformed ship section

Figure A.1: Vertical cut of deformed and undeformed ship section for an impact velocity of 2m/s.

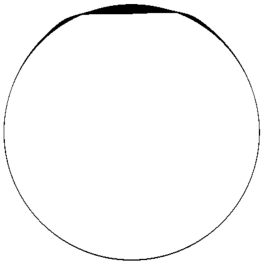

Figure A.2: Deformed OWT, cut to display largest dent at impact point for an impact velocity of 2m/s.

B Deformed ship and OWT for impact velocity of 3m/s

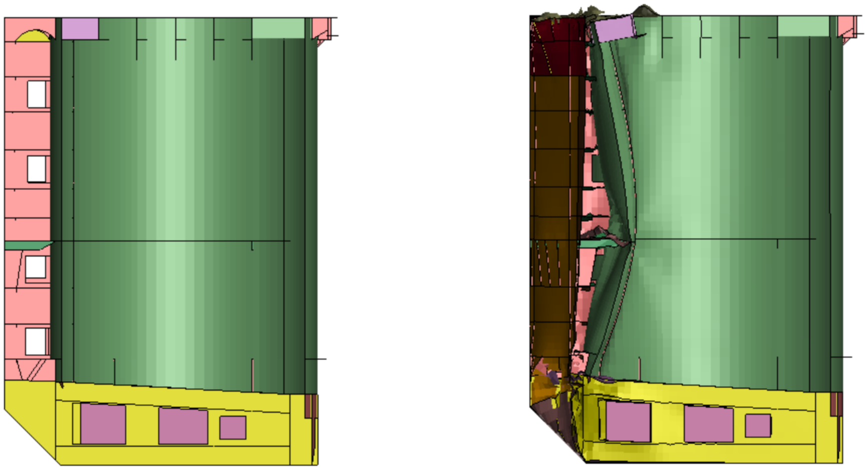

(a) Undeformed ship section **(b)** Deformed ship section

Figure B.1: Vertical cut of deformed and undeformed ship section with an impact velocity of 3m/s.

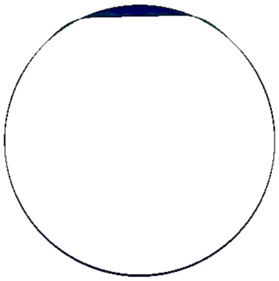

Figure B.2: Deformed OWT, cut to display largest dent at impact point for an impact velocity of 3m/s.

C von Mises stress for an impact velocity of 2m/s

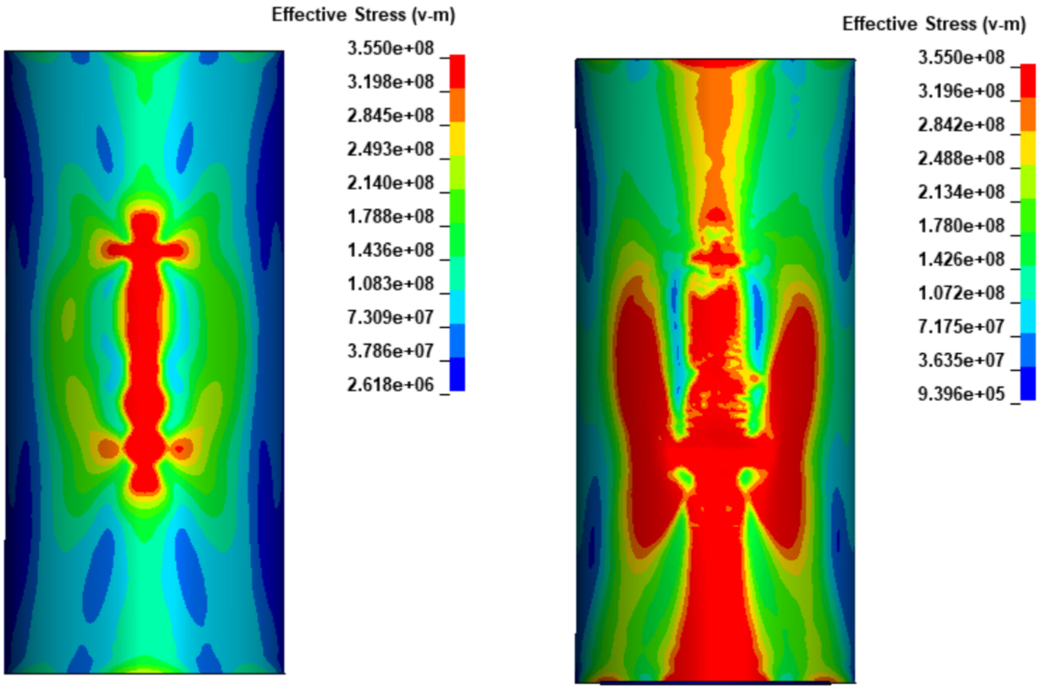

(a) Time = 0.05s.

(b) Time = 0.4s.

Figure C.1: von Mises stress for an impact velocity of 2m/s.

D von Mises stress for an impact velocity of 3m/s

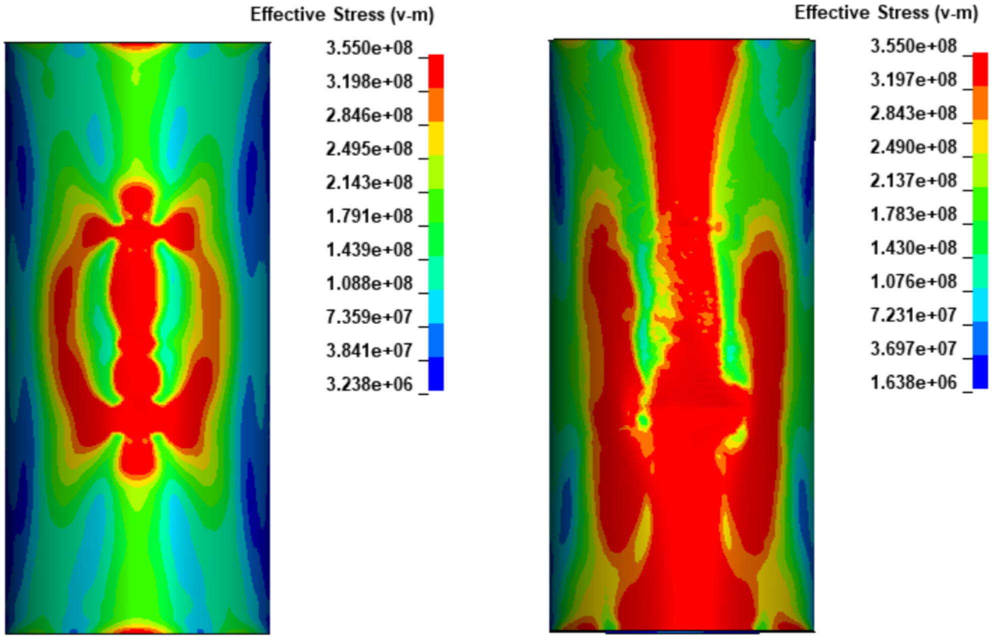

(a) Time = 0.05s. **(b)** Time = 0.4s.

Figure D.1: von Mises stress for an impact velocity of 2m/s.

E Effective plastic strain for an impact velocity of 2m/s

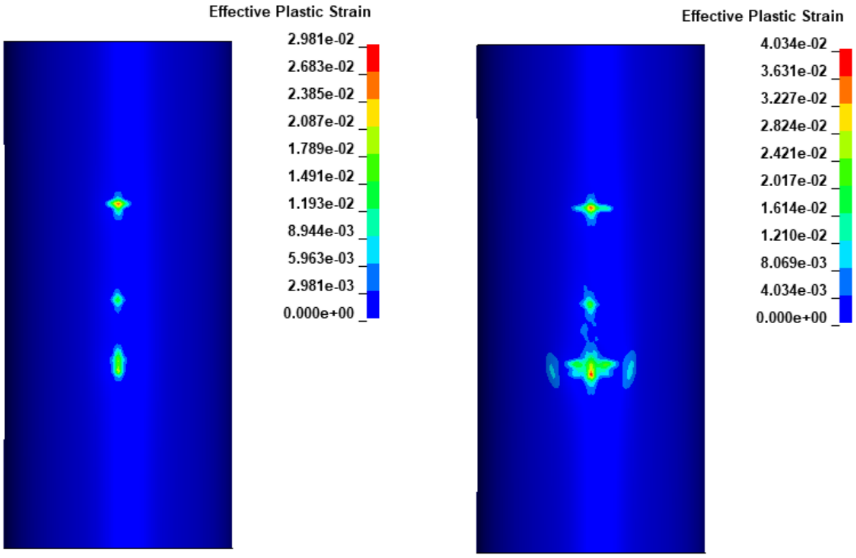

(a) Time = 0.05s.

(b) Time = 0.15s.

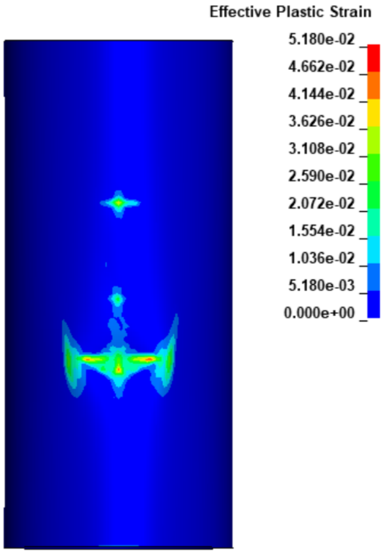

(c) Time = 0.4s.

Figure E.1: Effective plastic strain for an impact velocity of 2m/s.

F Effective plastic strain for an impact velocity of 3m/s

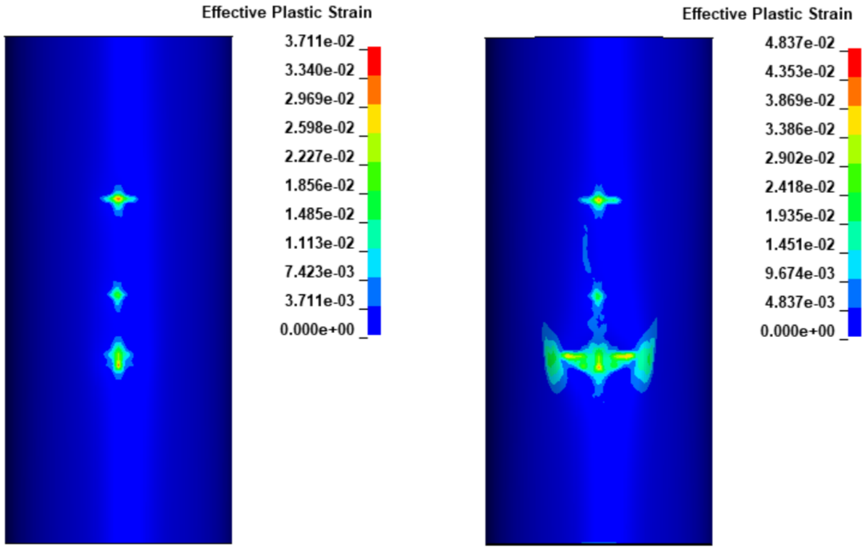

(a) Time = 0.05s.

(b) Time = 0.15s.

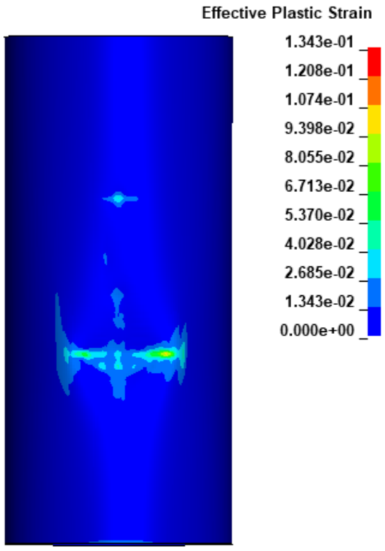

(c) Time = 0.4s.

Figure F.1: Effective plastic strain for an impact velocity of 3m/s.

G Max stresses for evaluation of critical areas

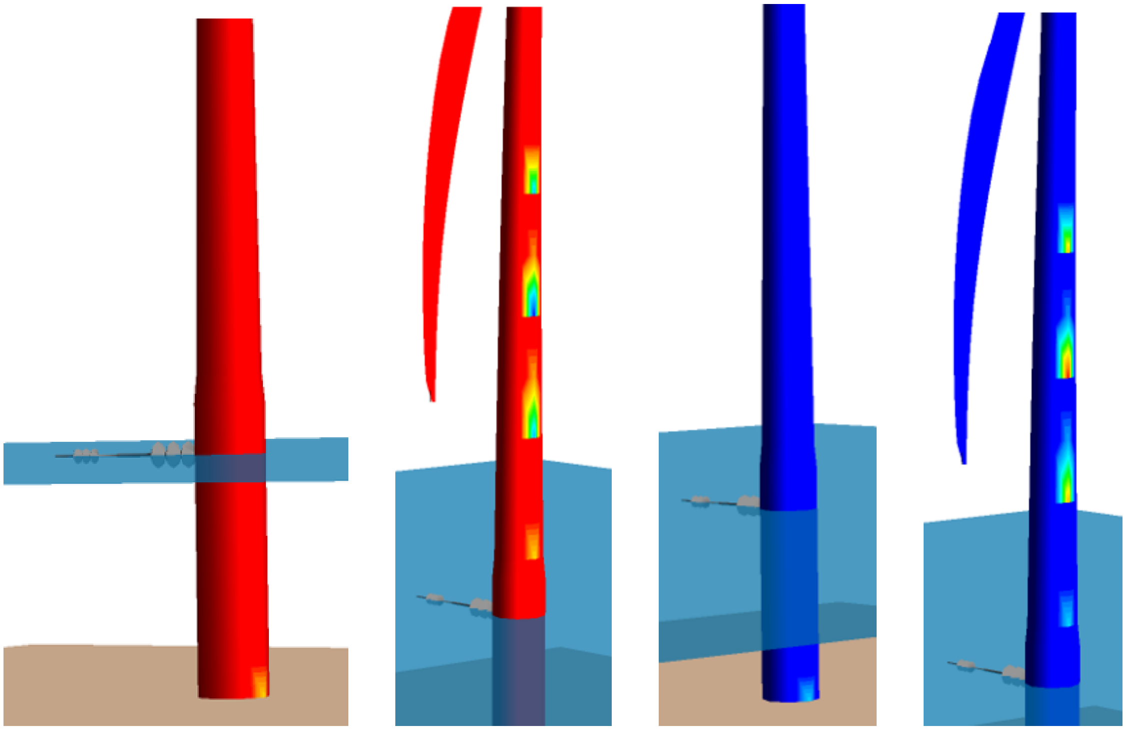

(a) Maximum axial stress at bottom

(b) Maximum axial stress in tower

(c) Maximum von Mises stress at bottom

(d) Maximum von Mises stress in tower

Figure G.1: Max stresses for operating condition for an impact velocity of 2m/s.

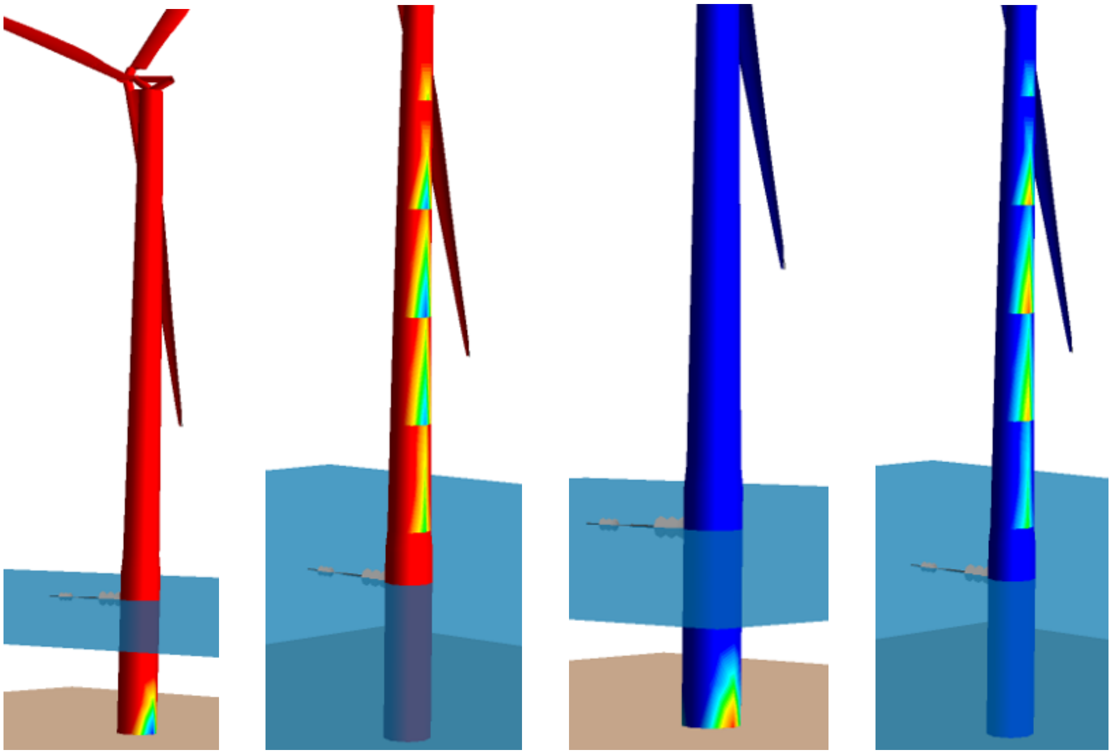

(a) Maximum axial stress at bottom

(b) Maximum axial stress in tower

(c) Maximum von Mises stress at bottom

(d) Maximum von Mises stress in tower

Figure G.2: Max stresses for parked condition for an impact velocity of 2m/s.

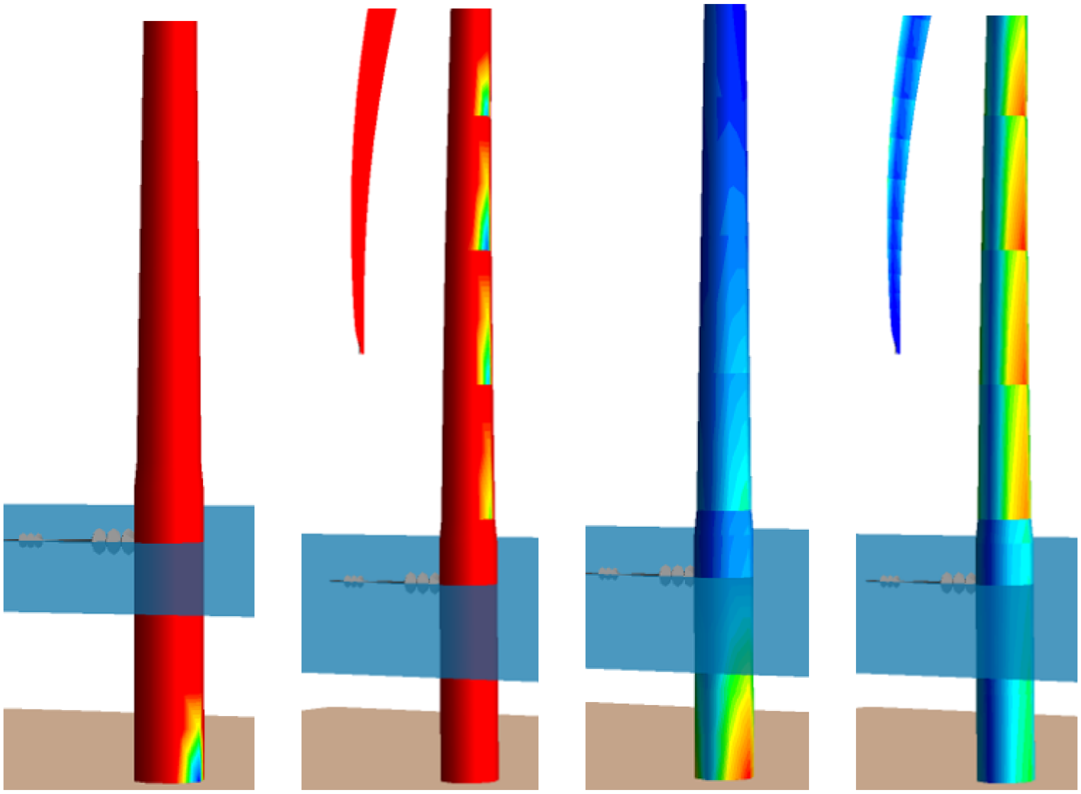

(a) Maximum axial stress at bottom

(b) Maximum axial stress in tower

(c) Maximum von Mises stress at bottom

(d) Maximum von Mises stress in tower

Figure G.3: Max stresses for operating condition for an impact velocity of 3m/s.

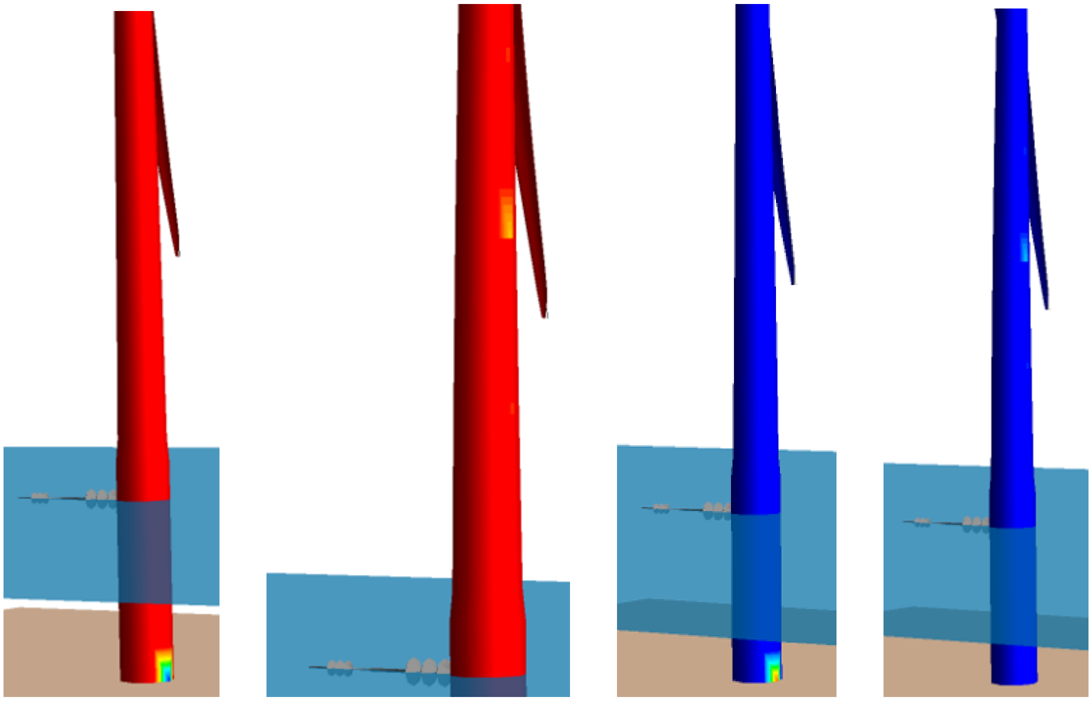

(a) Maximum axial stress at bottom **(b)** Maximum axial stress in tower **(c)** Maximum von Mises stress at bottom **(d)** Maximum von Mises stress in tower

Figure G.4: Max stresses for parked condition for an impact velocity of 3m/s.

Table G.1: Summary of the maximum stresses located at critical areas. Bold text indicates maximum values of the table.

	Middle section		At seabed	
Max. axial stress [MPa]				
Condition	**2m/s**	**3m/s**	**2m/s**	**3m/s**
Operating	254	**285**	210	**285**
Parked	185	212	185	247
Max. von Mises stress [MPa]				
Operating	254	**285**	200	**285**
Parked	187	212	187	252

H Force-deformation relationship for denting of tubular members

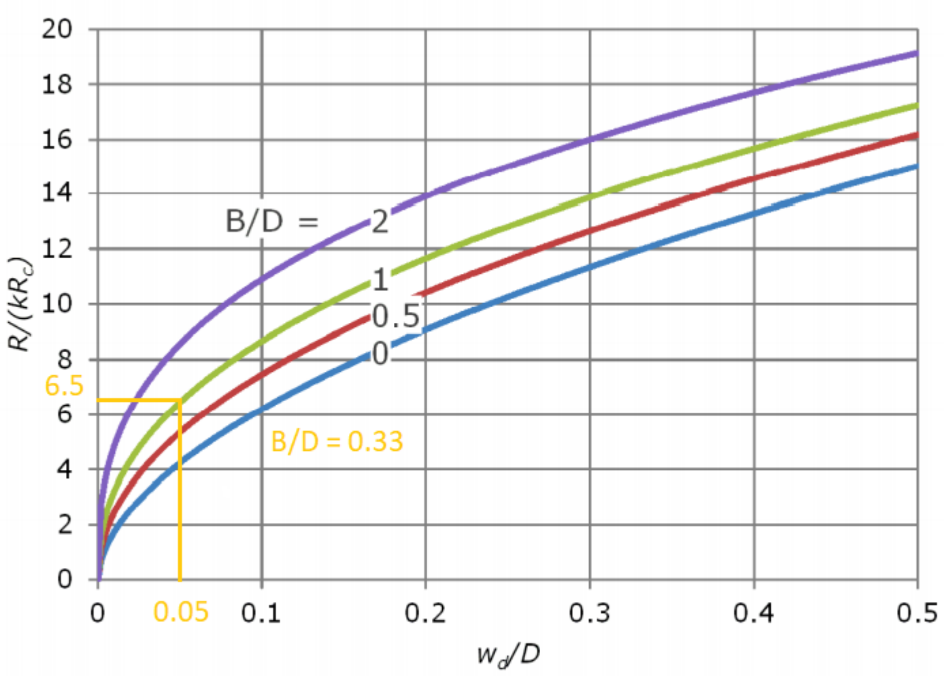

Figure H.1: Force-deformation relationship for denting of tubular members comparison (DNV GL, 2020a).

I Bending capacity of dented tubular members

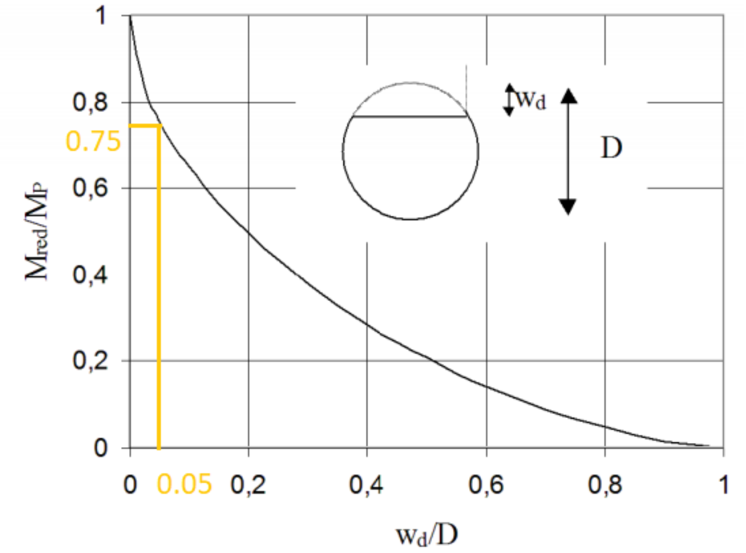

Figure I.1: Bending capacity of dented tubular members (DNV GL, 2020a).

Vilde Eirin Eidsæther Bruun

Ship collision analysis of monopile offshore wind turbines

NTNU
Norwegian University of
Science and Technology